

**INVERSION OF
SYNTHETIC APERTURE RADAR (SAR)
DATA USING BORN APPROXIMATION
AND SAR IMAGE ENHANCEMENT
FOR GEOLOGICAL APPLICATION**

BY

JOONG SUN WON

**A Thesis
Submitted to the Faculty of Graduate Studies
in Partial Fulfillment of the Requirements
for the Degree of**

**DOCTOR OF PHILOSOPHY
IN
GEOPHYSICS**

**Geophysics,
Department of Geological Sciences
University of Manitoba
Winnipeg, Manitoba**

January, 1993



National Library
of Canada

Acquisitions and
Bibliographic Services Branch

395 Wellington Street
Ottawa, Ontario
K1A 0N4

Bibliothèque nationale
du Canada

Direction des acquisitions et
des services bibliographiques

395, rue Wellington
Ottawa (Ontario)
K1A 0N4

Your file *Votre référence*

Our file *Notre référence*

The author has granted an irrevocable non-exclusive licence allowing the National Library of Canada to reproduce, loan, distribute or sell copies of his/her thesis by any means and in any form or format, making this thesis available to interested persons.

The author retains ownership of the copyright in his/her thesis. Neither the thesis nor substantial extracts from it may be printed or otherwise reproduced without his/her permission.

L'auteur a accordé une licence irrévocable et non exclusive permettant à la Bibliothèque nationale du Canada de reproduire, prêter, distribuer ou vendre des copies de sa thèse de quelque manière et sous quelque forme que ce soit pour mettre des exemplaires de cette thèse à la disposition des personnes intéressées.

L'auteur conserve la propriété du droit d'auteur qui protège sa thèse. Ni la thèse ni des extraits substantiels de celle-ci ne doivent être imprimés ou autrement reproduits sans son autorisation.

ISBN 0-315-81680-5

Canada

Name WON, JOONG SUN

Dissertation Abstracts International is arranged by broad, general subject categories. Please select the one subject which most nearly describes the content of your dissertation. Enter the corresponding four-digit code in the spaces provided.

Geophysics

0	3	7	3
---	---	---	---

U·M·I

SUBJECT TERM

SUBJECT CODE

Subject Categories

THE HUMANITIES AND SOCIAL SCIENCES

COMMUNICATIONS AND THE ARTS

Architecture 0729
 Art History 0377
 Cinema 0900
 Dance 0378
 Fine Arts 0357
 Information Science 0723
 Journalism 0391
 Library Science 0399
 Mass Communications 0708
 Music 0413
 Speech Communication 0459
 Theater 0465

EDUCATION

General 0515
 Administration 0514
 Adult and Continuing 0516
 Agricultural 0517
 Art 0273
 Bilingual and Multicultural 0282
 Business 0688
 Community College 0275
 Curriculum and Instruction 0727
 Early Childhood 0518
 Elementary 0524
 Finance 0277
 Guidance and Counseling 0519
 Health 0680
 Higher 0745
 History of 0520
 Home Economics 0278
 Industrial 0521
 Language and Literature 0279
 Mathematics 0280
 Music 0522
 Philosophy of 0998
 Physical 0523

Psychology 0525
 Reading 0535
 Religious 0527
 Sciences 0714
 Secondary 0533
 Social Sciences 0534
 Sociology of 0340
 Special 0529
 Teacher Training 0530
 Technology 0710
 Tests and Measurements 0288
 Vocational 0747

LANGUAGE, LITERATURE AND LINGUISTICS

Language
 General 0679
 Ancient 0289
 Linguistics 0290
 Modern 0291
 Literature
 General 0401
 Classical 0294
 Comparative 0295
 Medieval 0297
 Modern 0298
 African 0316
 American 0591
 Asian 0305
 Canadian (English) 0352
 Canadian (French) 0355
 English 0593
 Germanic 0311
 Latin American 0312
 Middle Eastern 0315
 Romance 0313
 Slavic and East European 0314

PHILOSOPHY, RELIGION AND THEOLOGY

Philosophy 0422
 Religion
 General 0318
 Biblical Studies 0321
 Clergy 0319
 History of 0320
 Philosophy of 0322
 Theology 0469

SOCIAL SCIENCES

American Studies 0323
 Anthropology
 Archaeology 0324
 Cultural 0326
 Physical 0327
 Business Administration
 General 0310
 Accounting 0272
 Banking 0770
 Management 0454
 Marketing 0338
 Canadian Studies 0385
 Economics
 General 0501
 Agricultural 0503
 Commerce-Business 0505
 Finance 0508
 History 0509
 Labor 0510
 Theory 0511
 Folklore 0358
 Geography 0366
 Gerontology 0351
 History
 General 0578

Ancient 0579
 Medieval 0581
 Modern 0582
 Black 0328
 African 0331
 Asia, Australia and Oceania 0332
 Canadian 0334
 European 0335
 Latin American 0336
 Middle Eastern 0333
 United States 0337
 History of Science 0585
 Law 0398
 Political Science
 General 0615
 International Law and Relations 0616
 Public Administration 0617
 Recreation 0814
 Social Work 0452
 Sociology
 General 0626
 Criminology and Penology 0627
 Demography 0938
 Ethnic and Racial Studies 0631
 Individual and Family Studies 0628
 Industrial and Labor Relations 0629
 Public and Social Welfare 0630
 Social Structure and Development 0700
 Theory and Methods 0344
 Transportation 0709
 Urban and Regional Planning 0999
 Women's Studies 0453

THE SCIENCES AND ENGINEERING

BIOLOGICAL SCIENCES

Agriculture
 General 0473
 Agronomy 0285
 Animal Culture and Nutrition 0475
 Animal Pathology 0476
 Food Science and Technology 0359
 Forestry and Wildlife 0478
 Plant Culture 0479
 Plant Pathology 0480
 Plant Physiology 0817
 Range Management 0777
 Wood Technology 0746
 Biology
 General 0306
 Anatomy 0287
 Biostatistics 0308
 Botany 0309
 Cell 0379
 Ecology 0329
 Entomology 0353
 Genetics 0369
 Limnology 0793
 Microbiology 0410
 Molecular 0307
 Neuroscience 0317
 Oceanography 0416
 Physiology 0433
 Radiation 0821
 Veterinary Science 0778
 Zoology 0472
 Biophysics
 General 0786
 Medical 0760

Geodesy 0370
 Geology 0372
 Geophysics 0373
 Hydrology 0388
 Mineralogy 0411
 Paleobotany 0345
 Paleoecology 0426
 Paleontology 0418
 Paleozoology 0985
 Palynology 0427
 Physical Geography 0368
 Physical Oceanography 0415

HEALTH AND ENVIRONMENTAL SCIENCES

Environmental Sciences 0768
 Health Sciences
 General 0566
 Audiology 0300
 Chemotherapy 0992
 Dentistry 0567
 Education 0350
 Hospital Management 0769
 Human Development 0758
 Immunology 0982
 Medicine and Surgery 0564
 Mental Health 0347
 Nursing 0569
 Nutrition 0570
 Obstetrics and Gynecology 0380
 Occupational Health and Therapy 0354
 Ophthalmology 0381
 Pathology 0571
 Pharmacology 0419
 Pharmacy 0572
 Physical Therapy 0382
 Public Health 0573
 Radiology 0574
 Recreation 0575

Speech Pathology 0460
 Toxicology 0383
 Home Economics 0386

PHYSICAL SCIENCES

Pure Sciences
 Chemistry
 General 0485
 Agricultural 0749
 Analytical 0486
 Biochemistry 0487
 Inorganic 0488
 Nuclear 0738
 Organic 0490
 Pharmaceutical 0491
 Physical 0494
 Polymer 0495
 Radiation 0754
 Mathematics 0405
 Physics
 General 0605
 Acoustics 0986
 Astronomy and Astrophysics 0606
 Atmospheric Science 0608
 Atomic 0748
 Electronics and Electricity 0607
 Elementary Particles and High Energy 0798
 Fluid and Plasma 0759
 Molecular 0609
 Nuclear 0610
 Optics 0752
 Radiation 0756
 Solid State 0611
 Statistics 0463
Applied Sciences
 Applied Mechanics 0346
 Computer Science 0984

Engineering
 General 0537
 Aerospace 0538
 Agricultural 0539
 Automotive 0540
 Biomedical 0541
 Chemical 0542
 Civil 0543
 Electronics and Electrical 0544
 Heat and Thermodynamics 0348
 Hydraulic 0545
 Industrial 0546
 Marine 0547
 Materials Science 0794
 Mechanical 0548
 Metallurgy 0743
 Mining 0551
 Nuclear 0552
 Packaging 0549
 Petroleum 0765
 Sanitary and Municipal 0554
 System Science 0790
 Geotechnology 0428
 Operations Research 0796
 Plastics Technology 0795
 Textile Technology 0994

PSYCHOLOGY

General 0621
 Behavioral 0384
 Clinical 0622
 Developmental 0620
 Experimental 0623
 Industrial 0624
 Personality 0625
 Physiological 0989
 Psychobiology 0349
 Psychometrics 0632
 Social 0451



INVERSION OF SYNTHETIC APERTURE RADAR (SAR) DATA USING
BORN APPROXIMATION AND SAR IMAGE ENHANCEMENT FOR
GEOLOGICAL APPLICATION

BY

JOONG SUN WON

A Thesis submitted to the Faculty of Graduate Studies of the University of Manitoba in partial fulfillment of the requirements of the degree of

DOCTOR OF PHILOSOPHY

(c) 1993

Permission has been granted to the LIBRARY OF THE UNIVERSITY OF MANITOBA to lend or sell copies of this Thesis, to the NATIONAL LIBRARY OF CANADA to microfilm this Thesis and to lend or sell copies of the film, and UNIVERSITY MICROFILM to publish an abstract of this Thesis.

The author reserves other publication rights, and neither the Thesis nor extensive extracts from it may be printed or otherwise reproduced without the author's written permission.

I hereby declare that I am the sole author of this thesis.

I authorize the University of Manitoba to lend this thesis to other institutions or individuals for the purpose of scholarly research.

I further authorize the University of Manitoba to reproduce this thesis by photocopying or by other means, in total or in part, at the request of other institutions or individuals for the purpose of scholarly research.

Abstract

An inversion method for synthetic aperture radar (SAR) has been formulated and numerically implemented by applying the Born (first) approximation. The spreading factors for both incident and backscattered fields have been explicitly included in the formulation.

Digital simulations for airborne and spaceborne SAR system configurations have been carried out, and demonstrated that the azimuth compression and the accommodation of the range curvature of the new approach is competitive for both airborne and spaceborne cases. The experimental test with real airborne SAR data acquired in the nadir mode shows slightly underfocused results after direct application of the inversion processing. The initial underfocusing problem, however, can be overcome by further focusing processes. Even though theoretical formulation of the inversion is now completed, certain details of the numerical implementation are needed to be tested further using satellite-borne SAR data.

Enhancements of SAR image data for geological application have also been investigated with specific focus on determination of geological lineaments.

To determine dominant trends of geological lineaments on a SAR image, a

plot of the maximum amplitude of the Radon transform versus slope has been analyzed and found to be very useful. Effects of radar look direction should be taken into account in the Radon transform analysis. A correlation technique using the Radon transform has also been developed. Correlation and certain screening processes, when combined in the Radon transform space, can provide an effective alternative to the traditional correlation approach using the Fourier transform.

The merging of two or more SAR image data sets with different survey parameters has been investigated using the CCRS's airborne C-SAR and the ERS-1 SAR data over the Sudbury Basin, Ontario. Tests have been focused on reduction of radar look direction bias, enhancing the geologic linear features in the merged image. Among the approaches: 1) simple addition and subtraction; 2) directional derivatives followed by simple subtraction; and 3) the principal components analysis (PCA), the PCA approach is most effective for the chosen objective. If only two SAR data sets are available and correlation between these data sets is very low, auxiliary information is required to properly enhance desired geologic lineament features.

Acknowledgements

I would like to express my hearty gratitude to Dr. W.M. Moon for his invaluable assistance and encouragement. His consistent supports have kept me motivated and focused. I wish to give thanks to the members of the examining committee, Dr. P.D. Lowman, Jr., Dr. W.C. Brisbin, Dr. P.D. Loly, Dr. I. Ferguson, and Dr. D. Hall for their careful reading and comments. Special thanks are due to Dr. R.K. Raney for discussion, and Dr. L. Gray for assistance in preparation of data. The SAR data have been provided by CCRS. I also have benefited from my colleagues, Mr. Jisoo Kim and Dr. Ping An. I would like to thank to Prof. K.D. Min, Yonsei University, who led me to geophysics.

Without continuing moral support from my parents, my lovely wife Eun Soon, and pranky son Moosoo, none of the works would have been possible.

Contents

Abstract	iv
Acknowledgements	vi
List of Figures	x
List of Tables	xiii
List of Notations	xv
List of Abbreviations	xvii
1 Introduction	1
1.1 Inversion of SAR Data	2
1.2 SAR Image Enhancement for Geological Application	8
2 Development of Synthetic Aperture (SAR) Systems	11
2.1 Origin and History of Imaging Radar	11
2.2 Spaceborne SAR Systems	16

3	Review of Digital SAR Processors	34
3.1	SAR Geometry and General Principles	34
3.2	Conventional Approach	41
3.2.1	Matched Filter	41
3.2.2	Doppler Phase History	49
3.2.3	Conventional Digital SAR Processors	56
4	Theoretical Development	64
4.1	Background Review	64
4.2	Review of Born Inversion Application	67
4.3	Forward Formulation for SAR Configuration	71
4.4	The Inversion	78
4.5	Further Focusing	83
5	Numerical Algorithm and Image Formation	85
5.1	Algorithm Features	85
5.2	Digital Simulation	90
5.3	Processing of Real SAR Data	102
6	SAR Image Enhancement for Geological Application	114
6.1	Introduction	114
6.2	Determination of Geological Structures Using Radon Transform	118
6.2.1	Introduction	118
6.2.2	Radon Transform Analysis of Lineaments	119
6.2.3	Correlation Using The Radon Transform	137
6.3	Merging of Multiple SAR Image Data Sets	151

6.3.1	Introduction	151
6.3.2	Digital Image Addition and Subtraction	152
6.3.3	Directional Derivative Approach	158
6.3.4	Principal Components Analysis	163
7	Conclusions	171
	Appendices	174
A.	Derivation of Forward Formula	174
B.	Derivation of Inversion Formula	176
C.	Derivation using the Method of Stationary Phase	178
	References	180

List of Figures

1.1	The main elements of a SAR geometry	3
1.2	Slant range and ground range	4
3.1	Radar beam geometry	36
3.2	Geometry for unfocused array	38
3.3	Transmitted waveform of a linear frequency modulated pulse .	43
3.4	Received waveform of the linear frequency modulated pulse and subsequent pulse compression	44
3.5	Amplitude-time characteristics of an ideal matched filter out- put signal	47
3.6	Sensor and scatterer geometry for Doppler parameters	51
3.7	Range walk, range curvature, and range migration	54
3.8	Spaceborne SAR geometry for Doppler parameters	55
3.9	Flow chart of a conventional range-Doppler SAR processor . .	57
3.10	Geometry for a sensor and scatter coordinate	59
3.11	Range migration due to multiple scatterers	60
4.1	Schematic diagram of the SAR geometry and integration vol- ume of Green's integral	74

5.1	Flow chart for the proposed inversion of SAR data	86
5.2	Examples from the frequency domain interpolation	88
5.3	Airborne simulation	93
5.4	Power representation of the reconstructed point scatterer . . .	95
5.5	Seasat simulation with seven point scatterers	97
5.6	Seasat simulation with three point scatterers	100
5.7	Combined perspective view image of amplitudes with phase . .	101
5.8	CCRS's airborne SAR operating geometries	103
5.9	Raw airborne SAR signal	105
5.10	Reconstructed image after initial application of the inversion processing alone	106
5.11	Reconstructed image after a further focusing processing step .	108
5.12	The upper half image	109
5.13	The bottom half image	111
5.14	Power representation of the small subarea	112
6.1	Image coordinate for the Radon transform	121
6.2	Point, lines, and hyperbola in the image space	122
6.3	Radon transform of point, lines, and hyperbola	123
6.4	Location map of the Sudbury Basin and Wekusko Lake test area	125
6.5	CCRS's airborne C-band SAR image over the Sudbury Basin .	126
6.6	ERS-1 SAR image over the Sudbury Basin	127
6.7	Airborne SAR image from the Sudbury Basin superimposed by geological lineaments	129
6.8	Radon transform of airborne SAR data	130

6.9	Radon transform of ERS-1 SAR data	131
6.10	Plot of maximum amplitude of Radon transform versus angle .	134
6.11	Plot of maximum amplitude of Radon transform versus angle .	135
6.12	Model test for correlation through the Radon transform: input data	141
6.13	Model test for correlation through the Radon transform: ref- erence template	142
6.14	Model test for correlation through the Radon transform: output	144
6.15	Airborne C-band SAR data from the Wekusko Lake area . . .	145
6.16	The reference hyperbola for correlation	146
6.17	Correlation output through the Fourier transform approach . .	148
6.18	Correlation output through the Radon transform approach . .	149
6.19	Additive images with factors $a = 1.0$ and $b = 1.0$	154
6.20	Additive images with factors $a = 0.75$ and $b = 0.75$	155
6.21	Subtractive images with factors $a = 0.5$	156
6.22	Subtractive images with factors $a = 0.4$	157
6.23	Directional derivative convolution mask	160
6.24	Image obtained through directional derivative process ($\theta =$ $+43^\circ$)	161
6.25	Image obtained through directional derivative process ($\theta =$ -26°)	162
6.26	The PCA first component image of two data sets	165
6.27	The PCA first component image of three data sets	168
6.28	Maximum amplitude of the Radon transform versus slope . . .	169

List of Tables

2.1	Seasat SAR sensor characteristics	17
2.2	SIR-A and SIR-B sensor characteristics	19
2.3	SIR-C instrument characteristics	21
2.4	ERS-1 payload instruments and their measurement	24
2.5	Geophysical measurements and ERS-1 performance parameters	25
2.6	ERS-1 SAR performance requirements	26
2.7	JERS-1 orbit parameters	28
2.8	Specifications of JERS-1 SAR system	29
2.9	Characteristics of OPS on JERS-1	30
2.10	Radarsat orbit parameters	31
2.11	Specifications of Radarsat SAR	32
2.12	Radarsat imaging modes	33
5.1	Specifications of CCRS's C/X-band airborne SAR	91
5.2	Model parameters for digital simulations	92
6.1	Examples of Radon transform pair	121
6.2	Correlation coefficient of the CCRS's airborne and the ERS-1 SAR data	166

6.3	Eigen values and eigen vectors of two components	166
6.4	Correlation coefficient of three data sets	167
6.5	Eigen values and eigen vectors of three components	167

List of Notations

α	–	squint angle
β	–	half-power beamwidth of an antenna
θ	–	look angle or off-nadir angle
δ	–	incidence angle
λ	–	wavelength
d	–	antenna physical aperture
L	–	distance across the antenna beam on the ground
ω_0	–	angular center frequency of radar signal
ω_d	–	angular frequency shift due to Doppler shift
μ	–	linear FM slope
Δf	–	chirp bandwidth
T	–	pulse duration
τ	–	pulsewidth after matched filtering
T_i	–	interpulse period
PRF	–	Pulse Repetition Frequency ($= 1/T_i$)
TBP	–	Time-Bandwidth Product ($T \Delta f = T/\tau$)
f_{DC}	–	Doppler frequency
f_{DR}	–	Doppler frequency rate
Φ	–	Doppler phase
σ	–	radar cross section
c	–	speed of the light
$s(t)$	–	received radar signal
U_I	–	incident wavefield
U_S	–	scattered wavefield ($\simeq s(t)$)

$\sigma^o(\mathbf{r})$	– complex backscattering coefficient
\mathbf{r}_o	– location vectors of the source
\mathbf{r}	– location vectors of a scatterer
x	– azimuth coordinate
y	– ground-range coordinate
η	– slant-range at the closest approach of an antenna
Δx	– azimuth resolution
k_x	– azimuth wavenumber
k_η	– range wavenumber
χ	– latitude
ψ	– orbit inclination measured from Earth spin vector to orbit rate vector
a	– Earth center angle between spacecraft radius vector and scatterer location vector
ξ	– antenna azimuth angle relative to antenna boresight
ω_s	– spacecraft orbital rotation rate
ω_e	– Earth rotation rate
V_s	– platform velocity ($V_s = \omega_s H$)
V_g	– SAR footprint effective velocity on R_e ($V_g = \omega_s R_e \cos a$)
R_e	– radius of the Earth
R	– radar range
h	– altitude of a platform
\mathbf{R}	– position vector of sensor relative to scatterer
\mathbf{R}_s	– position vector of sensor
\mathbf{R}_t	– position vector of scatterer
\mathbf{V}	– velocity vector of sensor relative to scatterer
\mathbf{V}_s	– velocity vector of sensor
\mathbf{V}_t	– velocity vector of scatterer
\mathbf{A}	– acceleration vector of sensor relative to scatterer
\mathbf{A}_s	– acceleration vector of sensor
\mathbf{A}_t	– acceleration vector of scatterer

(continued from the previous page)

List of Abbreviations

SAR	<i>Synthetic Aperture Radar</i>
RAR	<i>Real Aperture Radar</i>
SLAR	<i>Side-Looking Airborne Radar</i>
CCRS	<i>Canada Center for Remote Sensing</i>
NASA	<i>National Aeronautics and Space Administration</i>
ERIM	<i>Environmental Research Institute of Michigan</i>
IEEE	<i>Institute of Electrical and Electronic Engineering</i>
JPL	<i>Jet Propulsion Laboratory</i>
DFVLR	<i>German Aerospace Research Establishment</i>
NASDA	<i>National Space Development Agency (Japan)</i>
MITI	<i>Ministry of International Trade and Industry (Japan)</i>

Chapter 1

Introduction

The synthetic aperture radar (SAR) technique can record and provide us with invaluable data for study of the Earth and planetary surfaces, and it is becoming one of the most important tools in geological remote sensing today. Using microwave signals, SARs enable us to image terrestrial surfaces with relative independence of weather and solar illumination conditions. Since the late 1970's, a number of spaceborne SAR systems, in addition to numerous airborne systems, have been planned and operated. These include Seasat, Magellan, Almaz, ERS-1, JERS-1, Radarsat, and Space Shuttle missions (Li and Raney [59]). Seasat, SIR-A and SIR-B have already completed their missions and have demonstrated the SAR system's capability of providing us with very important surface information over land and sea. In geological applications, SAR has been extremely effective in imaging surface geological features, such as lineaments and drainage patterns (Trevett [101]). Lithologic discrimination using SAR data, however, is often problematic, although certain lithologic units can be delineated by interpreting topographic expression indirectly (Lowman *et al.* [66]).

The objectives of this thesis may be subdivided into two topics: (1) preliminary development of an inversion approach for SAR signal data by applying the Born (first) approximation; and (2) investigation and development of enhancement techniques of SAR image data for geological applications.

1.1 Inversion of SAR Data

The heart of SAR technology development has been the SAR signal processing techniques which enable a short antenna to be synthesized into a much longer antenna, and consequently to achieve high resolution in along-track or azimuth dimension.

A schematic SAR geometry is shown in Figure 1.1. The *depression angle* is the angle at the radar from the horizontal in range direction to the mid-line of the scan; note this is not necessarily the mid-point across the swath on the ground. The *look angle* (or off-nadir angle) is the complementary angle to the depression angle. The *incidence angle* is the angle which the far beam makes with the vertical at the terrain surface. The *squint angle* is the angle between the along-track direction and the ground range direction. In the side-looking radar case, the squint angle becomes equal to 90° . The *slant range* and *ground range* are illustrated in Figure 1.2. The slant range is determined from the round-trip travel time between antenna and a scatterer on the ground, which is the system's measurements. In the rest of the thesis, the term "range" without specifying "slant" or "ground" represents "slant range".

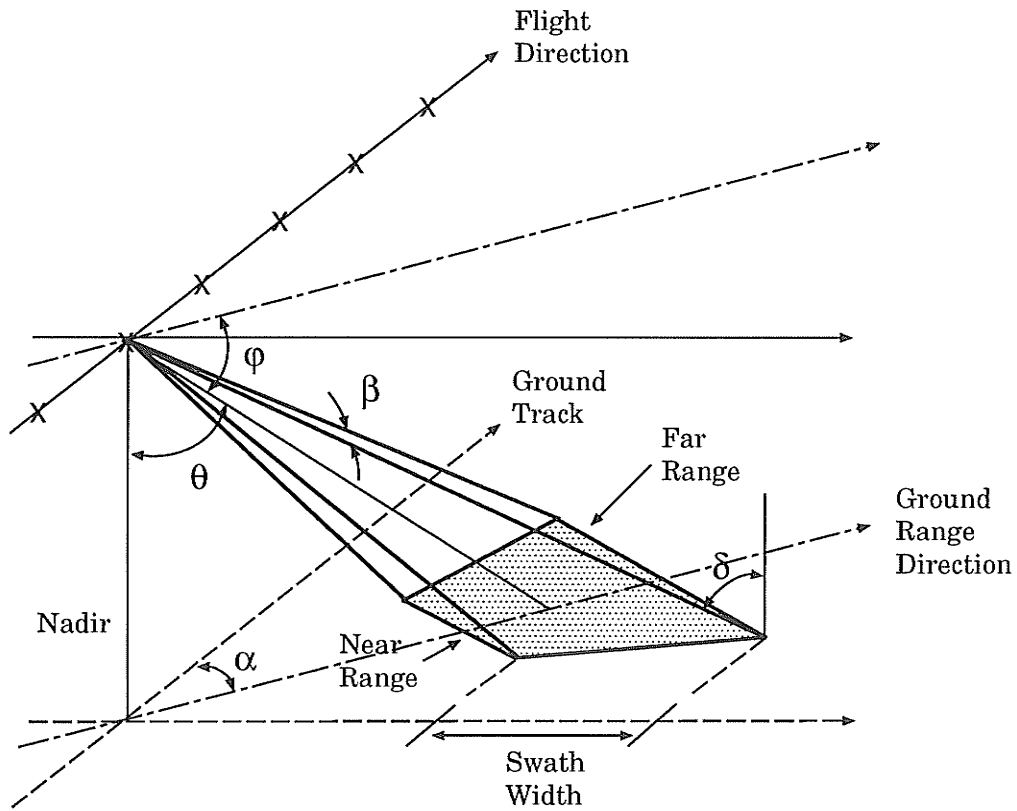


Figure 1.1: The main elements of a SAR geometry: depression angle φ , look angle or off-nadir angle θ , squint angle α , incidence δ angle, and azimuth beamwidth β .

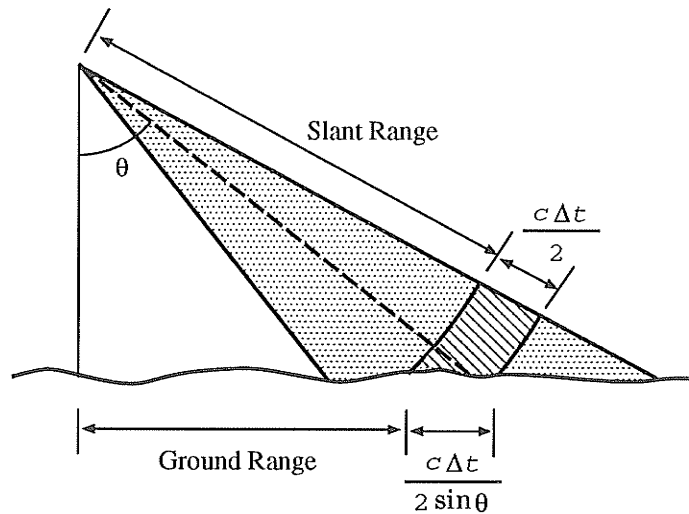


Figure 1.2: Slant range and ground range.

The optical processors had greatly contributed to the SAR signal processing in the early days. In the early 1950's, the University of Illinois group performed experiments to verify the Doppler beam sharpening concept using electronic circuitry. The electronic hardware existing at the time, however, had difficulties in manipulating the large amount of data and operations required for implementing the beam sharpening technique (Ulaby *et al.* [103]). In 1953, a group at the University of Michigan began to examine the possibility of using coherent optics for reconstructing the SAR image from the raw signal (Curtona *et al.* [22]). Until recent years, the coherent optics approach, similar to the technique of holographic image reconstruction, has been the primary SAR processing technique. In addition to the advantage of its relatively fast processing time, photographic film provides a reasonably compact medium for storing the immense amount of raw and processed SAR data.

The optical SAR processors have been replaced by the more efficient and effective digital SAR processors since the late 1970's (Hovnannessian [44]). For the digital SAR processing, an approach utilizing range migration correction and matched filtering in the range-Doppler domain has been widely used by authors such as Wu [109] [110], Bennett and Cumming [6] [7], and Wu *et al.* [112]. Most digital SAR processors currently being used are based on this conventional approach. However, these conventional SAR processors commonly have had difficulties in preserving phase information and improving performance.

For advanced applications of SAR data to geological and geophysical exploration and research, it will become necessary to extract certain characteristic surface parameters from SAR data as well as high quality imagery of terrestrial surface topographic features. Development of a SAR inversion techniques, which can provide an appropriate complex SAR imagery for this specific application has long been required. The $f-k$ domain processing approach is one of the most recent developments in SAR signal processing, and is an alternative to the conventional approach that utilizes the range-Doppler domain processing. The term " $f-k$ domain" represents a two-dimensional Fourier transform domain in both range and azimuth dimensions. Thus the range wavenumber-Doppler domain or the frequency-Doppler domain (if the range data is sampled in time) might be more explicit terminology for the SAR data set. For convenience, the term " $f-k$ domain" will be used in the rest of the thesis. The $f-k$ domain processing approach is still in the early stage of development, and thus various tests and verifications are required in

order to evaluate its full advantage over the conventional SAR processor.

In recent years several new SAR processing approaches have been reported, in which the f - k domain processing is utilized not only to accomplish the azimuth compression but also simultaneously the range curvature corrections. To achieve more effective SAR processor performance than is available from the conventional range-Doppler algorithm, Rocca *et al.* [96], and Raney and Vachon [89] have developed wavenumber domain or f - k domain SAR signal processing techniques. (Raney and Vachon's approach was developed from analysis of the SAR system theory, while the Rocca *et al.* approach was developed based on similarities between the reflection seismic and SAR data acquisition configurations.)

Inversion of SAR data represents the transformation of SAR signal data into an image. In this thesis, a particular SAR inversion approach in the f - k domain is formulated using the Born (first) approximation. The development of a new SAR processing approach is aimed at formulating an SAR inversion capable of providing appropriate SAR processed output from which the complex backscattering coefficient of the surface can be eventually estimated. To extract the complex backscattering coefficient of the surface, it is necessary that the complex ratio of the backscattered field to the incident field at the scattering surface should be estimated from SAR data. The development concentrates on the initial formulation, and a numerical implementation; the development of a full-fledged SAR processor goes beyond the purpose of the work.

The f - k domain SAR inversion technique described in this thesis was in-

spired initially by Rocca *et al.*'s success in applying seismic migration theory to the SAR signal processing. Seismic migration theory is based on the "exploding reflection model" (Loewenthal *et al.* [64]), a construct that was derived originally using heuristic arguments. This thesis utilizes the Born inversion approach (Born [12]) to formulate the final SAR inversion formula rigorously. The Rocca *et al.* approach included the spreading factor of only the backscattered field. As learned in the course of this research, the spreading factor of the incident field also can be included by introducing frequency derivatives in the derivation.

Digital simulations of airborne and spaceborne SAR system configurations are carried out to test the performance of the new inversion algorithm. For digital simulations, a single point scatterer model and also multiple point scatterer models are used. The simulation results demonstrate that the inversion technique is very effective for both airborne and spaceborne cases. A set of SAR test data, provided by Canadian Center for Remote Sensing (CCRS), is C-band airborne SAR data acquired in a nadir half-swath mode, HH-polarization. The test results turned out to be slightly underfocused after direct application of the inversion processing. The initial underfocusing problem, however, has been successfully overcome by further focusing processes.

Although the theoretical derivation of the f - k domain inversion is completed, certain details of the numerical implementation of the approach are yet to be assessed quantitatively. More detailed theoretical review, and quantitative tests using satellite-borne SAR data, are needed to verify that the

algorithm extracts the complex backscattering coefficient properly.

1.2 SAR Image Enhancement for Geological Application

In this thesis, SAR image enhancement for geological application is focused on enhancing geological lineaments. Geological lineament study using remote sensing data has long been one of the most important applications in the geological remote sensing. SAR images generally provide more clear lineament details than other optical sensor data such as Landsat MSS and TM images (Harris [40]). A comprehensive discussion of lineament mapping using Seasat SAR imagery was made by Harris [40], in which lineaments were interpreted by visual investigation. For automatic detection of lineaments on a remote sensing digital image, a technique using the Hough transform was recently investigated by Wang and Howarth [105].

In this thesis, the Radon transform technique is investigated for determining dominant trends of lineaments on SAR image data rather than individual lineament mapping.

When a SAR image is interpreted for geological applications, the radar look direction bias must be taken into account (Harris [40], Lowman *et al.* [66], and Masuoka *et al.* [75]). The radar look direction determines the preferential enhancement of terrain surface features: linear features within 20° of being parallel to the look direction are practically invisible (Lowman *et al.* [66]), whereas those within 20° of normal to the look direction are strongly highlighted (Harris [40]). For this reason, Lowman *et al.* [66] sug-

gested that at least two look directions be mandatory in any SAR application project for geologic investigation. It therefore becomes important to investigate techniques that can combine multiple SAR data sets for optimum geologic interpretation.

Image enhancement study for geological application of SAR data in this thesis is focused on two sub-objectives:

- 1) development of a Radon transform technique for determining dominant trends in geological lineaments; and
- 2) investigation of merging of two or more SAR image data into one digital image to reduce the radar look bias and consequently to enhance geological features in the resulting image.

This thesis stresses SAR data application development in a geologic context rather than geologic interpretation itself of the test areas.

To determine dominant lineament trends in a SAR image, a plot of the maximum amplitude of the Radon transform versus slope is found to be very useful. An experiment is carried out using a set of the CCRS's airborne C-SAR and the ERS-1 SAR data over the Sudbury Basin. It is demonstrated that dominant trends in surface lineaments can be well analyzed through the Radon transform approach. The effect of a radar look direction bias is also well determined by this plot. Correlation using Radon transform is also investigated to evaluate whether the technique would be useful for discriminating certain geologic structures in a given SAR image. Experiments with airborne C-SAR data from the Wekusko Lake test area were not as

successful as expected. There are, however, some indication that correlation using the Radon transform technique, when combined with certain screening processes in the Radon transformed space, can be an effective alternative to correlation using the Fourier transform approach.

Merging of two or more SAR data sets was experimented with and investigated in three different approaches:

- 1) simple addition or subtraction,
- 2) directional derivative followed by subtraction, and
- 3) the principal components analysis (PCA) approach.

Each test is carried out with the CCRS's airborne C-SAR and the ERS-1 SAR data over the Sudbury Basin test area. It has been learned from these experiments that the PCA technique is the most effective among three approaches. At least three data sets are required to effectively enhance lineaments in the resulting PCA image if correlation between two original data sets is low.

Chapter 2

Development of Synthetic Aperture (SAR) Systems

2.1 Origin and History of Imaging Radar

The radar is a device capable of detecting an object, indicating its distance and position. The acronym “RADAR” was derived from *radio detection and ranging*. An imaging radar system is a radar with which images of the planetary terrain can be achieved rather than simple detection of an object. One of the pioneering paper regarding to radar is traced to G. Marconi [72].

A.H. Taylor and L.C. Young at U.S. Naval Research Laboratory made a discovery while doing radio communications research in 1922, which they at once realized was a potential detection method (Ulaby *et al.* [103]). The initial device was operated by separate transmitter and receiver with continuous-wave transmission. After various experiments and tests on continuous-wave radar in the early 1930’s, the initial radar evolved into a single antenna served as both transmitter and receiver with a pulsed signal. The first successful pulse-radar was operated by U.S. Naval Research Laboratory in 1936 (Ulaby

et al. [103]). Similar development in radar technology was achieved in 1938 by Sir Watson-Watt in England (Ridenour [95]). In the mid-1930s, G. Marconi also succeeded in detecting moving vehicles and aircraft using his radar [73]. During World War II, pulse-radar systems were improved remarkably upon urgent military requests, and airborne radars deployed to detect enemy aircrafts and ships.

It was not until 1950s that a new type of imaging radar, the *side-looking airborne radar* (SLAR), producing continuous strip images was developed. The early SLAR was *real aperture radar* (RAR)*, in which film recording was primary means of display. The advent of SLAR system opened a new era of imaging radar, and it has been subsequently developed into *synthetic aperture radar* or *synthetic array radar* (SAR). Many different real aperture SLAR systems were developed during the 1950's, but images produced by those systems were not available on an unclassified basis till early 1960's. In 1964, a declassified real aperture SLAR system AN/APQ-97 was developed by Westinghouse, initially for U.S. Army Electronics Command (Ulaby *et al.* [103]). This system became commercially available, and it was used extensively for mapping in various parts of the world, primarily with geological studies in mind.

Although the real aperture radar system was widely used as a prominent remote sensing tool through the 1960's, RAR requires both a long antenna

*The term *real aperture radar* (RAR) is used in contrast to *synthetic aperture radar* (SAR), and the term SLAR occasionally represents real aperture side-looking radar as common name of RAR. In the following discussion, the term SLAR will be used to cover common features of RAR and SAR, and terms RAR and SAR used for the individual systems as appropriate (Moore [81])

and large power supply because the along-track resolution is determined by the physical length of the antenna aperture in the RAR system. The size of antenna and power specification are severe constraints if an imaging radar is to be operated on a satellite or other spacecraft. SAR, in which the along-track resolution is determined by signal processing equivalent to a longer synthetic aperture, overcomes these problems.

In 1952, C. Wiley of the Goodyear Aircraft Co. developed an imaging radar with frequency of 75 MHz, initially called *Doppler beam-sharpening system*, whose idea can be traced back to the paper by Sherwin *et al.* [98]. An independent experiment with a Doppler processing radar was conducted by the University of Illinois group in 1953 using an airborne coherent X-band pulsed radar (Brown *et al.* [13]). The research being developed at the University of Illinois was transferred to the University of Michigan about 1956 (Ulaby *et al.* [103]). The classified development of SAR systems took place at the University of Michigan and also at a number of companies during the late 1950's and early 1960's. The first unclassified paper describing a SAR system can be found in Curtona *et al.* [22].

The first operational SAR was the Goodyear AN/APQ-102 system. It was an X-band (3 cm) horizontally polarized system built for military use (Moore [80]). In 1969, the synthetic aperture GEMS (Goodyear Electronic Mapping System) became available commercially (Moore [80]).

The first extensive geological mapping using airborne SAR was conducted in eastern Panama by the United States Army Engineering Topography Lab in 1967 (MacDonald [68]). There had been minimal success in obtaining

aerial photography over the area because of perpetual cloud cover. In this first geologic test of imaging radars various interpretation and application techniques of SAR imagery were developed (MacDonald [68]).

The first spaceborne SAR used for imaging of the Earth's surface was the L-band SAR on Seasat launched by the National Aeronautics and Space Administration (NASA) in 1978 (Jordan [53]). The average orbital altitude of Seasat was 800 *km*, and the horizontally polarized (HH) instrument operated at a fixed wavelength (L-band 23.5 *cm*) and with a fixed look angle (20.5° from nadir) yielding approximately 25 *m* resolution (Jordan [53]). Despite Seasat's relatively short lifetime, SAR images acquired by Seasat clearly demonstrated its contribution to various geoscientific studies as well as ocean wave imaging.

The following spaceborne SAR system after Seasat was the *Shuttle Imaging Radar-A* (SIR-A) carried on-board by the space shuttle Columbia in 1981. The SIR-A technology was derived from Seasat, again using the 23 *cm* wavelength (L-band) and HH-polarization. However, the look angle was changed to a fixed angle of 47°, which was primarily chosen for geological research. SIR-A raw data were optically processed at Jet Propulsion Laboratory (JPL) of Pasadena, California. A dramatic discovery of uncharted paleochannels beneath the Sahara Desert in Sudan and Egypt by SIR-A is an excellent example of SAR utility (McCauley *et al.* [76]).

The next NASA SAR mission was the SIR-B launched in October 1984 on the space shuttle Challenger. SIR-B also used 23 *cm* wavelength (L-band) and HH-polarization, but was equipped with an articulating antenna enabling

the incidence angles to be selectable over the 15° to 60° range. SIR-B data were the first to be digitally encoded and digitally processed.

In the following section, several spaceborne SAR systems will be described. An excellent description of spaceborne radars including Magellan, ERS-1, Almaz II, JERS-1, SIR-C, and RADARSAT may be found in the special section on spaceborne radars in Proceedings of IEEE, June issue 1991 [59]. Good references for geologic uses of orbital SAR are found in IEEE Transactions on Geoscience and Remote Sensing, SIR-B special issue for July, 1986 [48].

2.2 Spaceborne SAR Systems

1) SEASAT

The L-band SAR on Seasat was the first spaceborne scientific imaging radar and was launched into about 800 *km* altitude near-polar orbit in July 1978. Due to an unexpected loss of power, Seasat was unfortunately operated for only little more than 100 days. Despite the relatively short life span of Seasat, the SAR imagery clearly demonstrated SAR sensitivity to surface roughness, slope, and land-water boundaries.

Seasat was designed primarily for oceanographic experiments. Seasat SAR sensor characteristics are summarized in table 2.1. The Landsat imaging system, being an optical system largely dependent upon solar illumination, is of little value in the deep sea area, although it has been successfully used to provide excellent imagery over shallow coastal zones. For this reason, the oceanographic community had stressed a satellite more suited to their particular requirements. Seasat succeeded in measuring the wind and wave conditions over the oceans using a scatterometer (SASS) with an accuracy comparable to that achieved from surface platforms. The Seasat radar altimeter also measured its own height above the sea surface to a remarkable 10 *cm* precision.

Apart from wind and wave measurements, Seasat SAR imagery revealed detailed patterns of complex slick patterns produced by internal waves and coastal bathymetry which might not be displayed by an optical sensor. Although the depth of penetration achieved by microwaves into sea water is

Table 2.1: Seasat SAR sensor characteristics (Jordan [53]).

Parameter	Value
Active Period	July – October 1978
Orbit Inclination	Polar 108°
Altitude	794 <i>km</i>
Nominal Speed	7450 m/sec
Antenna Dimension	10.74 × 2.16 m
Peak Power	1 kW
Swath Width	100 <i>km</i>
Look Angle	20.5° ± 3°
Frequency	1.275 GHz (L-band)
Polarization	HH
Pulse Width	33.8 μ s
Pulse Bandwidth	19 MHz
PRF	1645 Hz
A/D Rate	45.03 μ s
A/D Window	228 μ s
Processing	Optical and Digital
Azimuth Resolution	25 m
Range Resolution	25 m

less than a few millimeters, features visible on Seasat SAR images have been known to be correlated with bathymetry (Lodges [63]).

Even though Seasat was designed primarily for oceanographic experiments, it was also used to obtain very valuable radar images over the land mass for resources studies. A number of studies were conducted using Seasat imagery for geological studies (Ford [31]). Seasat SAR imagery has been proven to be very successful especially in displaying geological lineaments (Harris [40]). Radar imagery often shows significantly more lineaments than geological mapping. In regions where a geological unit can be interpreted on

the basis of a distinctive drainage pattern or geologic structure such as sand dunes, radar interpretation can be correlated accurately with the geologic map. Even some oceanographic aspects of Seasat can be of value to the geologist. The SAR imagery in coastal areas can reflect bathymetry, consequently is of value in areas where offshore exploration activities are planned.

Seasat was successful in proving that a modern microwave sensors deployed on satellites can provide very accurate data on sea surface conditions. It has also clearly demonstrated that a satellite-borne SAR system can provide geoscientists with very useful geological information as well as oceanographic informations.

2) Shuttle Imaging Radar

Instead of launching a direct successor to Seasat satellite-borne radar, NASA launched the *Shuttle Imaging Radar-A* (SIR-A) on the space shuttle Columbia in November 1981. It was not designed primarily as an oceanographic mission but as an experiment to assess the SAR system for geological mapping from a shuttle. As summarized in Table 2.2, the SIR-A system was operated in L-band (23 cm) like the Seasat SAR. However, the higher look angle was selected to enhance geologic expression. The antenna was fixed relative to the shuttle platform, at an angle of 47° to the left of the sub-nadir track. This higher look angle than that of Seasat was selected to eliminate certain effects of the lower look angle, for instance layover effect. The SIR-A data were optically recorded onto film carried on-board in a cassette, and optically processed.

Table 2.2: SIR-A and SIR-B sensor characteristics

Parameter	SIR-A	SIR-B
Active Period	November 1981	October 1984
Orbital Inclination	38°	57°
Altitude	260 <i>km</i>	225 <i>km</i>
Antenna Dimension	9.35 × 2.16 m	10.7 × 2.16 m
Peak Power	1 kW	1 kW
Swath Width	50 – 55 <i>km</i>	20 – 55 <i>km</i> (Variable)
Depression Angle	43° ± 3°	30° – 75° (Variable)
Frequency	1.282 GHz	1.282 GHz
Polarization	HH	HH
Pulse Bandwidth	6 MHz	12 MHz
Azimuth Resolution	40 m (6 look)	25 m (4 look)
Range Resolution	40 m	58 – 17 m (Variable)
Optical Data collection	8 hours	8 hours
Digital Data collection	0 hours	25 hours
Processing	Optical only	Optical and Digital

Large areas of land and ocean were covered between 40° *N* and 36° *S*, which included a number of wet tropical areas where Landsat has had difficulties in acquiring useful imagery due to cloud cover. Overall the SIR-A experiment emphasized the value of radar in providing an improved expression of topographic relief and lineaments for regional mapping.

In October 1984 the SIR-B shuttle mission was flown. The objectives were to continue geological studies by varying the look angle to test the effects of change in look angle on the geological expression. The wavelength and polarization were the same as in the SIR-A mission (Table 2.2). The SIR-B antenna was modified to permit the look angle to be changed within the range from 15° to 60°. This mission provided the first multi-look angle data

set for selected areas, useful for extracting geophysical information where there is a strong illumination angle signature.

Despite problems with the shuttle's K_u -band antenna and antenna cable during the flight, SIR-B provided relatively good quality data over a number sites and demonstrated the sensitivity of radar images to geological structural and lithologic features, to soil moisture, and to oceanic directional wave spectra [48].

The SIR-B data were the first to be digitally encoded and processed. Consequently, they have provided digitally encoded SAR images which could be quantitatively analyzed by geoscientists.

The success of the SIR-A and SIR-B missions has led to a second generation SAR design that will be used for later shuttle flights and on satellite missions. The SIR-C SAR mission, scheduled for two flights during at least different seasons in the early 1990's, will incorporate multifrequency and multipolarization features including variable incidence angle (Jordan *et al.* [54]). While Seasat, SIR-A, and SIR-B radars have operated at the single L-band frequency and single HH-polarization, SIR-C has been designed to operate simultaneously at both L- and C-band frequencies and to utilize quad-polarization returns at each frequency. An X-band, single channel VV-polarization, provided by the German Aerospace Research Establishment (DFVLR), will also be included in the mission (Jordan *et al.* [54]). In addition to the nominal mode, SIR-C will operate in some innovative modes: the squint alignment mode, the extended aperture mode, the scansar mode, and the interferometry mode (Huneycutt 1990). These new innovative modes

Table 2.3: SIR-C instrument characteristics (Jordan *et al.* [54]).

Parameter	L-Band	C-Band	X-Band
Orbital Altitude	225 km		
Antenna Size	12.0 × 2.9 m	12.0 × 0.7 m	12.0 × 0.4 m
Peak Power	3.2 kW	1.7 kW	1.4 kW
Wavelength	0.235 m	0.058 m	0.031 m
Polarization	HH,HV,VV,VH	HH,HV,VV,VH	VV
Pulse Width	33,17,8.5 μs	33,17,8.5 μs	40 μs
Pulse Bandwidth	10 and 20 MHz		
Elevation Beamwidth	4.9 – 16°	4.9 – 16°	5.5°
Azimuth Beamwidth	1.0°	0.25°	0.14°
PRF	1395 to 1736 Hz		
Resolution	30 × 30 m on the surface		

were made possible by new engineering techniques such as the electronic beam steering technique. The electronic beam steering technique helps to minimize mechanical antenna and shuttle rotations. The SIR-C instrument parameters are given in Table 2.3.

In short, SIR-C will be important for being an innovative instrument in the following three areas (Jordan *et al.* [54]):

- 1) to provide the first simultaneous multifrequency radar images from an earth-orbiting spacecraft,
- 2) to provide the first simultaneous quad-polarization images from a spaceborne high-resolution radar, and
- 3) to provide the first multiseason coverage of a multiparameter imaging radar.

3) ERS-1

The first European remote sensing satellite (ERS-1) is a programme approved and sponsored by thirteen countries: Austria, Belgium, Canada, Denmark, France, Germany, Italy, Netherlands, Norway, Spain, Sweden, Switzerland, and the United Kingdom. The ERS-1 was launched on July 16, 1991, into the 785 *km* sun synchronous circular orbit, and the expected lifetime is two to three years. The nominal ERS-1 orbit is the 3-day repetition orbit with 14 and 1/3 orbits per day and a revolution time of 100.465 minutes (Attema [3]). It is also anticipated that a second flight unit ERS-2, probably identical to ERS-1, will be launched later to provide users with five to six years of continuous data (Attema [3]).

The mission objectives are summarized as follows (Duchossois [27]):

- 1) to increase the scientific understanding of the ocean process in the coastal zones and polar regions,
- 2) to establish and develop the coastal, ocean, and ice applications of remote sensing data. Industrial applications, such as offshore petroleum activities, ship routing, and fishing activities, are also included.
- 3) to develop scientific research and applications for satellite-borne SAR data.

The ERS-1 was designed primarily to observe the surface wind and wave structure over the ocean and to provide high resolution images of the Earth's surface. Its geophysical data products are ocean surface wind speed and direction, ocean wave length and direction, and radar mapping of land, ocean,

ice, and coastal zones (Attema [3]). The major ERS-1 payload instruments consist of an Active Microwave Instrument (AMI) and K_u -band radar altimeter. These radar instruments are complemented with the infrared Along-Track Scanning Radiometer with a Microwave sounder (ATSR/M), and the Precise Range and Range Rate Equipment (PRARE) (Velten and Dieterle [104]). Measurements of each of these instruments are summarized in Table 2.4. Geophysical measurements and ERS-1 performance parameters are given in Table 2.5.

The Active Microwave Instrument (AMI) is a multimode radar operating at a frequency 5.3 GHz (C-band) using VV polarization (Table 2.6), and capable of performing in three distinct modes: the image mode, the wave mode, and the wind mode (Attema [3]). In the wind mode, the AMI is configured as a scatterometer and measures the change in radar reflectivity of the sea surface due to the perturbation of the surface by the wind. The AMI can also be operated in two SAR modes: the image mode and the wave mode. The wave mode is for smaller images ($5 \times 5 \text{ km}$) of the sea surface taken at 200 km intervals along the orbit. In this mode, the SAR is used for determination of two-dimensional ocean wave spectra of SAR images. The main purpose of the wave mode is to take radar snap shots over the ocean to measure ocean wave patterns. In the image mode, the AMI performs as a full SAR producing high quality approximately 100 km swath images over land, coastal zones, and ocean with a spatial resolution of 30 m . The output data rate in this mode (105 Mb/s) is too high to be recorded on-board. Thus the output data are transmitted to a ground station via a X-band link (8

Table 2.4: ERS-1 payload instruments and their measurement (Velten and Dieterle [104]).

- **C-band Active Microwave Instrument (AMI)**
 - **SAR**
 - * Image mode: high-resolution SAR images
 - * Wave mode: small images for ocean wave spectra
 - **Wind scatterometer**
 - * Wind mode: measuring wind fields

- **K_u -band Radar Altimeter**
 - measuring waveheight, wind speed, etc.

- **ATSR/M**
 - **Infrared Along Track Scanning Radiometer (ATSR)**
 - * measuring sea surface and cloud top temperature
 - **Microwave Sounder (M)**
 - * determination of the water vapor content

- **Precise Range and Range Rate Equipment (PRARE)**
 - measuring altitude and altitude change

- **Laser Retroreflector (LR)**
 - for satellite tracking from the ground

Table 2.5: Geophysical measurements and ERS-1 performance parameters (Duchossois [27]).

Measurement	Range	Accuracy	Instrument
Wind Field			
– Velocity	4 – 24 m/s	± 2 m/s or 10% (bigger one)	Scatterometer & Altimeter
– Direction	0 – 360°	$\pm 20^\circ$	Scatterometer
Wave Field			
– Wave Height	1 – 20 m	± 0.9 m or 10% (bigger one)	Altimeter
– Wave Direction	0 – 360°	$\pm 15^\circ$	AMI
– Wavelength	50 – 1000 m	20%	(Wave mode)
Earth Imaging	100 km	30 × 30 m	AMI
Altitude			
– Over Ocean	745 – 825 km	2 m absolute	Altimeter
– Polar Ice-Sheets		± 10 cm relative	
Satellite Range		± 10 cm	PRARE
Sea Surface Temp.	500 km swath	± 0.5 K	ATSR(IR)
Water Vapor	in 25 km spot	10%	Sounder (M)

Table 2.6: ERS-1 SAR performance requirements (Attema [3]).

Parameter	Image Mode	Wave Mode
Altitude	745 – 825 <i>km</i>	
Frequency	5.3 GHz (C-band)	
Polarization	VV	
Peak RF Power	4 kW	
Spatial Resolution		
– along track	28 m	
– cross track	26 m	
Data Rates	105 Mb/s	0.345 Mb/s
Integrated sidelobe ratio	-12 dB	
Radiometric Resolution	1.83 dB	1.73 dB
Swath width	100 <i>km</i>	6 <i>km</i>
Elevation Beamwidth	5.4°	
Azimuth Beamwidth	0.288°	
Localization accuracy		
– along track	0.35 <i>km</i>	
– cross track	0.12 <i>km</i>	

GHz).

As a forerunner of a series of satellite radar programmes planned to be launched in 1990s such as JERS-1 (Japan), Radarsat (Canada), ERS-2 (Europe), and EOS (USA), the C-band SAR on ERS-1 will provide geoscientists with much valuable data including the surface wind speed and direction over the ocean, the directional spectrum of the ocean waves, the ocean wave height, the sea surface temperature, and high resolution radar mapping.

4) JERS-1

The Japanese Earth resources satellite-1 (JERS-1) is an Earth observation satellite developed by the National Space Development Agency of Japan (NASDA) and the Ministry of International Trade and Industry (MITI), and launched in April 1992. The JER-1 carries L-band SAR and optical sensors (OPS) to observe primarily global land areas for resource exploration during its expected two-year life span. In addition to the primary objectives of geological applications, data from JERS-1 sensors will also be utilized for land survey, agriculture, forestry and fishery, environmental protection, disaster prevention and coastal monitoring (Nemoto *et al.* [85]).

The steady-state orbit of JERS-1 is a sun synchronous subrecurrent orbit. The nominal altitude of the platform is 568 *km*, which is lower than that of Seasat and ERS-1. The nominal JERS-1 orbit is the 44-day repetition orbit with 15 and 1/44 orbits per day, and a revolution time of 96.146 minutes (Nemoto *et al.* [85]). The orbit parameters of JERS-1 are given in Table 2.7.

Table 2.7: JERS-1 orbit parameters (MITI/NASDA [77]).

Parameter	Value
Nominal Altitude	568.023 <i>km</i>
Semi major Axis	6946.165 <i>km</i>
Inclination	97.662°
Revolution Period	94.146 minutes
Eccentricity	< 0.0015
Recurrent Period	44 days
Revolution/day	15 1/44 times
Drift direction	Westward
Local mean solar time (at descending node)	10:30 – 11:00 a.m.

The SAR loaded onto JERS-1 is operated at L-band and HH-polarization with 35° off-nadir angle, producing high resolution (18×18 *m* with 3 looks) images with the swath width of 75 *km*. The JERS-1 SAR is operated up to twenty minutes per revolution (Nemoto *et al.* [85]). The specifications of JERS-1 SAR is given in Table 2.8.

Optical Sensors (OPS) is also an important JERS-1 payload sensor together with SAR. This passive microwave sensor observes the Earth surface with seven spectral bands. OPS consists of two instruments: Visible and Near-Infrared Radiometer (VNIR) and Short Wavelength Infrared Radiometer (SWIR) (MITI/NASDA [77]). Specifically the SWIR is very effective for geological studies as demonstrated by Landsat TM, and will be useful discriminating lithological units on the surface. The VNIR is designed for stereoscopic observation which is to be achieved by band 4 of VNIR 15.3° (forward view) combined with band 3 of VNIR (nadir view). Both radiometers

Table 2.8: Specifications of JERS-1 SAR system (Nemoto *et al.* [85])

Parameter	Value
Antenna size	11.9 × 2.2 m
Frequency	1275 MHz (L-band)
Polarization	HH
Bandwidth	15 MHz
Pulsewidth	35 μ s
Off-nadir angle	35.21°
Swath width	75 km
Noise equivalent backscattering coeff.	-25.5 dB (maximum)
Power	about 1.1 kW (minimum)
PRF (selectable)	1505.8, 1530.1, 1555.2, 1581.1, and 1606.0 (nominal) Hz
Resolution	18 × 18 m (3 looks)
Quantization Bit No.	3 bits digitization
Down Link Data Rate	60 Mb/s (30 Mb/s × 2 channel)

cover a swath of 75 km width with 18 m ground resolution. Characteristics of OPS are given in Table 2.9.

The nadir location of images recorded by JERS-1 sensors (both SAR and OPS) is defined by the Ground Reference System (GRS) for JERS-1. The GRS is a world wide coordinate system with almost same grid spacing over the Earth's surface defined by satellite orbit "PATH number", ranging from 1 to 659, and "ROW number", ranging from 141 to 449 (Moon *et al.* [79]).

Table 2.9: Characteristics of OPS on JERS-1 (MITI/NASDA [77])

Parameter	Value
VNIR Spectral Band	Band 1: 0.52 – 0.60 μm
	Band 2: 0.63 – 0.69 μm
	Band 3: 0.76 – 0.86 μm
	Band 4: 0.76 – 0.86 μm (forward viewing)
SWIR Spectral Band	Band 5: 1.60 – 1.71 μm
	Band 6: 2.01 – 2.12 μm
	Band 7: 2.13 – 2.25 μm
	Band 8: 2.27 – 2.40 μm
View angle	7.55°
Stereo angle	15.3°
Ground resolution	18.3 × 24.2 m
Swath Width	75 km
Data rate	60 Mb/s
Digitization	6 bits

5) RADARSAT

The Radarsat, the first Canadian remote sensing satellite, is planned to be launched in 1994 (Raney *et al.* [93]). The only payload instrument is a SAR operating at a frequency of 5.3 GHz (C-band). The spacecraft is scheduled for launch into a sun synchronous near polar orbit in 1994 for a five-year mission. The satellite's five-year design life is timed to complement the earlier ERS-1 and JERS-1 programmes (Ahemed *et al.* [1]).

The orbit parameters of Radarsat are given in Table 2.10. The nominal altitude of platform will be 800 km with 98.6° inclination and an ascending node of 1800-hours local time. Radarsat will provide daily Arctic coverage,

Table 2.10: Radarsat orbit parameters (Raney *et al.* [93])

Parameter	Value
Nominal Altitude	800 <i>km</i> (793 - 821 <i>km</i>)
Orbit Inclination	98.6°
Ascending node	1800-hours local time
Period	101 minutes
Repeat cycle	24 days (343 orbits)
Sub-cycles	7 and 17 days
Re-observation	3+ days
Orbits/day	14 7/24

coverage of the Canadian land mass every 3 days, and coverage of the globe every 24 days.

The Radarsat programme objectives are based on Canadian national requirements for information to support resource management and environmental monitoring (Raney *et al.* [93]). Applications of the Radarsat SAR data include (Raney *et al.* [93]):

- 1) mapping of ice and northern region,
- 2) monitoring of agricultural, forestry and geological resources, and
- 3) maintaining an all-weather capability for Arctic observations.

The Radarsat SAR specifications are outlined in Table 2.11. A unique capability of the satellite is its ability to shape and steer the radar beam over the 500 *km* accessibility swath, and to swing the SAR beam from the right to the left side of the flight path by a yaw maneuver of the spacecraft. The SAR on Radarsat will operate at C-band (5.6 *cm* wavelength) in a variety

Table 2.11: Specifications of Radarsat SAR (Raney *et al.* [93])

Parameter	Value
Antenna size	15 × 1.5 m
Frequency	5.3 GHz
Wavelength	5.6 cm (C-band)
Polarization	HH
Pulse length	42.0 μ s
Pulse bandwidth	11.6, 17.3, or 30.0 MHz
Sampling rate	12.9, 18.5, or 32.3 MHz
PRF	1270 – 1390 Hz (2 Hz steps)
Peak power	5 kW
Average power	300 W (nominal)
Maximum time	28 min./orbit
Signal digitization	4 bits each I & Q

of commandable strip mapping modes, illuminating a swath normally to the right of nadir track.

By carrying out a 180° yaw maneuver, the SAR will operate on the left side and will then complete the entire coverage of the Antarctic region (Ahmed *et al.* [1]). The SAR sensor will be allowed to operate for a maximum of 28 minutes during any 101-minute orbital period. One of the most distinctive features of the Radarsat SAR compared with the previous spaceborne SARs is its ability to operate in various imaging modes. Specifically, it is to be the first satellite using a special radar technology known as ScanSAR which will allow imaging of a much wider swath (Raney *et al.* [93]). Each imaging mode is acquired by different resolution, swath width, and incidence angle. The eight imaging modes are summarized in Table 2.12.

Table 2.12: Radarsat imaging modes (Ahemed *et al.* 1990)

Mode	Resolution ($R_a \times A_z$, m)	Looks	Swath Width (km)	Incidence Angle (Degree)
Standard	25×28	4	100	20 – 49
Wide (1)	$48 - 30 \times 28$	4	165	20 – 31
Wide (2)	$32 - 25 \times 28$	4	150	31 – 39
Fine Resolution	$11 - 9 \times 9$	1	45	37 – 48
ScanSAR (N)	50×50	2 – 4	305	20 – 40
ScanSAR (W)	100×100	4 – 8	510	20 – 49
Extended (H)	$22 - 19 \times 28$	4	75	50 – 60
Extended (L)	$63 - 28 \times 28$	4	170	10 – 23

A variety of commandable imaging modes will be utilized to provide the most profitable SAR imagery for various research and application purposes. For instance, surveillance of large ice floes or open ocean dynamics can be carried out by a broad swath while ships and icebergs can be detected by a narrow swath at high incidence angles. Stereoscopic imagery for geologists can be obtained also by using different incidence angles.

Chapter 3

Review of Digital SAR Processors

3.1 SAR Geometry and General Principles

The antenna pattern is characterized by the width and shape of the main lobe. The width of the main lobe is usually represented by the *half-power beamwidth* defined as the angular width of the main lobe between the two angles at which the magnitude is equal to half the radiation pattern's peak value (or -3 dB on a decibel scale) (Ulaby *et al.* [103], pp.101).

A circular antenna with uniform current distribution will produce a “pencil beam” radiation pattern involving first order Bessel functions. The half-power beamwidth β in radians in this case is given by

$$\beta \simeq \frac{\lambda}{l} \quad (3.1)$$

where l is the diameter of the circular antenna and λ is wavelength (Ulaby *et al.* [103], pp.131). A rectangular antenna, more commonly used for imaging radars, with uniform current distribution will produce a “fan beam”

with sinc-function type radiation pattern. For a rectangular antenna with dimension l_1 and l_2 , the approximate expression for half-power beamwidth are given by

$$\beta_{l_1} \simeq 0.88 \frac{\lambda}{l_1}, \quad \beta_{l_2} \simeq 0.88 \frac{\lambda}{l_2} \quad (3.2)$$

where β_{l_1} and β_{l_2} are half-power beamwidth in radians corresponding to l_1 and l_2 , respectively (Ulaby *et al.* [103], p.125).

In an imaging radar, the *azimuth beamwidth* and *elevation beamwidth* are defined by the half-power beamwidth of the antenna pattern in along-track (or azimuth) dimension and cross-track (or slant range) dimension, respectively (Moore [80], pp.419). For both real and synthetic aperture radar systems, fine resolution in the cross-track direction is achieved through signal processing (Cook and Bernfeld [19]). The fundamental differences between the two systems are the technique used to achieve the azimuth resolution. The azimuth resolution of real aperture imaging radar is directly determined by the antenna beam coverage on the ground. The distance across the antenna beam for given antenna physical aperture d and radar range R is as shown in Figure 3.1

$$L \simeq \beta R \simeq \frac{\lambda}{d} R \quad (3.3)$$

where L is the distance across the antenna beam (also a azimuth resolution in the real aperture radar case). Therefore, the finer azimuth resolution of real aperture radar is obtained by making L smaller, which requires to enlarge the antenna size l . The size of an imaging radar is however limited if it is to be carried on a spacecraft or aircraft.

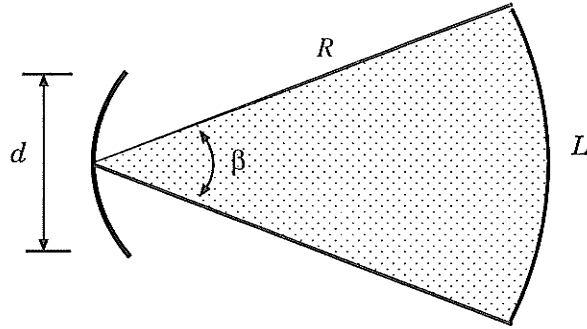


Figure 3.1: Radar beam geometry.

In order to overcome the antenna size problem, synthetic aperture radar (SAR) was developed. In SAR, finer resolution in range dimension is achieved by pulse compression technique. Unlike the real aperture radar case, the azimuth resolution of SAR, however, is determined by signal processing through the Doppler shift analysis. The synthetic array signal processing procedures can produce higher resolution images with a standard antenna. Therefore, techniques improving the azimuth resolution has become the center of interest in SAR signal processing. Problems related to the azimuth resolution are to be examined in the rest of the chapter.

The azimuth resolution of a real aperture radar, Δx_{rar} , is in proportion to the antenna illumination width, and it is from Eq.(3.3)

$$\Delta x_{rar} \simeq \frac{\lambda}{d} R . \quad (3.4)$$

There are two approaches for SAR data processing techniques: one is *unfocused* technique, and the other is *focused* technique. The focused technique is commonly adopted today in SAR processing. The unfocused technique is

introduced below for resolution comparison with the focused case.

The basic idea behind the SAR theory is that an extremely long antenna could be synthesized by using the forward motion of the platform carrying an imaging radar antenna to successive positions which could then be treated as though they were the individual antenna elements of a linear antenna array (Curtona *et al.* [22], Curtona and Hall [23]). First, a flat-surface model is assumed, which is applicable to most airborne SAR systems.

In early simpler synthetic array techniques, the coherent signals received at the synthetic array points were integrated without any attempt of shifting of the phase of signals before integration. This technique generates an unfocused synthetic aperture. The lack of phase adjustment imposes a maximum length upon the synthetic array length. As shown in Figure 3.2, a phase shift of $\lambda/4$ (i.e. 90° phase shift) of the returning wave is acceptable for the unfocused integration (Moore [80]). From the geometry given in the Figure 3.2, the maximum synthetic array effective length, L_{eff} , is given in terms of R_0 and wavelength, λ , by

$$\left(R_0 + \frac{\lambda}{8}\right)^2 = \left(\frac{L_{eff}}{2}\right)^2 + R_0^2, \quad (3.5)$$

where R_0 is the radar range at the closest approach of the antenna to a scatterer. $(\lambda/8)^2$ is negligible compared with $\lambda R_0/4$, and therefore the synthetic antenna length L_{eff} can be approximated as

$$L_{eff} \simeq \sqrt{\lambda R_0}. \quad (3.6)$$

The phase information obtained for each of the element positions of the syn-

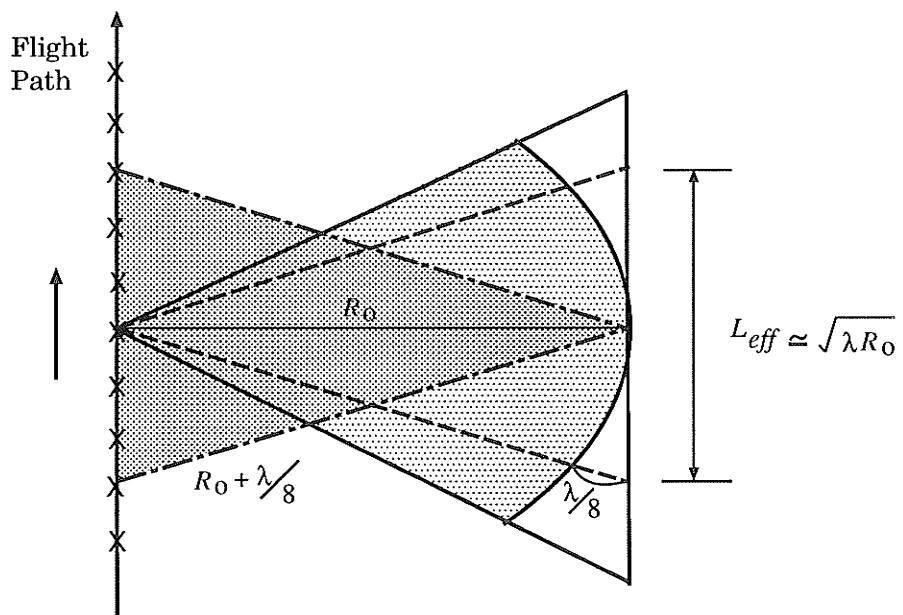


Figure 3.2: Geometry for unfocused array.

thesized antenna is based on the “round-trip” distance between the antenna and scatterers. Consequently, the beamwidth of the synthetic antenna is half that of a physical antenna (Eq.(3.1). That is,

$$\beta_{unfocused} \simeq \frac{\lambda}{2L_{eff}} \quad (3.7)$$

$$= \frac{\sqrt{\lambda}}{2\sqrt{R_0}} . \quad (3.8)$$

The achievable azimuth resolution of the unfocused synthetic aperture technique is then given by

$$\begin{aligned} \Delta x_{unfocused} &\simeq \beta_{unfocused} \cdot R_0 \\ &= \frac{1}{2} \sqrt{\lambda R_0} . \end{aligned} \quad (3.9)$$

The azimuth resolution of the unfocused synthetic aperture radar is independent of the antenna physical aperture size d (*cf.* the real aperture radar results in (Eq.3.4)), but still depends on the wavelength and radar range.

In the unfocused case, the length of synthetic aperture array is limited due to the lack of phase adjustment. If an adjustment of phase is made, a synthetic antenna array can be extended up to the distance across the antenna beam for a given radar range. This phase correction and adjustment is usually termed *focusing*, and arrays using the focusing technique are called *focused arrays*. The data processing required is adjustment of the phase of the signals received at each point of the synthetic array in order to make the signals co-phase for a given scatterer. If this can be done, the synthetic antenna length L_{eff} is

$$L_{eff} \simeq \frac{\lambda}{d} R_0 \quad (3.10)$$

which is the distance across the antenna beam given in Eq.(3.3). Similar to Eq.(3.7), the beamwidth of a focused synthetic antenna is given by

$$\beta_{focused} \simeq \frac{\lambda}{2L_{eff}} \quad (3.11)$$

$$= \frac{d}{2R_0} . \quad (3.12)$$

The maximum achievable azimuth resolution can then be obtained by multiplying this beamwidth by range, which results in

$$\Delta x_{focused} \simeq \frac{d}{2} . \quad (3.13)$$

Thus the maximum azimuth resolution of the SAR systems is one-half of the size of antenna physical aperture, and is independent of radar wavelength and range.

It should, however, be recalled that above derivation is made under a flat-Earth approximation, which is not appropriate for the spaceborne SAR configuration. It has been shown that the resolution achievable from a satellite-borne SAR is in fact much better than one-half the aperture, and is given by

$$\Delta x_{satellite} \simeq \frac{d}{2} \left(\frac{R_e}{h + R_e} \right) \quad (3.14)$$

where R_e is radius of the Earth and h is altitude of the platform (Raney [89]).

3.2 Conventional Approach

3.2.1 Matched Filter

Synthetic aperture radar achieves fine range resolution through pulse compression techniques. This section will discuss how pulse compression is accomplished.

The peak power of a radar transmitter is restricted to a certain level. The transmitted energy of a given radar can be raised by increasing the pulselength (Cook and Bernfeld [19]). The increased pulselength, however, decreases the range resolution of the radar. Thus it is desirable to raise the transmitted energy by increasing the pulselength and simultaneously to keep a high range resolution capability. To achieve this, a long pulse whose carrier frequency is phase modulated can be transmitted. On reception, the pulse must be compressed to permit separation of adjacent range resolution cells. The pulse compression is achieved through matched filtering (Bernfeld *et al.* [9]). Matched filtering constitutes the optimum predetection processing of radar signal assuming that signals are corrupted by white Gaussian noise (Bernfeld *et al.* [9]).

A linear frequency modulated (FM) pulse with rectangular envelope of pulse duration T is given as

$$s(t) = A \cos \left(\omega_0 t + \frac{\mu}{2} t^2 \right) \quad -\frac{T}{2} \leq t \leq \frac{T}{2} \quad (3.15)$$

where the carrier frequency is of the linear form

$$\omega = \omega_0 + \mu t \quad -\frac{T}{2} \leq t \leq \frac{T}{2} \quad (3.16)$$

where ω_0 is a angular center frequency, $\mu = 2\pi\Delta f/T$ is the FM slope, and A is a constant amplitude. Figure 3.3 shows a transmitted rectangular waveform of a linear FM pulse characterized by the lower frequency components at the beginning and the higher frequency components at the end of the pulse. The return echo at the receiver will be similar to the transmitted signal in time-frequency characteristics as shown in Figure 3.4 (a) and (b). If the receiver acts, as shown in Figure 3.4 (c), to delay the lower frequency components more than the higher frequency components at the end of the pulse, this is a time compression of the pulse as shown in Figure 3.4 (d).

This time delay filter is characterized by the inverse time-frequency slope in comparison with that of the transmitted pulse, and is called a *matched filter*. The characteristics of a matched filter are (Cook and Bernfeld 1967):

- 1) If the signal spectrum is described by $s(\omega)$, then the frequency response function $H(\omega)$ of a filter that results in a maximum signal-to-noise ratio for the filter output is the complex conjugate of the spectrum function, or $H(\omega) \propto s(\omega)^*$.
- 2) If the signal waveform is defined by $s(t)$, impulse response of the filter meeting the condition of 1) is the time inverse of the signal $s(t)$, that is $h(t) \propto s(-t)$.

Thus the impulse response of the filter matched to the signal in Eq.(3.15) is

$$\begin{aligned}
 h(t) &= \sqrt{\frac{2\mu}{\pi}} s(-t) \\
 &= \sqrt{\frac{2\mu}{\pi}} \cos\left(\omega_0 t - \frac{\mu t^2}{2}\right) \quad -\frac{T}{2} \leq t \leq \frac{T}{2}
 \end{aligned} \tag{3.17}$$

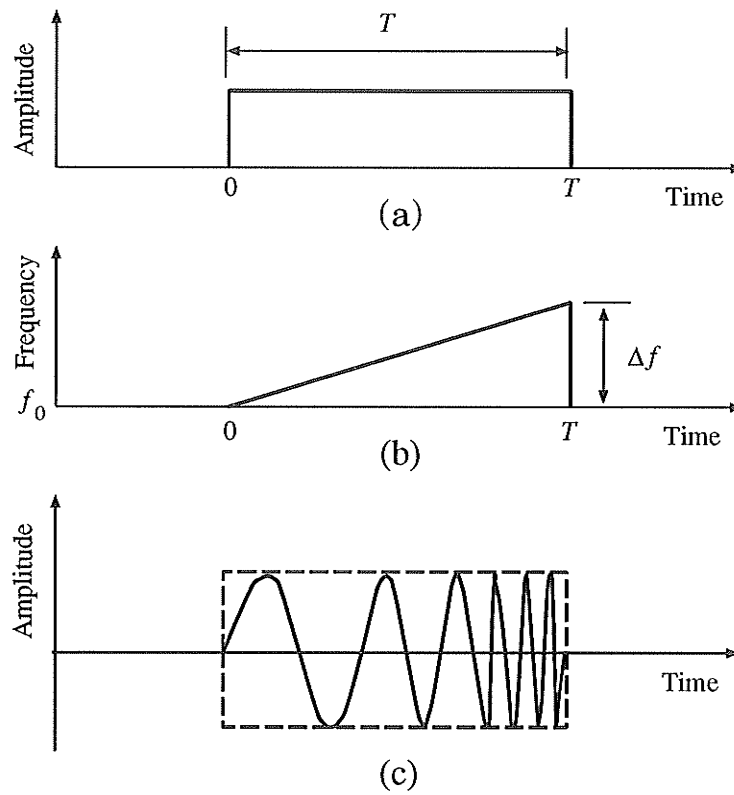


Figure 3.3: Transmitted waveform of a linear frequency modulated pulse: (a) rectangular pulse envelope, (b) time-frequency characteristic of linear FM signal, (c) waveform of a linear FM signal.

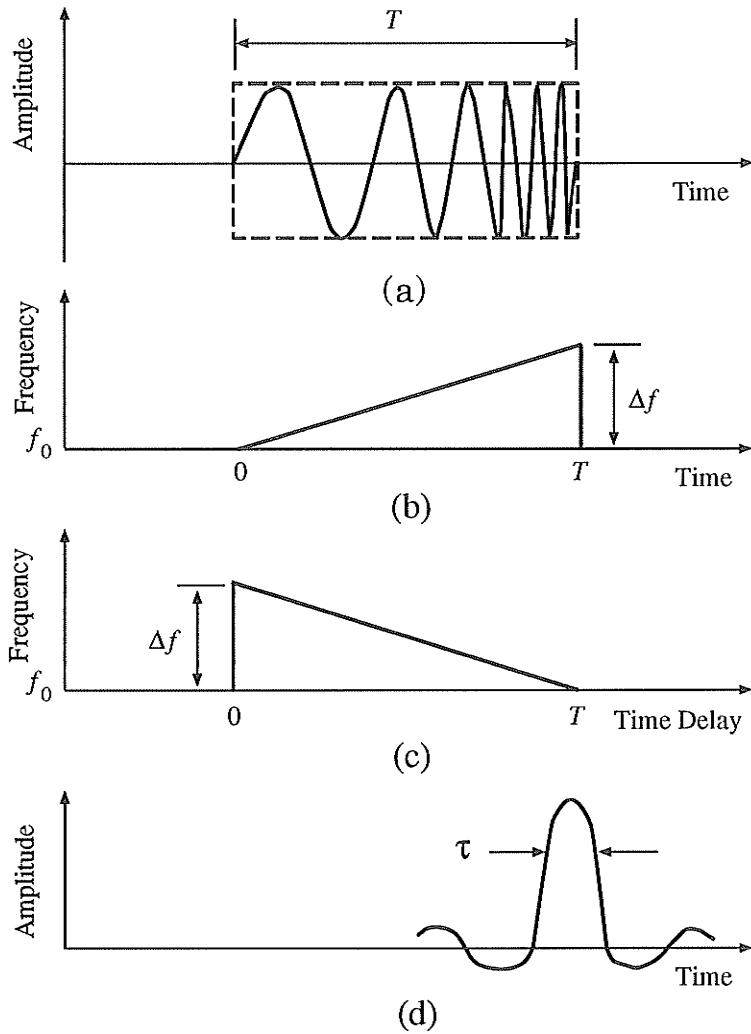


Figure 3.4: Received waveform of the linear frequency modulated pulse and subsequent pulse compression: (a) waveform of the received signal, (b) time-frequency characteristic of the received signal, (c) time-frequency characteristic of the matched filter, (d) a compressed pulse after matched filtering.

where the $\sqrt{2\mu/\pi}$ is a normalization factor that results in unit gain at ω_0 . The matched-filter output signal is then

$$\begin{aligned}
g(t) &= \int_{-\infty}^{\infty} s(\tau)h(\tau - t) d\tau \\
&= \sqrt{\frac{2\mu}{\pi}} \int_{-\infty}^{\infty} s(\tau)s(t - \tau) d\tau \quad . \\
&= \sqrt{\frac{2\mu}{\pi}} \int_{-T/2}^{T/2} \cos\left(\omega_0\tau + \frac{\mu\tau^2}{2}\right) \cos\left(\omega_0(t - \tau) - \frac{\mu(t - \tau)^2}{2}\right) d\tau \quad .
\end{aligned} \tag{3.18}$$

The input to a radar receiver will not be an exact replica of the transmitted signal, because the SAR signal has undergone a Doppler shift. The Doppler shift occurs when the signal is reflected from an object that has a radial velocity component relative to the radar system. When a Doppler shift is included, the general output of the matched filter becomes

$$\begin{aligned}
g(t; \omega_d) &= \sqrt{\frac{2\mu}{\pi}} \int_a^b \cos\left((\omega_0 + \omega_d)\tau + \frac{\mu\tau^2}{2}\right) \cdot \\
&\quad \cos\left(\omega_0(t - \tau) - \frac{\mu(t - \tau)^2}{2}\right) d\tau \quad (3.19)
\end{aligned}$$

where

$$\begin{cases} a = -T/2 + t, & b = T/2 & t > 0 \\ a = -T/2, & b = T/2 + t & t < 0 \end{cases}$$

and ω_d is the Doppler frequency shift. When $\omega_d = 0$, $g(t)$ is the ‘‘autocorrelation’’ function of the input signal. When $\omega_d \neq 0$ which is general case for the SAR signals, $g(t; \omega_d)$ is the ‘‘cross correlation’’ of the two functions, representing all possible matched filter outputs for the moving object condition (Cook and Bernfeld [19]). The closed form solution of Eq.(3.19) can be

approximated by

$$g(t; \omega_d) \simeq \sqrt{\frac{2\mu}{\pi}} \frac{\sin [(T - |t|)(\omega_d + \mu t)/2]}{\mu t} \cos(\omega_o + \frac{\omega_d}{2}) t \quad -T \leq t \leq T \quad (3.20)$$

(Bernfeld *et al.* 1964).

The compressed pulse is readily recognized from Eq.(3.22) as having a sinc-function ($\sin x/x$) form. Figure 3.5 shows amplitude-time characteristics of an ideal matched filter output signal. The 4 dB down pulsewidth is $\tau = 1/\Delta f$ as shown in Figure 3.5. The spacing between the first zeros of this envelope is $2/\Delta f$, and the peak amplitude is $\sqrt{T\Delta f}$. The pulse compression ratio (T/τ) is

$$\frac{T}{\tau} = \frac{T}{(1/\Delta f)} = T\Delta f \quad , \quad (3.21)$$

thus the *time-bandwidth product* (TBP) determines the pulse compression ratio of the input signal to the matched filter output signal.

For a special case of $\omega_d = 0$, $g(t, \omega_d = 0)$ reduces to

$$g(t) \simeq \sqrt{\frac{2\mu}{\pi}} \frac{\sin [(T - |t|)(\mu t/2)]}{\mu t} \cos \omega_o t \quad -T \leq t \leq T \quad . \quad (3.22)$$

When the Doppler shift ω_d is not zero, there exist: phase shift, time shift of the waveform, loss in peak amplitude, and broadening of the pulse width. The maximum value of $g(t; \omega_d)$ in Eq.(3.20) occurs at $\omega_d + \mu t = 0$. Thus the value of the time shift t_s is

$$t_s = -\frac{\omega_d}{\mu} = -\frac{f_d}{\Delta f} T \quad (3.23)$$

where f_d is the frequency shift due to a Doppler shift.

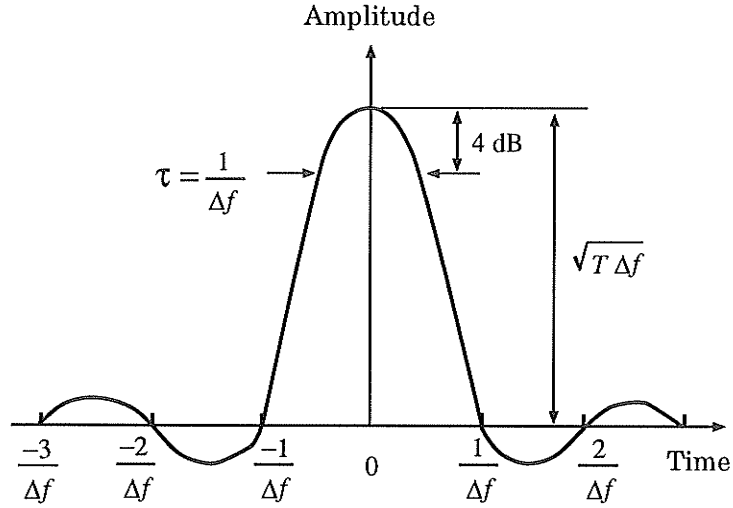


Figure 3.5: Amplitude-time characteristics of an ideal matched filter output signal for $\omega_d = 0$.

It is of interest to analyze the matched filter in terms of its transfer function being the complex conjugate of the transmitted signal. The Fourier transform of the linear FM signal is expressed by

$$\begin{aligned}
 s(\omega) &= \int_{-T/2}^{T/2} \cos\left(\omega_0 t + \frac{\mu t^2}{2}\right) e^{-i\omega t} dt \\
 &= \frac{1}{2} \int_{-T/2}^{T/2} \exp\left[i\left((\omega_0 - \omega)t + \frac{\mu t^2}{2}\right)\right] dt \\
 &\quad + \frac{1}{2} \int_{-T/2}^{T/2} \exp\left[-i\left((\omega_0 + \omega)t + \frac{\mu t^2}{2}\right)\right] dt .
 \end{aligned} \tag{3.24}$$

The second integral is the negative frequency portion of the spectrum, and consequently creates a negligible contribution at positive frequencies if the ratio of center frequency (ω_0) to bandwidth ($\Delta\omega$) is sufficiently large. Then

$s(\omega)$ is rewritten as

$$s(\omega) \simeq \frac{1}{2} e^{-i(\omega-\omega_0)^2/2\mu} \int_{-T/2}^{T/2} \exp \left[i \frac{\mu}{2} \left(t - \frac{\omega - \omega_0}{\mu} \right)^2 \right] dt . \quad (3.25)$$

Through a change of variable, $s(\omega)$ reduces to

$$s(\omega) = \frac{1}{2} \sqrt{\frac{\pi}{\mu}} e^{-i(\omega-\omega_0)^2/2\mu} [C(X_+) + C(X_-) + i(S(X_+) + S(X_-))] \quad (3.26)$$

where

$$X_{\pm} = \frac{\mu/2 \pm (\omega - \omega_0)}{\sqrt{\pi\mu}} \quad (3.27)$$

the subscript \pm corresponds to the signs in the numerator, and

$$C(x) = \int_0^x \cos \frac{\pi y^2}{2} dy, \quad S(x) = \int_0^x \sin \frac{\pi y^2}{2} dy \quad (3.28)$$

are the Fresnel integrals (Bernfeld *et al.* 1964).

In Eq.(3.26), the phase spectrum of the linear FM signal consists of two terms: one is the square-law phase term

$$\Phi_1(\omega) = \frac{(\omega - \omega_0)^2}{2\mu} \quad (3.29)$$

and the other is the residual phase term

$$\Phi_2(\omega) = -\tan^{-1} \left[\frac{S(X_+) + S(X_-)}{C(X_+) + C(X_-)} \right] . \quad (3.30)$$

For large values of $T\Delta f$ (TBP) (i.e., $T\Delta f > 30$, Cook and Bernfeld [19], p.140), the ratio

$$\frac{S(X_+) + S(X_-)}{C(X_+) + C(X_-)} \approx 1 \quad (3.31)$$

and thus the residual phase term Φ_2 approximates to a constant $\pi/4$. Since $\mu = 2\pi\Delta f/T$ and $(\omega - \omega_0) = 2\pi n\Delta f/2$, the argument of the Fresnel integrals in Eq.(3.27) becomes

$$X_{\pm} = \sqrt{T\Delta f} \left(\frac{1 \pm n}{\sqrt{2}} \right) \quad (3.32)$$

where n is a normalized frequency parameter. The spectra in Eq.(3.26) are thus functions of the time-bandwidth product $T\Delta f$ (i.e. compression ratio T/τ).

During design of a matched filter, weighting is usually included to reduce side lobes. The first, and largest, sidelobe of an ideal matched filter output signal is only 13 dB below the peak of the compressed pulse and near sidelobes fall off at approximately 4 dB per sidelobe interval, with the sidelobe null points being spaced $1/\Delta f$ apart. To reduce the undesirable sidelobes, there are various approaches such as weighting the spectrum by frequency domain filtering, or amplitude weighting of the envelope of the transmitted FM signal in the time domain. The frequency domain weighting is generally adopted (Cook and Bernfeld [19]).

3.2.2 Doppler Phase History

The azimuth compression of the SAR signal is based on the analysis of Doppler shift along an array. Thus the image formation out of SAR data requires accurate estimation of the expected phase histories of scatterers on the Earth's surface. It is the sequence of relative distances between the moving sensor and a scatterer that determines its phase history. For convenience, a flat-surface model is assumed first and the orbital SAR case will be

discussed later in this section.

Three vectors which describe the position, velocity, and acceleration of the sensor are denoted by $\mathbf{R}_s(t)$, $\mathbf{V}_s(t)$, $\mathbf{A}_s(t)$ respectively. The corresponding vectors for a scatterer on the surface are given by $\mathbf{R}_t(t)$, $\mathbf{V}_t(t)$, $\mathbf{A}_t(t)$ as displayed in Figure 3.6. Because the relative motion is more important, the vectors $\mathbf{R}(t)$, $\mathbf{V}(t)$, $\mathbf{A}(t)$ are defined by

$$\begin{aligned}\mathbf{R}(t) &= \mathbf{R}_s(t) - \mathbf{R}_t(t) \\ \mathbf{V}(t) &= \mathbf{V}_s(t) - \mathbf{V}_t(t) \\ \mathbf{A}(t) &= \mathbf{A}_s(t) - \mathbf{A}_t(t)\end{aligned}\tag{3.33}$$

which describe the relative motion between the sensor and scatterer. In a short time interval centered at t_0 , the distance can be expressed by

$$\mathbf{R}(t) = \mathbf{R}(t_0) + \mathbf{V}(t_0)(t - t_0) + \frac{1}{2}\mathbf{A}(t_0)(t - t_0)^2 .\tag{3.34}$$

The norm of the vector is

$$\begin{aligned}|\mathbf{R}(t)| &= \sqrt{\mathbf{R}(t) \cdot \mathbf{R}(t)} \\ &\simeq |\mathbf{R}(t_0)| + \frac{\mathbf{R}(t_0) \cdot \mathbf{V}(t_0)}{|\mathbf{R}(t_0)|}(t - t_0) \\ &\quad + \frac{(\mathbf{V}(t_0) \cdot \mathbf{V}(t_0) + \mathbf{R}(t_0) \cdot \mathbf{A}(t_0))}{2|\mathbf{R}(t_0)|}(t - t_0)^2\end{aligned}\tag{3.35}$$

where $|\mathbf{R}(t_0)|$ is a magnitude of $\mathbf{R}(t_0)$ and \cdot denotes a dot product. The return signal is time delayed by $2|\mathbf{R}(t_0)|/c$, thus the phase shift due to the signal time delay is

$$\Phi(t) = -\frac{2}{\lambda}2\pi|\mathbf{R}(t)|\tag{3.36}$$

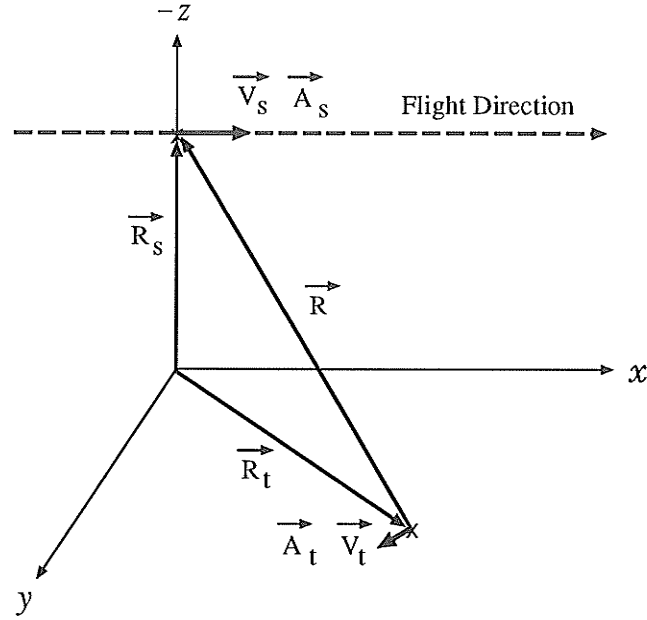


Figure 3.6: Sensor and scatterer geometry for Doppler parameters.

where λ is wavelength of the signal. The instantaneous frequency is given by

$$f(t) = \frac{1}{2\pi} \frac{d\Phi(t)}{dt} . \quad (3.37)$$

Thus the Doppler shift becomes

$$\begin{aligned} f_D(t) &= -\frac{2}{\lambda} \frac{d|\mathbf{R}(t)|}{dt} \\ &\equiv f_{DC} + f_{DR}(t - t_0) \end{aligned} \quad (3.38)$$

where the *Doppler frequency*, f_{DC} , and the *Doppler frequency rate*, f_{DR} , are approximated by

$$f_{DC} \simeq -\frac{2}{\lambda} \frac{\mathbf{R}(t_0) \cdot \mathbf{V}(t_0)}{|\mathbf{R}(t_0)|} \quad (3.39)$$

$$\begin{aligned}
f_{DR} &\simeq -\frac{2}{\lambda} \frac{(\mathbf{V}(t_0) \cdot \mathbf{V}(t_0) + \mathbf{R}(t_0) \cdot \mathbf{A}(t_0))}{|\mathbf{R}(t_0)|} \\
&= \frac{df_{DC}}{dt} .
\end{aligned} \tag{3.40}$$

From Eq.(3.36) and Eqs.(3.39) and (3.40), the Doppler phase history is approximated by

$$\Phi(t) \simeq \Phi(t_0) + 2\pi \left(f_{DC}(t - t_0) + \frac{1}{2} f_{DR}(t - t_0)^2 \right) \tag{3.41}$$

where

$$\Phi(t_0) = -\frac{4\pi}{\lambda} |\mathbf{R}(t_0)| . \tag{3.42}$$

Thus the Doppler history represents a linear FM signal in the azimuth dimension centered at f_{DC} having a slope of f_{DR} . Consequently the signal along azimuth dimension can be compressed through a matched filter processing the same way as the range pulse compression is achieved.

However, there exist some difficulties in applying a matched filter for the azimuth compression directly. An accurate estimation of the Doppler frequency and the Doppler frequency rate used for azimuth reference function are first required. In addition, both the Doppler frequency f_{DC} and the Doppler frequency rate f_{DR} vary with range $\mathbf{R}(t_0)$. Thus both parameters must be repeatedly updated over the swath width (Wu *et al.* [112]).

Apart from accurate estimation of Doppler parameters, a severe difficulty in implementing an azimuth matched filter is associated with the *range migration*. The Doppler phase change in Eq.(3.36) results from change in the range between the sensor and scatterer. The locus of a scatterer in the range-azimuth domain is represented not by a straight line but by a curve

because of the change in range. This effect is known as range migration. If the change in range is smaller than one-half of the range resolution, the locus approximates to a straight line (Bennett and Cumming [6]). Many airborne SAR systems are designed to avoid range migration. On the other hand, if the change in range is greater than one-half range resolution, then the azimuth samples to be used for azimuth compression must be collected along the locus of each point scatterer (Bennett and Cumming [6]). Range migration is directly associated with Doppler phase history, and is a combination of the *range walk* and the *range curvature*. The range walk is correlated with the Doppler frequency f_{DC} , and the range curvature with the Doppler frequency rate f_{DR} . The range walk and range curvature are shown in Figure 3.7.

In the case of a spaceborne SAR, the Doppler phase history must take into account the circular nature of orbit, Earth's curvature, and Earth's rotation effect additionally. An excellent discussion about the Doppler phase history of a spaceborne SAR system may be found in Raney [90]. One problem emphasized in the orbital SAR configuration is that the radar footprint velocity, the rate at which the Earth's surface is covered by radar beam, must be discriminated from the platform velocity (Raney [90]). For the flat-surface model, two velocities have the same value.

The geometry used for formulating Doppler parameters of spaceborne SAR is displayed in Figure 3.8. When the circular orbital SAR configuration is taken into account, the Doppler frequency is more precisely expressed by

$$f_{DC} \simeq \frac{2V_s}{\lambda} \sin \theta \cos \alpha \left\{ 1 - \frac{\omega_e}{\omega_s} (\varepsilon \cos \chi \sin \psi \tan \alpha + \cos \psi) \right\} \quad (3.43)$$

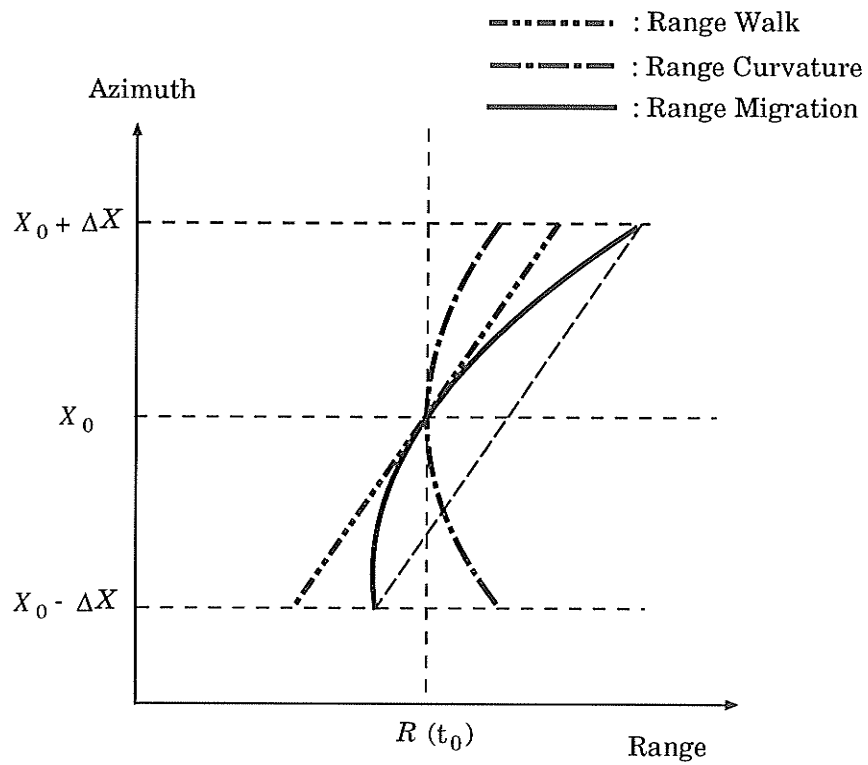


Figure 3.7: Range walk, range curvature, and range migration.

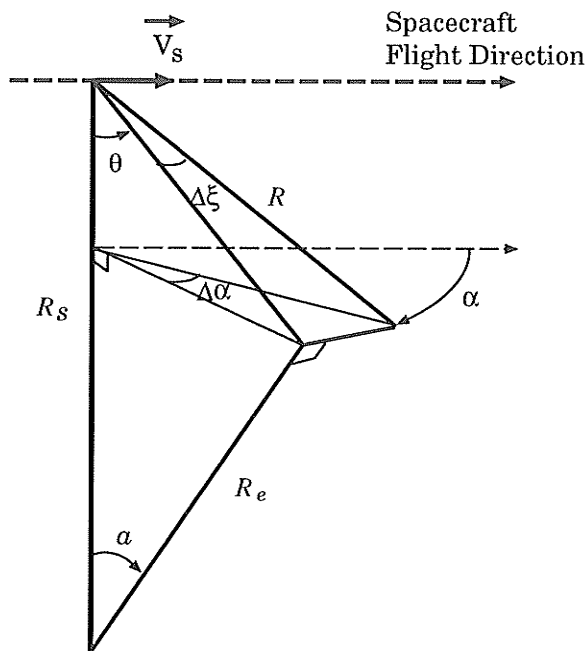


Figure 3.8: Spaceborne SAR geometry for Doppler parameters.

where ω_e and ω_s are respectively the Earth rotation rate and spacecraft orbital rotation rate, χ is latitude, ψ is orbital inclination, and ε is indicator variable: $\varepsilon = 1$ if radar looks to the right side, and $\varepsilon = -1$ if radar looks to the left (Raney [90]). The first term in Eq.(3.43) arises from the platform motion, and it is same as the Eq.(3.39). The remaining two terms in Eq.(3.43) are caused by Earth rotation.

The Doppler frequency rate now can be directly derived by taking the time derivative of the Doppler frequency in Eq.(3.43). For the given geometry, it can be shown that $d\alpha/dt = V_g/R \sin \theta$ where V_g is radar footprint velocity, and $d\chi/dt = \omega_s$ by definition. The resulting Doppler frequency rate for an

orbital SAR is given by

$$\begin{aligned}
 f_{DR} \simeq & -\frac{2V_s V_g}{R\lambda} \left\{ 1 - 2\frac{\omega_e}{\omega_s} (\cos \psi + \sin \alpha \sin \chi \tan a \sin \psi) \right. \\
 & + \frac{\omega_e^2}{\omega_s^2} (1 - \sin^2 \chi \sin^2 \psi) \\
 & \left. + \frac{\omega_e^2}{\omega_s^2} \sin \chi \sin \psi \tan a (\cos \psi \sin a - \sin \psi \cos \chi \cos a) \right\}
 \end{aligned} \tag{3.44}$$

(Raney [91]). It is noted that the Doppler frequency rate depends only on the relative location of a scatterer with respect to the sensor.

3.2.3 Conventional Digital SAR Processors

Early works on digital SAR processing techniques can be found in Brown *et al.* [13], Kirk [55], and Martinson [74]. These authors did not yet provide a full-scale processing scheme for digital SAR image reconstruction. More detailed and complete digital SAR processing schemes were discussed by Wu [109], van de Lindt [60], and Bennett and Cumming [6] [7]. The principal strategy of these algorithms is such that the SAR imagery can be reconstructed by two sequential correlations of the return signal with the range reference function first and then by the azimuth reference function second, through fast correlation approach using the one-dimensional fast Fourier transform (FFT). The flow chart for the algorithm is shown in Figure 3.9.

The mathematical model of the SAR return signal may help the algorithm to be better understood. A SAR system generally transmits and receives signal using the same antenna. During the transmission over a pulse duration T , the frequency is linearly modulated or “chirped”, while the frequency

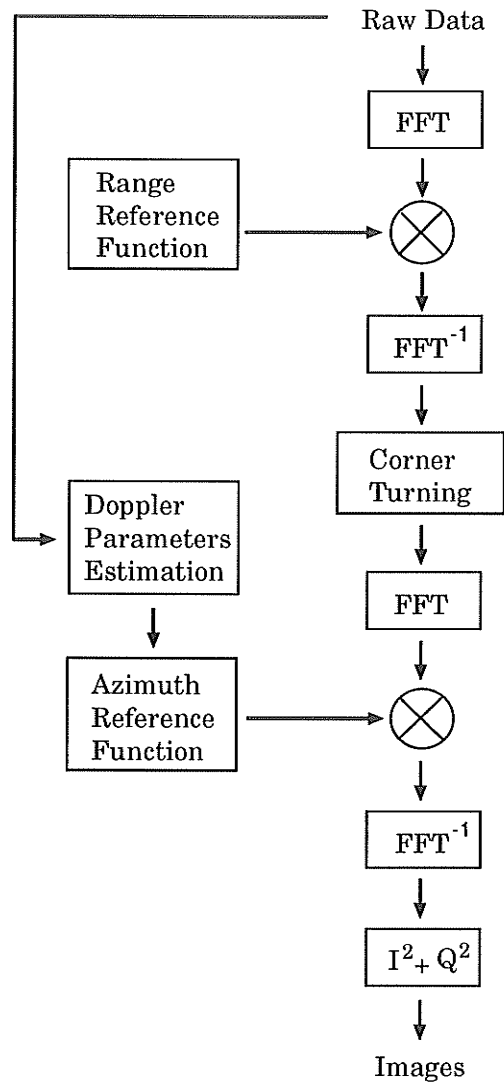


Figure 3.9: Flow chart of a conventional range-Doppler SAR processor (Wu 1976).

is constant during the receiving period. Each transmitted pulse can be described by

$$s(x, t) = \cos(w_0 t + \mu t^2) \quad (3.45)$$

where w_0 is a carrier frequency, and the FM slope μ . In Eq.(3.45), the pulse envelope was not included. A detailed formula for the pulse envelope can be found in van de Lindt [60].

The signal returned from a scatterer located at $R(x, \eta)$ has time-delayed from transmission by $2R(x, \eta)/c$, and is given by

$$s(x, t; \eta) = \cos \left\{ \omega_0 \left(t - \frac{2}{c} R(x, \eta) \right) + \mu \left[t - \frac{c}{2} R(x, \eta) \right]^2 \right\} \quad (3.46)$$

where η is slant range at the closest approach of an antenna as shown in Figure 3.10. After quadrature demodulation at the receiver, the signal returned from a point scatterer can be written as

$$\begin{aligned} s(x, t; \eta) &= \exp \left\{ i\mu \left[t - \frac{c}{2} R(x, \eta) \right]^2 \right\} \exp \left\{ -i \frac{4\pi}{\lambda} R(x, \eta) \right\} \quad (3.47) \\ &\equiv h_1(x, t; \eta) h_2(x, t; \eta) \end{aligned}$$

where the wavelength $\lambda = 2\pi c/\omega_0$. The first term $h_1(x, t; \eta)$ accounts for the range chirp and range migration. The second term $h_2(x, t; \eta)$ is the Doppler phase shift discussed in the previous section. In conventional approaches (Figure 3.9), the range compression is carried out first through the fast FFT correlation. The Fourier transform of $h_1(x, t; \eta)$ with respect to t is given by

$$h_1(x, \omega; \eta) = \exp \left\{ -i \frac{\omega^2}{4\mu} \right\} \exp \left\{ -i \frac{2}{c} R(x, \eta) \omega \right\} . \quad (3.48)$$

The range matched filtering is achieved by multiplying $h_1(x, \omega; \eta)$ by a complex conjugate function of $\exp\{-i\omega^2/4\mu\}$. The inverse Fourier transform

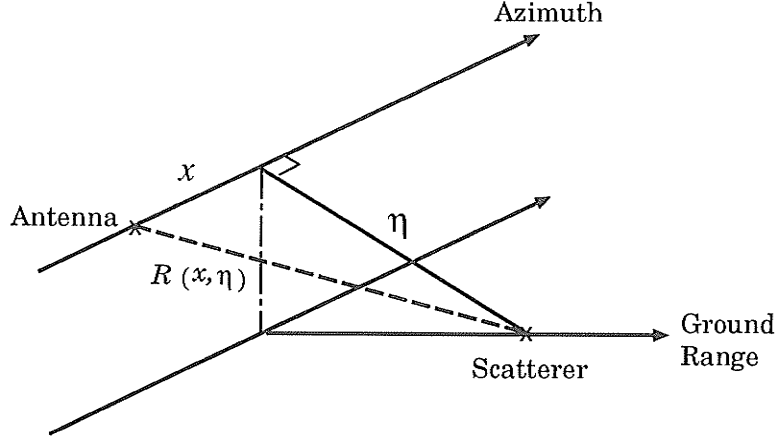


Figure 3.10: Geometry for a sensor and scatter coordinate.

with respect to ω (third step in Figure 3.9) after matched filtering results in a range compressed signal given as

$$s(x, t; \eta) = \delta \left(t - \frac{2}{c} R(x, \eta) \right) \exp \left\{ -i \frac{4\pi}{\lambda} R(x, \eta) \right\} . \quad (3.49)$$

A key approximation used in conventional approaches is a quadratic approximation of range $R(x, \eta)$ to be

$$\begin{aligned} R(x, \eta) &= \sqrt{x^2 + \eta^2} \\ &\simeq \eta + \frac{x^2}{2\eta} . \end{aligned} \quad (3.50)$$

Using this quadratic approximation, the range compressed signal is then approximated to

$$s(x, t; \eta) \simeq \delta \left(t - \frac{2}{c} \eta - \frac{x^2}{c\eta} \right) \exp \left\{ -i \frac{4\pi}{\lambda} \left(\eta + \frac{x^2}{2\eta} \right) \right\} . \quad (3.51)$$

Conventional approaches perform the range migration correction and the azimuth compression in the range-Doppler domain based on Eq.(3.51) (Wu

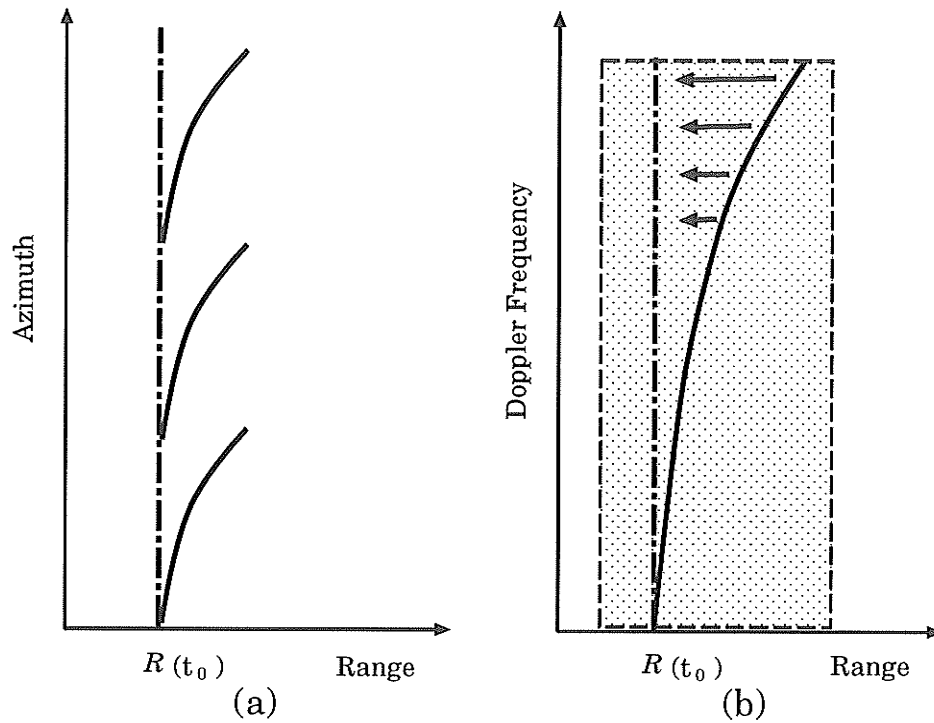


Figure 3.11: Range migration due to multiple scatterers (a) in the range-azimuth domain, and (b) in the range-Doppler domain.

[109], Bennett and Cumming [6], and van de Lindt [60]). The advantage of the range-Doppler approach over the range-azimuth domain processing was discussed by Bennett and Cumming [6]. The locuses of scatterers, which locate at the same range but at different azimuth, in the range-azimuth domain are shown in Figure 3.11 (a). These locuses map into a single frequency spectrum trajectory in range-Doppler domain as in Figure 3.11 (b). Thus straightening the curvature of the single trajectory in the range-Doppler domain will straighten the curvature of whole family of equal range trajectories

in range-azimuth domain (Bennett and Cumming [6]).

The Fourier transform of $s(x, t; \eta)$ with respect to the azimuth x is given by

$$s(k_x, t; \eta) \sim \sqrt{i \frac{\lambda \eta}{2}} e^{-i4\pi\eta/\lambda} \delta \left(t - \frac{2}{c}\eta - \frac{c\eta}{4} \frac{k_x^2}{\omega_0^2} \right) \exp \left\{ i \frac{c\eta}{4} \frac{k_x^2}{\omega_0} \right\} \quad (3.52)$$

where k_x is the azimuth wavenumber or spatial angular Doppler frequency. The detailed derivation for the Eq.(3.52) is summarized in Appendix C. The exponential term $\exp(-i4\pi\eta/\lambda)$, whose phase is found in Eq.(3.42), is independent of k_x , and thus is not so important as the k_x -dependent last two terms.

The range migration correction in the range-Doppler domain is performed as a time shift by

$$\Delta t(k_x) \simeq -\frac{c\eta}{4} \frac{k_x^2}{\omega_0^2}. \quad (3.53)$$

This time shift process requires a range domain interpolation, which is often difficult to achieve with high accuracy. Errors due to interpolation result in image blurring and the loss of phase information. In addition, this range migration correction formula is not exact but based on a quadratic approximation of $R(x, \eta)$ in Eq.(3.50).

After the range migration correction, the azimuth compression of conventional approaches in the range-Doppler domain is performed using a reference function given by

$$\exp \left\{ -i \frac{c\eta}{4} \frac{k_x^2}{\omega_0} \right\} \quad (3.54)$$

which is a complex conjugate of the last exponential term in Eq.(3.52). It is of interest to compare the conventional azimuth reference function in Eq.(3.54)

with a formula developed in this thesis work which will be discussed in the following chapter. From Eq.(4.36), the corresponding function in the f - k domain can be approximated as

$$\exp \left\{ -i \frac{c\eta}{4(\omega_0 + \omega)} k_x^2 \right\} \sim \exp \left\{ -i \frac{c\eta}{4\omega_0} k_x^2 \left(1 - \frac{\omega}{\omega_0} \right) \right\}, \quad (3.55)$$

since the carrier frequency ω_0 is usually much larger than bandwidth ω . The inverse Fourier transform of Eq.(3.55) with respect to ω is given by

$$\delta \left(t + \frac{c\eta}{4} \frac{k_x^2}{\omega_0^2} \right) \exp \left\{ -i \frac{c\eta}{4} \frac{k_x^2}{\omega_0} \right\}, \quad (3.56)$$

which corresponds to the azimuth reference function of conventional approaches given in Eq.(3.54). Therefore, conventional approaches account for up to the first order approximation of ω/ω_0 in the azimuth compression.

To improve performance of the azimuth compression, modified approaches have been developed by Wu *et al.* [112], and Jin and Wu [52]. A limited two-dimensional processing for azimuth correlation was also suggested to achieve higher quality imagery by Wu *et al.* [110]. In this approach, a data block of several neighboring azimuth lines, marked by shaded area in Figure 3.11 (b), is used for a azimuth correlation without interpolation. The reference function is also a limited two-dimensional array, so the two-dimensional correlation in azimuth will be combination of frequency domain fast correlation in the azimuth domain and a time-domain convolver type operation in the range dimension. With this approach, errors due to interpolation step can be avoided but the processing efficiency decreases rapidly as the amount of range migration increases. Specifically the SIR-B data yielded a larger

amount of range migration than Seasat data because of variation in look angle and reduced antenna pointing accuracy. To accommodate large range migration, Jin and Wu [52] developed another method of two cascaded one-dimensional correlation: the azimuthal-range compression performing first a range convolution to correct the range-dispersed spectrum, and then an azimuth compression using a plain frequency-domain range migration correction approach.

Details of these algorithms are beyond the scope of this thesis. In general, the required image resolutions have been satisfied by these conventional range-Doppler processors. However, it must be stated that further improvements upon digital SAR processors has become necessary to accommodate the range curvature accurately and to achieve better azimuth focusing.

Chapter 4

Theoretical Development

4.1 Background Review

As briefly reviewed in the previous chapter, the conventional digital SAR processors are based on the one-dimensional matched filtering processes in both range and azimuth dimension. Specifically the azimuth compression of the conventional approaches must be incorporated with range-migration correction which requires interpolation in the range-Doppler domain. The performance and efficiency of a conventional SAR processor therefore depends very much upon the range-migration correction. Moreover, the azimuth transfer function of conventional approaches accounts for only quadratic approximation of Doppler shift.

In recent years several SAR processing approaches, utilizing f - k domain processing, have been reported.

Di Cenzo [26] suggested a direct two-dimensional correlation approach through a two-dimensional Fourier transform. The method reported is essentially a two-dimensional correlation of data with a two-dimensional SAR

template which represents the complex pulse returns received from a point scatterer at a specified location. Although this approach utilizes f - k domain operations for fast two-dimensional correlation, it is only an extended version of the conventional SAR processing approach.

Two other more recent approaches are more distinct in the context of the f - k domain processing. Rocca *et al.* [96] have showed similarities between reflection seismic survey and SAR data acquisition configuration, and developed a SAR processing algorithm utilizing f - k domain processing. This approach is based on the seismic migration theory. Raney and Vachon [92] also developed a phase-preserving SAR processor by exploiting the phase shifts in the f - k domain solely from the analysis of the SAR system theory.

Although, the above two approaches started from quite different points of view with respect to SAR signal data, both approaches utilize f - k domain processing and have proved its advantages over the conventional range-Doppler domain processors. The key to the success of these approaches lies in the fact that a small adjustment of the phase in the f - k domain achieves the range-curvature correction without significantly disturbing the range or azimuth focus.

Development of a new SAR processing approach in this thesis is motivated by the successful application reported in the seismic migration research described by Rocca *et al.* [96]. Unlike the seismic migration approach, the new SAR processing approach in this thesis is, however, based on an inverse scattering theory. Specifically inversion of the SAR image data is formulated in similar fashion to the seismic Born inversion method which has been

developed and discussed by several authors such as Cohen and Bleistein [17] [18], Bleistein [10], Cheng and Coen [16], Bleistein *et al.* [11], and Wenzel [107].

While the Born inversion theory provides a mathematical consistency for both the acquisition and the inversion of the data, the seismic migration schemes are generally based on a heuristic seismic model such as the exploding reflector model. The exploding reflector model can be summarized as follows: reflectors explode simultaneously at a certain time, let us say $t = 0$, and waves travel upward in a medium with half the true velocity. Thus the seismic migration process downward continues with the wavefield and defines the reflectivity as its values at the imaging time $t = 0$ (Loewenthal *et al.* [64]). The end result of the migration, however, is not true reflectivity but a combined value of true reflectivity and the incident wavefield at the location of each reflector (Wenzel [107]). By analogy, the Rocca *et al.* approach accounts for the spreading factor of only the backscattered wavefield. As learned in the course of this research, the spreading factor of the incident wavefield also can be included through the new formulation in this thesis.

4.2 Review of Born Inversion Application

Born inversion is a wave equation inversion procedure through a Born (first) approximation (Born [12]). To illustrate the Born inversion approach, a seismic velocity inversion example is to be described in this section. The acoustic wave propagating into the Earth's subsurface is discussed below.

Vector variables are denoted by bold type and the domain of Fourier transform is denoted by the corresponding argument.

The equation governing simple wave propagation for a point source in an inhomogeneous medium is

$$\left(\nabla^2 - \frac{1}{v^2(\mathbf{r})} \frac{\partial^2}{\partial t^2} \right) U(\mathbf{r}, \mathbf{r}_0; t) = \delta(\mathbf{r} - \mathbf{r}_0) \delta(t) \quad (4.1)$$

where $U(\mathbf{r}, \mathbf{r}_0; t)$ is a total wavefield, $v(\mathbf{r})$ is the local acoustic velocity, \mathbf{r}_0 and \mathbf{r} are respectively the source and observation positions, and $\delta(\cdot)$ is a Dirac delta function. If the subsurface velocity variation is small compared with a reference velocity, the velocity $v(\mathbf{r})$ can be defined by a perturbation equation such as

$$\frac{1}{v^2(\mathbf{r})} = \frac{1}{v_0} (1 + \alpha(\mathbf{r})) \quad (4.2)$$

where v_0 is the reference velocity and $\alpha(\mathbf{r})$ is a perturbation expressed in terms of index of refraction. Substituting Eq.(4.2) into (4.1) and performing a temporal Fourier transformation, we have the Helmholtz equation given by

$$\left(\nabla^2 + \frac{\omega^2}{v_0^2} (1 + \alpha(\mathbf{r})) \right) U(\mathbf{r}, \mathbf{r}_0; \omega) = \delta(\mathbf{r} - \mathbf{r}_0) \quad (4.3)$$

or

$$\left(\nabla^2 + \frac{\omega^2}{v_0^2} \right) U(\mathbf{r}, \mathbf{r}_0; \omega) = \delta(\mathbf{r} - \mathbf{r}_0) - \alpha(\mathbf{r}) \frac{\omega^2}{v_0^2} U(\mathbf{r}, \mathbf{r}_0; \omega) \quad (4.4)$$

where

$$U(\mathbf{r}, \mathbf{r}_0; \omega) = \int U(\mathbf{r}, \mathbf{r}_0, t) e^{-i\omega t} dt .$$

The right-hand side of Eq.(4.4) is composed of two source terms, consequently the integral representation of the solution is given by

$$\begin{aligned} U(\mathbf{r}, \mathbf{r}_0; \omega) &= U_0(\mathbf{r}, \mathbf{r}_0; \omega) + \int U_0(\mathbf{r}, \mathbf{r}'; \omega) \frac{\omega^2}{v_0^2} \alpha(\mathbf{r}') U(\mathbf{r}', \mathbf{r}_0; \omega) d\mathbf{r}' \\ &\equiv U_0(\mathbf{r}, \mathbf{r}_0; \omega) + U_S(\mathbf{r}, \mathbf{r}_0; \omega) \end{aligned} \quad (4.5)$$

where $U_0(\mathbf{r}, \mathbf{r}_0; \omega)$ satisfies

$$\left(\nabla^2 + \frac{\omega^2}{v_0^2} \right) U_0(\mathbf{r}, \mathbf{r}_0; \omega) = \delta(\mathbf{r} - \mathbf{r}_0) . \quad (4.6)$$

Thus $U_0(\mathbf{r}, \mathbf{r}_0; \omega)$ represents a spherical wavefield propagating from \mathbf{r}_0 to \mathbf{r} and can be defined by the Green's function for a homogeneous medium. The integral representation in Eq.(4.5) is known as the *Lippmann-Schwinger* integral equation (Weglein [106]).

The Lippmann-Schwinger integral equation is interpreted as indicating that the total field U is sum of the incident wavefield in the reference medium, U_0 , and the scattered wavefield, U_S . It is nonlinear because the unknown $U(\mathbf{r}, \mathbf{r}_0; \omega)$ is also a part of integrand. When the integral equation is successively iterated, the expansion of $U(\mathbf{r}, \mathbf{r}_0; \omega)$ in infinite series representation becomes

$$\begin{aligned} U &= U_0 + \int U_0(\mathbf{r}, \mathbf{r}'; \omega) \frac{\omega^2}{v_0^2} \alpha(\mathbf{r}') U_0(\mathbf{r}', \mathbf{r}_0; \omega) d\mathbf{r}' \\ &\quad + \int U_0(\mathbf{r}, \mathbf{r}'; \omega) \frac{\omega^2}{v_0^2} \alpha(\mathbf{r}') \cdot \end{aligned} \quad (4.7)$$

$$\begin{aligned}
& \left\{ \int U_0(\mathbf{r}', \mathbf{r}''; \omega) \frac{\omega^2}{v_0^2} \alpha(\mathbf{r}'') U_0(\mathbf{r}'', \mathbf{r}_0; \omega) d\mathbf{r}'' \right\} d\mathbf{r}' + \dots \\
& = U_0 + \underbrace{U_1 + U_2 + \dots}_{U_S} .
\end{aligned}$$

The second term U_1 is the sum of spherical waves originating at the source location, \mathbf{r}_0 , and propagating freely with reference velocity v_0 , being scattered at the first perturbation boundary \mathbf{r}' with a strength $(\omega^2/v_0^2)\alpha(\mathbf{r}')$ and then propagating freely again with speed v_0 to the observation position, \mathbf{r} . In general, U_n can be interpreted as a wave originating at \mathbf{r}_0 , experiencing n -scattering interactions and then being recorded by a certain receiver at \mathbf{r} .

An approximate linear equation is obtained by truncating the series in Eq.(4.7) after the second term, that is

$$U(\mathbf{r}, \mathbf{r}_0; \omega) \simeq U_0(\mathbf{r}, \mathbf{r}_0; \omega) + \int U_0(\mathbf{r}, \mathbf{r}'; \omega) \frac{\omega^2}{v_0^2} \alpha(\mathbf{r}') U_0(\mathbf{r}', \mathbf{r}_0; \omega) d\mathbf{r}' \quad (4.8)$$

or

$$U_S(\mathbf{r}, \mathbf{r}_0; \omega) \simeq \int U_0(\mathbf{r}, \mathbf{r}'; \omega) \frac{\omega^2}{v_0^2} \alpha(\mathbf{r}') U_0(\mathbf{r}', \mathbf{r}_0; \omega) d\mathbf{r}' . \quad (4.9)$$

This is known as Born (first) approximation because V.M. Born [12] initially introduced this approximation to scattering problems in atomic physics. This approximation has been utilized in many applications in physics, such as, atomic, nuclear, acoustic, and optic scattering problems.

The problem in this example is estimation of the subsurface velocity perturbation, $\alpha(\mathbf{r}')$, from measurements $U_S(\mathbf{r}, \mathbf{r}_0; \omega)$. For a far-field case (*i.e.* $|\mathbf{r}| \gg |\mathbf{r}'|_{max}$), the Green's function satisfying Eq.(4.6) is

$$U_0(\mathbf{r}, \mathbf{r}', ; \omega) = \frac{\exp \{-i(\omega/v_0)|\mathbf{r} - \mathbf{r}'|\}}{4\pi |\mathbf{r} - \mathbf{r}'|} \quad (4.10)$$

$$\simeq \frac{\exp(-ikr)}{4\pi r} \exp(i\mathbf{k}' \cdot \mathbf{r}') \quad (4.11)$$

where

$$\mathbf{k}' \equiv k \hat{r} \quad \text{and} \quad k = \omega/v_0$$

and where \hat{r} is a unit vector pointing from a scatterer to the observation position, and k is the wavenumber (Bleistein [10]). When Eq.(4.11) is substituted into Eq.(4.9), the scattered field in the far-field region becomes

$$U_S(\mathbf{r}, \mathbf{r}_0; \omega) \simeq \frac{\exp(-ikr)}{4\pi r} \int \exp(i\mathbf{k}' \cdot \mathbf{r}') k^2 \alpha(\mathbf{r}') \exp(-i\mathbf{k} \cdot \mathbf{r}') d\mathbf{r}' \quad (4.12)$$

where \mathbf{k} is the incident wave vector directed from the source position to a scatterer. Thus the amplitude of the scattered field is

$$T(\mathbf{k}, \mathbf{k}') = \int \exp(i\mathbf{k}' \cdot \mathbf{r}') k^2 \alpha(\mathbf{r}') \exp(-i\mathbf{k} \cdot \mathbf{r}') d\mathbf{r}' \quad (4.13)$$

If the observation point coincides with the source location, the observation direction \mathbf{k}' is opposite to the direction of the incident wave vector \mathbf{k} (i.e. $\mathbf{k}' = -\mathbf{k}$). Then Eq.(4.13) becomes

$$T(\mathbf{k}, -\mathbf{k}) = \int \exp(-2i\mathbf{k} \cdot \mathbf{r}') k^2 \alpha(\mathbf{r}') d\mathbf{r}' \quad (4.14)$$

and a Fourier transform relationship gives

$$\alpha(\mathbf{r}') = \frac{2}{(2\pi)^3} \int T(\mathbf{k}, -\mathbf{k}) \frac{\exp(2i\mathbf{k} \cdot \mathbf{r}')}{k^2} d\mathbf{k} \quad (4.15)$$

(Weglein [106]).

Eq.(4.15) thus allows the acoustic velocity configuration to be determined within the Born (first) approximation from backscattering information.

4.3 Forward Formulation for SAR Configuration

The previous section dealt with how the Born inversion can be applied to reflection seismology problems. In the derivation, the Born (first) approximation used in Eq.(4.9) had two implicit assumptions: (a) the incident wavefield remains unaffected, and (b) only the incident wavefield interacts with the velocity perturbation.

The first condition is required to formulate the Born inversion because the incident wave is assumed to be governed by a Green's function for the constant reference medium in Eq.(4.10). Thus the transmission losses or refractive effects on the incident wave as it propagates downward are not included.

The second assumption is in fact the main step of the Born (first) approximation to omit higher-order scattering caused by other than the incident wave.

SAR specific features must be investigated to develop an inversion method of SAR data using the Born (first) approximation. Differences between SAR configuration and reflection seismology are summarized as follows:

- 1) unlike in seismic applications, the reference velocity is a constant, i.e. the velocity of light,
- 2) the center frequency of the radar signal is much higher than that of seismic waves,
- 3) the source and receiver pairs are not on the scattering surface, and

4) there is relative motion of antenna with respect to scatterers.

The first point is favorable to the application of Born inversion to the SAR processing method. In addition, the incident wavefield remains unaffected until it arrives at scatterers on the scattering surface, while the seismic incident wave is affected by energy loss due to transmission, refraction and etc., as it propagates through the Earth.

The high frequency nature of the SAR transmitted signal will also be exploited to derive an approximation for the high-frequency backscattered wavefield.

SAR processing scheme also must take into account the last two points, whereas no particular attention is normally required in seismic problems. For SAR there is a relatively large time gap between the transmission time and the first return signal arriving time because of the large distance between the antenna and the scattering surface. This time gap must be considered in proper reconstruction of the SAR image data. In SAR a problem also arises from fluctuations in the relative velocity of the moving antenna with respect to the scatterers. A constant velocity results in equally spaced sampling interval in the azimuth dimension. However, the relative velocity of the SAR antenna often varies along the flight path, and this results in a defocused image unless appropriate corrections are made.

Based on the above discussions, an approximate relationship representing the high-frequency backscattered wavefield, which corresponds to the SAR received signals, can be formulated as follow.

The Helmholtz equation in the frequency-domain is given by

$$\left(\nabla^2 + \frac{\omega^2}{c^2}\right)U(\mathbf{r}, \mathbf{r}_o; \omega) = -f(\mathbf{r} - \mathbf{r}_o) \quad (4.16)$$

where

$$U(\mathbf{r}, \mathbf{r}_o; \omega) = \int_{-\infty}^{\infty} U(\mathbf{r}, \mathbf{r}_o; t) e^{-i\omega t} dt$$

and where $U(\mathbf{r}, \mathbf{r}_o; \omega)$ is the total electromagnetic wavefield, $f(\mathbf{r} - \mathbf{r}_o)$ is the source, c is the velocity of light, and \mathbf{r}_o is the source coordinate. The first argument of $U(\mathbf{r}, \mathbf{r}_o; \omega)$ represents the receiver location, and the second is the source location. Compared with Eq.(4.4), the subsurface velocity perturbation $\alpha(\mathbf{r})$ is now not necessary to be included in the SAR case. The source function $f(\mathbf{r} - \mathbf{r}_o)$ of a SAR system is a point source with respect to the azimuth dimension. But this source function is a time-dependent function in the range dimension because the transmitted signal is linearly frequency-modulated. The source function in the range dimension is a simple convolution of a delta function with a frequency modulation function, and consequently the temporal term does not play an important role after the range compression. The range compression is straightforward, and is not main interest of the discussion in this section. Our analysis can continue with the assumption that the range compression has already been completed.

The total wavefield $U(\mathbf{r}, \mathbf{r}_o; \omega)$ can be decomposed into the incident wavefield U_I generated by the source, and the scattered wavefield U_S due to scattering on the surface. Thus $U(\mathbf{r}, \mathbf{r}_o; \omega)$ can be rewritten as

$$U(\mathbf{r}, \mathbf{r}_o; \omega) = U_I(\mathbf{r}, \mathbf{r}_o; \omega) + U_S(\mathbf{r}, \mathbf{r}_o; \omega) \quad (4.17)$$

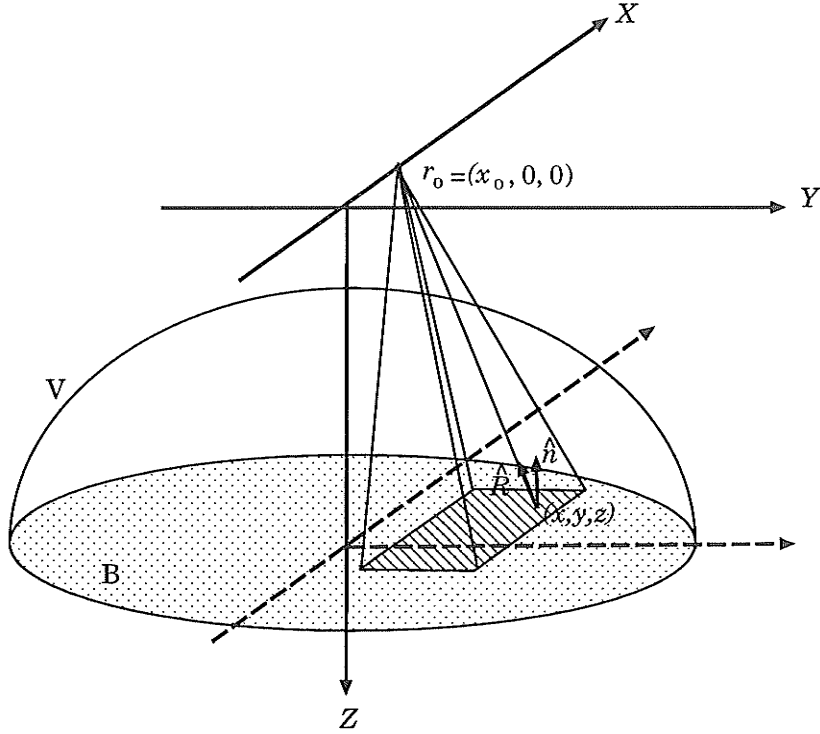


Figure 4.1: Schematic diagram of the SAR geometry and integration volume of Green's integral

Integrating Eq.(4.16) over volume V given in Figure 4.1 and replacing the total wavefield by Eq.(4.17), we have, from Green's theorem,

$$U_S(\mathbf{r}_0, \mathbf{r}_0; \omega) = \iint_B \left[U_S(\mathbf{r}, \mathbf{r}_0; \omega) \frac{\partial}{\partial n} G_0(\mathbf{r}, \mathbf{r}_0; \omega) - G_0(\mathbf{r}, \mathbf{r}_0; \omega) \frac{\partial}{\partial n} U_S(\mathbf{r}, \mathbf{r}_0; \omega) \right] d^2\mathbf{r} \quad (4.18)$$

where B represents the surface boundary and \mathbf{n} is the unit vector normal to the boundary surface as shown in Figure 4.1.

The receiving location of the antenna (\mathbf{r}) was replaced by the transmitting

location of the antenna (\mathbf{r}_o) in the derivation. Similar to Eq.(4.10), the Green's function $G_0(\mathbf{r}, \mathbf{r}_o; \omega)$ for a homogeneous medium with the reference velocity c is given by

$$G_0(\mathbf{r}, \mathbf{r}_o; \omega) = \frac{\exp \{-i\omega |\mathbf{r} - \mathbf{r}_o| / c\}}{4\pi |\mathbf{r} - \mathbf{r}_o|} , \quad (4.19)$$

and this Green's function is identical to the incident wavefield $U_I(\mathbf{r}, \mathbf{r}_o; \omega)$ because U_I also satisfies Eq.(4.6).

To derive Eq.(4.18) from Eqs.(4.16) and (4.17), we have assumed that the receiver location is the same as the source location. This assumption is not strictly true in the SAR case because the SAR antenna moves constantly with time. The approximation, however, can be validated because the ratio of the distance traveled by the antenna between the signal transmission and the arrival of the first echo to the slant-range is extremely small.

If surface scattering is dominant, we can assume that the backscattered wavefield is linearly proportional to the incident wavefield in the vicinity of the surface boundary B such that

$$U_S(\mathbf{r}, \mathbf{r}_o; \omega) \sim \sigma^o(\mathbf{r}) U_I(\mathbf{r}, \mathbf{r}_o; \omega) \quad \mathbf{r} \text{ on } B \quad (4.20)$$

$$\frac{\partial}{\partial n} U_S(\mathbf{r}, \mathbf{r}_o; \omega) \sim -\sigma^o(\mathbf{r}) \frac{\partial}{\partial n} U_I(\mathbf{r}, \mathbf{r}_o; \omega) \quad \mathbf{r} \text{ on } B . \quad (4.21)$$

This approximation corresponds to the Kirchhoff boundary condition in optics (Goodman [35], Bleistein [10]). Volume scattering is not completely negligible in some media such as glacier ice or the vegetation canopy. Volume scattering depends upon the ability of the microwave transmitted by the SAR antenna to penetrate surface media and return signals from scatterers

below that surface. In general, surface scattering at terrain or ocean surface is, however, by far dominant relative to volume scattering in geological or oceanographic application of SAR.

The parameter $\sigma^o(\mathbf{r})$ represents the complex ratio of the backscattered wavefield to the incident wavefield at the surface boundary, and indicates a phase change as well as an amplitude ratio at the scattering surface. The complex backscattering coefficient $\sigma^o(\mathbf{r})$ may have geophysical significance. Terrain slope (or incident angle), surface roughness, and complex dielectric constant characterize properties of a scattering surface. Consequently, they are influences on radar return. The amplitude of the complex backscattering coefficient is governed mainly by terrain slope and surface roughness. The complex dielectric constant determines penetration of microwave, and is closely related to the phase of the complex backscattering coefficient.

In fact, the above two approximations in Eqs.(4.20) and (4.21) imply that sources of the backscattered wavefield other than the most significant term, the incident wavefield, are neglected. That is exactly the same idea as Born (first) approximation in Eq.(4.9).

Substituting Eqs.(4.20), and (4.21) into (4.18), we have

$$U_S(\mathbf{r}_o, \mathbf{r}_o; \omega) \sim 2 \iint_B \sigma_n^o(\mathbf{r}) G_0(\mathbf{r}, \mathbf{r}_o; \omega) \frac{\partial}{\partial n} G_0(\mathbf{r}, \mathbf{r}_o; \omega) d^2\mathbf{r} \quad (4.22)$$

if the incident wavefield U_I is replaced by Green's function $G_0(\mathbf{r}, \mathbf{r}_o; \omega)$. For the Green's function in Eq.(4.19), we have an approximation to a leading order term in ω given by

$$U_S(\mathbf{r}_o, \mathbf{r}_o; \omega) \sim \frac{i\omega}{8\pi^2 c} \iint_B \sigma_n^o(\mathbf{r}) \frac{e^{-i2\omega R/c}}{R^2} d^2\mathbf{r} + O\left(\frac{c}{\omega R}\right) \quad (4.23)$$

$$= 2\frac{i\omega}{c} \iint_B \sigma_n^o(\mathbf{r}) G_0^2(\mathbf{r}, \mathbf{r}_0; \omega) d^2\mathbf{r} \quad (4.24)$$

where $O(\cdot)$ is the order of the approximation error and

$$\sigma_n^o(\mathbf{r}) = \sigma^o(\mathbf{r}) \hat{\mathbf{n}} \cdot \hat{\mathbf{R}} \quad , \quad (4.25)$$

$$R(x, y, z; x_0, y_0, z_0) = \sqrt{(x - x_0)^2 + (y - y_0)^2 + (z - z_0)^2} \quad (4.26)$$

where $\hat{\mathbf{R}}$ is the unit vector from a scatterer to the source. This approximation is valid when the frequency is high enough and R is large enough to satisfy $c/\omega R \ll 1$. In the SAR case, the value $c/\omega R$ has at most an order of 10^{-3} .

Eq.(4.23) indicates that the backscattered wavefield can be expressed using an integral over all possible scatterers on the ground. The integrand is the product of the complex backscattering coefficient $\sigma_n^o(\mathbf{r})$, the wave propagation term $\exp\{-i2\omega R/c\}/R^2$, and the linear frequency-dependent term $i\omega/(8\pi^2 c)$.

The SAR antenna receives the backscattered wavefield U_S , and therefore the forward formula Eq.(4.23) corresponds to the range-compressed SAR signal which has been described in many publications (for instance, van de Lindt 1977, Eq.(1.23)). But the expression U_S in Eq.(4.23) differs from the conventional description of the SAR signal in that $1/R^2$ term is explicitly included in the integration. This inverse square of the distance term is inherited from the theory of wavefield propagation, and corresponds to the *spreading factor* in the radar equation (Ulaby *et al.* [103]).

4.4 The Inversion

The equation Eq.(4.23), derived in the previous section, indicates that the inverse scattering problem associated with the SAR theory reduces to a problem of estimating the complex backscattering coefficient $\sigma_n^o(\mathbf{r})$ from the backscattered wavefield $U_S(x_0, y_0, z_0; \omega)$ as observed along the line $y_0 = z_0 = 0$. Inversion of Eq.(4.23) can utilize a spatial Fourier transformation to derive a simple relation between the observed data and the backscattering coefficient in the f - k domain.

As mentioned in the previous section, the forward formula, Eq.(4.23), is similar to the conventional expression of the range-compressed SAR signal except for the spreading factor $1/R^2$ term. Most conventional SAR processors use $\exp\{-i2\omega R/c\}$ as the azimuth impulse-response function. It has been known that it is difficult to find an explicit Fourier transform formula for this function.

If, however, only a $1/R$ term is included, it becomes to obtain an explicit Fourier transform relationship with respect to x_0 . The Fourier transform of the function $\exp\{-i2\omega R/c\}/R$ is a Hankel function of the second kind (Magnus and Oberhettinger [71], p.118). Moreover, the first-order asymptotic approximation of the Hankel function reduces the result to the kernel of the Fourier transform as shown by Eq.(A..3) in Appendix A. The integrand in Eq.(4.24), however, is a square of the Green's function. To overcome this problem, a modified function can be introduced in an analogous manner to the seismic Born inversion scheme (for instance, Eq.(10) of Bleistein

et al. [11]). To achieve this, we introduce a function $\Theta(x_0, 0, 0; \omega)$ defined by

$$\Theta(x_0, 0, 0; \omega) \equiv \omega \frac{\partial}{\partial \omega} \left(\frac{U_S(x_0, 0, 0; \omega)}{\omega} \right) . \quad (4.27)$$

When U_S in Eq.(4.23) is replaced by the new function $\Theta(x_0, 0, 0; \omega)$, we have

$$\Theta(x_0; \omega) \sim \frac{2\omega}{8\pi^2 c^2} \iint_B \sigma_n^o(\mathbf{r}) \frac{\exp\{-i2\omega R/c\}}{R} d^2\mathbf{r} . \quad (4.28)$$

An inversion formula can be described by slant-range coordinates instead of ground-range coordinates because the SAR signal data and the reconstructed image are primarily represented by slant-range coordinates. If we assume a flat surface, the height of antenna platform above the surface reduces to a constant value z_0 . If we take the Fourier transform of $\Theta(x_0; \omega)$ in Eq.(4.28) with respect to x_0 and change the coordinate (y, z_0) using a slant-range at the closest approach of the antenna, $\eta = \sqrt{y^2 + z_0^2}$, we have

$$\Theta(k_x; \omega) \sim \frac{i\omega e^{i\pi/4}}{4\pi c^2} \sqrt{\frac{2}{\pi k_\eta}} \iint_B \sigma_{nc}^o(x, \eta) e^{-i(k_x x + k_\eta \eta)} dx d\eta \quad (4.29)$$

where

$$\begin{aligned} \Theta(k_x; \omega) &= \int_{-\infty}^{\infty} \Theta(x_0; \omega) e^{-ik_x x_0} dx_0 , \\ \sigma_{nc}^o(x, \eta) &= \sqrt{\frac{\eta}{\eta^2 - z_0^2}} \sigma_n^o(x, \eta) , \\ -2\pi \frac{\text{PRF}}{2V_s} &\leq k_x \leq 2\pi \frac{\text{PRF}}{2V_s} , \end{aligned} \quad (4.30)$$

and

$$k_\eta = \sqrt{4\frac{\omega^2}{c^2} - k_x^2} , \quad 4\frac{\omega^2}{c^2} \geq k_x^2 \quad (4.31)$$

where V_s is a platform velocity and PRF is pulse repetition rate.

Detailed derivation of Eq.(4.29) from Eq.(4.28) is given in Appendix A. The value of $2\omega/c$ is much larger than k_x in SAR systems because the center frequency of the transmitted pulse is on the order of $\sim 10^9 Hz$. Therefore, k_η in Eq.(4.31) can only be expressed in positive values.

The right-hand side of Eq.(4.29) is a two-dimensional Fourier transform, and therefore the inversion formula can easily be derived from Eq.(4.29) using the two-dimensional inverse Fourier transform formula. The resulting inversion formula then becomes

$$\sigma_{nc}^o(x, \eta') \sim -4\sqrt{2\pi^3} c e^{i\pi/4} \frac{1}{(2\pi)^2} \iint \frac{\sqrt{k_\eta}}{\sqrt{k_\eta^2 + k_x^2}} e^{i\eta_0(k_\eta - \sqrt{k_\eta^2 + k_x^2})} \Theta\left(k_x; \frac{c}{2}\sqrt{k_\eta^2 + k_x^2}\right) e^{i(k_x x + k_\eta \eta')} dk_x dk_\eta \quad (4.32)$$

where

$$\eta' = \eta - \eta_0 \quad (4.33)$$

and where η_0 is the minimum slant-range. Derivation of Eq.(4.32) from Eq.(4.29) is given in Appendix B.

The above inversion procedure may be summarized as follows. The SAR data inversion is a process of estimating the complex backscattering coefficient $\sigma_n^o(x, \eta)$ from the backscattered wavefield, *i.e.* the received SAR signals, observed along the platform flight line. This goal can be achieved by a series of processing steps;

- 1) forward two-dimensional Fourier transform,
- 2) frequency-domain interpolation for the change of variable from ω to k_η ,

- 3) phase shift and amplitude adjustment (in Eq.(4.32)) to the function $\Theta(k_x; \omega)$ which is a derivative of the two-dimensional Fourier transform of the raw SAR data, and
- 4) then two-dimensional Fourier inverse transformation.

The differentiation with respect to the frequency in Eq.(4.27) is more easily done by simply multiplying $(-it)$ in the time domain before Fourier transformation.

A further approximation can be made for comparison of Eq.(4.32) with conventional range-Doppler approaches. When the variable k_η is replaced by $\omega = (c/2)\sqrt{k_x^2 + k_\eta^2}$, the inversion formula reduces to

$$\sigma_{nc}^o(x, \eta') \sim A \iint \left[\left(\frac{\omega}{c/2} \right)^2 - k_x^2 \right]^{-1/4} \Theta(k_x; \omega) e^{+i(xk_x + 2\eta'\omega/c)} \exp \left\{ i\eta \left[\sqrt{\left(\frac{\omega}{c/2} \right)^2 - k_x^2} - \frac{\omega}{c/2} \right] \right\} dk_x d\omega \quad (4.34)$$

where $A = -8\sqrt{2\pi^3}e^{i\pi/4}/(2\pi)^2$.

The following inequality condition holds for most SAR systems

$$\left(\frac{\omega_0 + \omega'}{c/2} \right)^2 \gg k_x^2 \quad (4.35)$$

where $\omega = \omega_0 + \omega'$, ω_0 is the carrier frequency, and ω' is the frequency within the bandwidth. Then above equation can be further approximated to be

$$\sigma_{nc}^o(x, \eta') \sim A \iint \sqrt{\frac{c}{2\omega_0}} \Theta(k_x; \omega) e^{+i(xk_x + 2\eta'\omega/c)} \exp \left\{ -i\eta \frac{c}{4} \frac{k_x^2}{\omega_0 + \omega'} \right\} dk_x d\omega \quad (4.36)$$

The Eq.(4.36) cannot be used directly for the f - k domain processing because the transfer function $\exp\{-i\eta ck_x^2/4(\omega_0 + \omega')\}$ is range dependent. The range dependence of the transfer function has been overcome through the change of variable from ω to k_η in the formulation of Eq.(4.32).

A comparison between the approach in this thesis and conventional approaches can be made using Eq.(4.36). The comparison was detailed in section 3.2.3.

4.5 Further Focusing

One of problems in the inversion method arises from the irregularity of platform velocity, more precisely from the irregular azimuth sampling distance. The inversion method in this thesis was derived and developed under the assumption of a constant sampling distance in the azimuth dimension. However, this assumption is not always true for many of the acquired SAR data sets. The azimuth sampling distance varies in the azimuth dimension due to the platform velocity changes.

The irregularity of the azimuth sampling distance causes errors in k_x values in the f - k domain, and thus results in image blurring. In the subarea of a image where a full focused resolution is not achieved due to the error in the azimuth sampling distance, further focusing becomes necessary.

The inversion approach utilizes a phase adjustment in the f - k domain. In Eq.(4.34), the phase adjustment of the inversion method in the f - k domain approximates to a function such as

$$\exp\left\{\frac{-ic\eta_0 k_x^2}{4\omega_0}\right\} \simeq \exp\left\{-i\frac{\lambda k_x^2}{4}\right\} \quad (4.37)$$

The azimuth wavenumber k_x is governed by the azimuth sampling distance Δx . If the value of Δx used for the inversion processing is different from the true azimuth sampling distance $\Delta x'$, it will result in incorrect phase adjustment. The phase error due to the incorrect value of Δx can be further focused by adjusting the phase difference given by

$$\exp\left\{-i\frac{\lambda k_x'^2}{4}\left(\pm\sqrt{dk_x'^2 - dk_x^2}\right)\right\} \quad (4.38)$$

where k'_x is a wavenumber corresponds to the correct azimuth sampling distance $\Delta x'$ and the \pm sign complies to the sign of the value of inside square root. Thus the additional focusing requires precise estimation of the value of $\Delta x'$ for the subarea where further focusing is necessary. One approach is to estimate velocity information from the SAR data, and a method developed by Moreira [83] is found to be very useful for this purpose.

Chapter 5

Numerical Algorithm and Image Formation

5.1 Algorithm Features

An inversion approach to SAR image reconstruction has been formulated theoretically in the earlier chapters. Inverse scattering and Born inversion theory was applied in the formulation. The proposed inversion and image formation of SAR data has been implemented numerically, and is summarized as a flow chart in Figure 5.1.

The inversion scheme shown in Figure 5.1 is based on Eq.(4.32). After Fourier transform of the raw SAR data, differentiation with respect to frequency is required to obtain $\Theta(x_0; \omega)$ from $U_S(x_0; \omega)$ as in Eq.(4.27). The same result, however, can be more easily achieved by multiplying raw SAR data by $(-it)$ before Fourier transformation. The output of Fourier transformation is then not the Fourier transform $U_S(k_x; \omega)$ of the original raw SAR data but its derivative $\Theta(k_x; \omega)$ as shown at the fourth step in Figure 5.1.

The performance of the proposed SAR signal processing approach largely

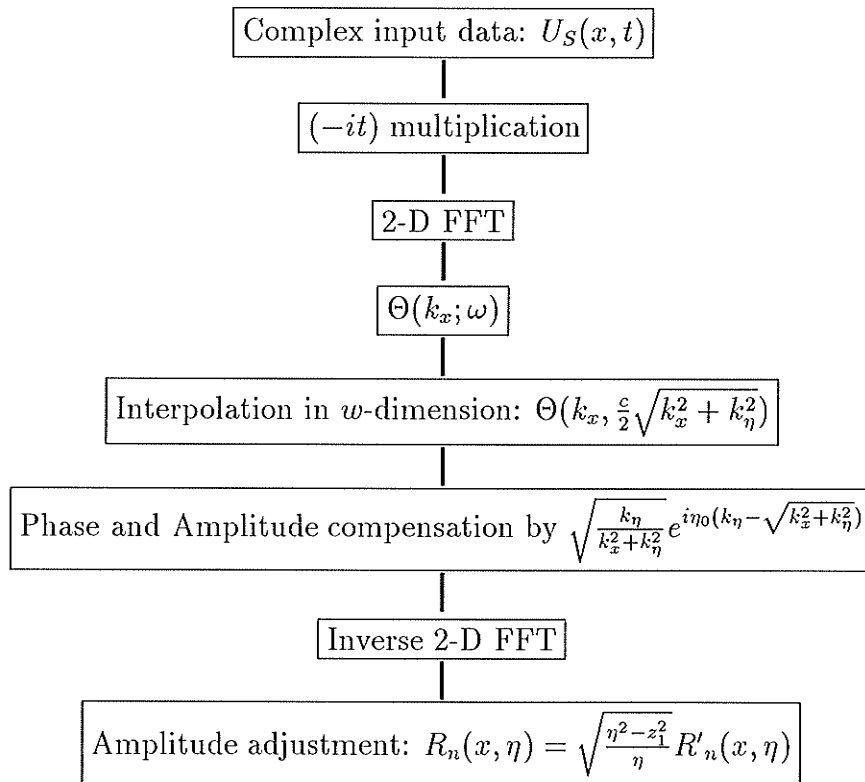


Figure 5.1: Flow chart for the proposed inversion of SAR data.

depends on the phase shift and frequency-domain interpolation steps. The interpolation is inherited from the change of the variable from frequency, ω , to slant-range wavenumber, k_r . This step is same as the Rocca *et al.* [96] approach, and has been known as *Stolt's change of variable method* in seismic processing (Stolt [99]). For SAR signal processing, the frequency-domain interpolation has posed difficulties because the frequency spectra of SAR signals are extremely oscillatory as shown in Figure 5.2 (a), and the interpolation points are unevenly spaced. Thus interpolation requires very high accuracy and has posed problems. The required accuracy can be achieved by employing an interpolation method developed by Rosenbaum and Bourdeaux [97]. A test result of the interpolation is given in Figure 5.2. The SAR signal frequency spectra in Figure 5.2 (a) consists of 512 samples and are generated with the 1.275 GHz center frequency, 19 MHz chirp bandwidth, 33.8 μ sec chirp width, and 45.8 MHz sampling frequency. Interpolation is carried out using all the midpoints of the original sampling points. The midpoint interpolation shifts the frequency spectra by one-half the sampling interval, Δf , and consequently the inverse Fourier transform of the interpolated frequency spectra results in phase shifts of the original SAR signal by $\Delta f/2$. Figure 5.2 (b) is obtained by multiplying the original input SAR signal by the $\Delta f/2$ phase shift term, and consequently it represents the theoretical output of a frequency-domain interpolation. Figure 5.2 (c) represents the signal obtained through an actual frequency-domain interpolation. The result of the frequency-domain interpolation reproduces both the real and imaginary parts of the theoretical output with high accuracy.

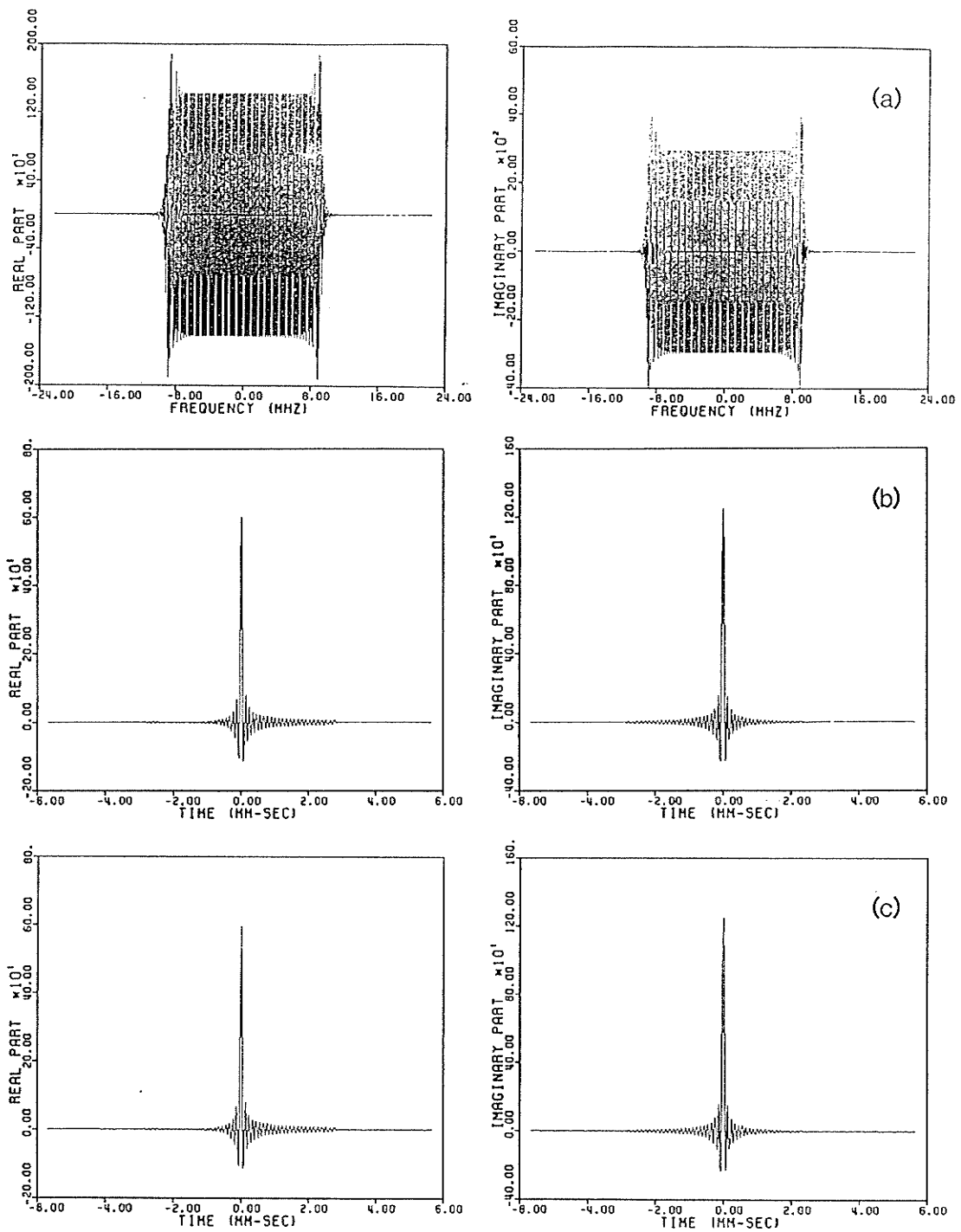


Figure 5.2: Examples from the frequency domain interpolation; (a) frequency spectra of SAR signal, (b) signal obtained by multiplying $\exp\{-it\Delta f/2\}$, and (c) signal obtained through a frequency domain interpolation.

Two-dimensional inverse FFT and amplitude adjustment steps then follow the phase shift step.

The computational efficiency of the SAR processing algorithm being proposed here can be compared with the conventional range-Doppler SAR processors (for example, Wu [109]). When input data of a N by N data array are to be processed using a conventional approach, the range correlation has to be performed first through FFT. Since each correlation of N data requires $N \log_2 N$ butterfly computations (BF) for forward and inverse FFT and N complex multiplications (CM), the total range correlations require $N \times \{(N \log_2 N) \cdot \text{BF} + N \cdot \text{CM}\}$ operations. The same number of operations are also required for the azimuth correlation, and consequently the range and azimuth correlation requires a total of $2 \times N \times \{(N \log_2 N) \cdot \text{BF} + N \cdot \text{CM}\}$ operations. The inversion algorithm being proposed in this thesis requires 2-D FFT and $N \times N$ complex multiplications, which add up to $N \times \{2 \times (N \log_2 N) \cdot \text{BF} + N \cdot \text{CM}\}$ operations. Thus the conventional correlation algorithm requires $N \times N$ more complex multiplications than the inverse algorithm for the range and azimuth compression.

5.2 Digital Simulation

Digital simulation and image formation are conducted to test the performance of the inversion method. To evaluate the capability of the inversion method properly, it is necessary to carry out the simulation on a spaceborne SAR system as well as on an airborne SAR system (Won and Moon [108]).

First the simulated airborne or spaceborne SAR received signals were generated by using the key parameters of the CCRS's C-band airborne SAR system and the Seasat SAR system, respectively. The CCRS's C-band airborne SAR system was chosen for an airborne SAR simulation because a set of raw SAR data acquired by the CCRS's C-band airborne SAR system was also processed by the new inversion algorithm. The narrow swath mode, however, is simulated, while the actual SAR data set is acquired in the nadir mode. For the simulation of a spaceborne SAR system, the system parameters of the Seasat SAR are used. The system parameters of the CCRS narrow swath C-band SAR configuration are listed in Table 5.1, and the Seasat SAR system parameters in Table 2.1.

A single point scatterer model and the multiple point scatterer models are used for the simulation. A single point scatterer model is aimed at studying the azimuth compression performance. A point scatterer with unit backscattering coefficient is located at the center of the image in this model. The multiple point scatterer models are used to evaluate the capability of accommodating the range curvature and of reconstructing phase information. Scatterers are assumed to have complex backscattering coefficients in

Table 5.1: Specifications of CCRS's C/X-band airborne SAR (Livingstone *et al.* [62]).

	C-Band		X-Band	
Transmitter				
Nominal Altitude	6 km		6 km	
Frequency	5.30 GHz		9.25 GHz	
Wavelength	5.66 cm		3.24 cm	
PRF/V (Swath Mode)	2.32 or 2.57 Hz/m/s (Narrow)	2.57 Hz/m/s (Wide)	2.32 or 2.57 Hz/m/s (Narrow)	2.57 Hz/m/s (Wide)
Chirp length	7 μ s	8 μ s	15 μ s	30 μ s
Receiver	(Narrow)	(Wide)	(Narrow)	(Wide)
Compressed pulse width	40 ns	120 ns	32 ns	134 ns
Noise figure	5.2 dB	3.7 dB	5.3 dB	5.2 dB
Antenna	(H-Pol.)	(V-Pol.)	(H-Pol.)	(V-Pol.)
Azimuth beamwidth	3.0°	4.2°	1.4°	1.4°
Elevation beamwidth	20°	29°	26°	26°
Peak gain	24 dB	22 dB	28dB	29 dB
Resolution	(Narrow)	(Wide)	(Narrow)	(Wide)
Azimuth	6 m	10 m	6 m	10 m
Range	6 m	20 m	6 m	20 m

Table 5.2: Model parameters for digital simulations.

	Scatterer location ^a (Range,Azimuth)	Scatterer values		Reconstructed Phase
		Amplitude	Phase	
Airborne	(513,513)	1.0	0.0°	-
Seasat	(513,2049)	1.0	0.0°	-
	(1025,2049)	1.0	0.0°	-
	(1537,2049)	1.0	0.0°	-
	(2049,2049)	1.0	0.0°	-
	(2561,2049)	1.0	0.0°	-
	(3073,2049)	1.0	0.0°	-
	(3585,2049)	1.0	0.0°	-
	(1025,1025)	1.00	90.0°	88.2°
	(3073,1025)	0.75	45.0°	44.5°
	(3073,3073)	0.50	30.0°	29.3°

^acoordinate in pixel numbers

the multiple point scatterer model. The model parameters are listed in Table 5.2. The simulated SAR signal are generated through a two-dimensional convolution for each model as described by Wu *et al.* [112]. The digital simulation for the airborne SAR system is carried out with a 1024×1024 input data array, which covers about 4 km in slant range and 400 m in azimuth. Generally the larger azimuth length is included in the simulation, the more extended frequency spectra in the $f-k$ domain are obtained (Won and Moon [108]). A simulated SAR signal after the range compression is shown in Figure 5.3 (a). A cosine square function is used as weighting function in azimuth.

The reconstructed amplitude image is given in Figure 5.3 (b). The input

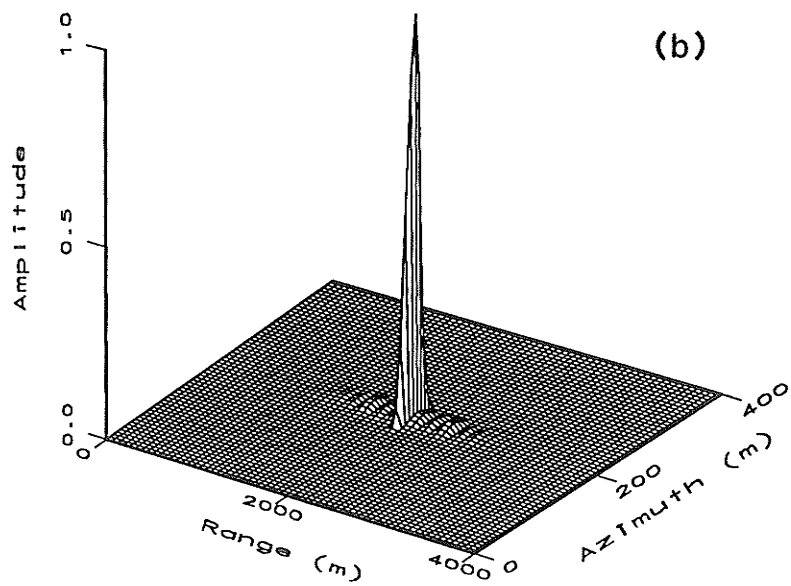
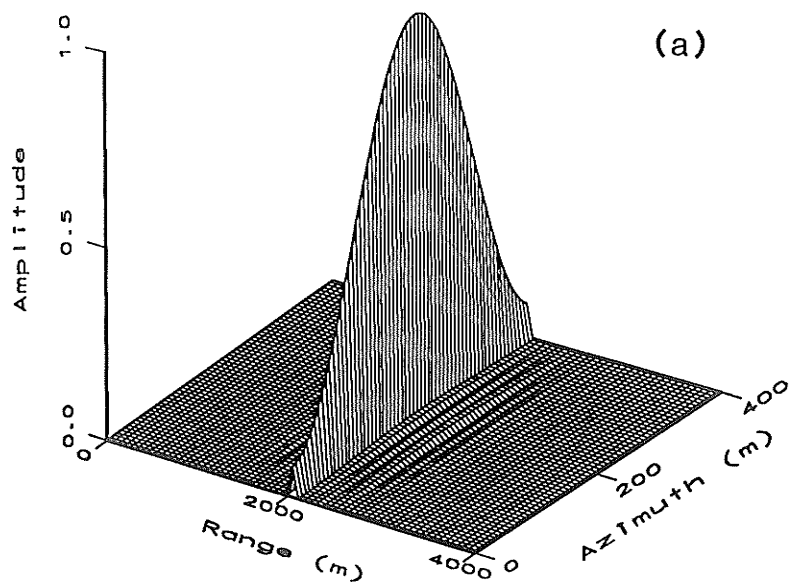


Figure 5.3: Airborne simulation: (a) a simulated input signal of 1024×1024 pixels, and (b) the reconstructed amplitude image after inversion processing alone. The range and azimuth sampling intervals are 4 m and 0.39 m , respectively.

signal and the reconstructed three dimensional image in Figure 5.3 (a) and (b) are exaggerated by ten times in azimuth because the sampling intervals in azimuth and range are respectively 0.39 m and 4.0 m . The amplitudes of the reconstructed image, shown in Figure 5.3 (b), are relative amplitudes. Pixels around the reconstructed point scatterer are selected from the image to produce a close-look power image given in Figure 5.4. After subsampling around the point scatterer, interpolation is carried out. The power of pixels less than -20 dB was replaced by -20 dB in Figure 5.4 (a). A cross section along the azimuth line crossing the center of the scatterer is shown in Figure 5.4 (b). The 3 dB width in azimuth of the reconstructed point scatterer is approximately 2.8 m .

The Seasat SAR simulations are conducted with 4096×4096 input data array, which covers an area of about 27 km by 19 km in range and azimuth, respectively. The pulse repetition frequency is 1645 Hz , and the sampling frequency of range pixels is 22.76 Hz . The range and azimuth sampling intervals are 6.6 m and 4.5 m , respectively.

The first model of Seasat simulation consists of seven point scatterers aligned along the center range line of the image (Table 5.2). The image of the input signal after range compression is shown in Figure 5.5 (a). The range curvature of the nearest scatterer is extended up to approximately 63 m in slant range which corresponds to 10 range pixels. The output image after the inversion processing is shown in Figure 5.5 (b), which displays only 256 range lines around the center. Thus the image in Figure 5.5 (b) represents about 1.2 km in azimuth and 27 km in slant range. This simulation demonstrates

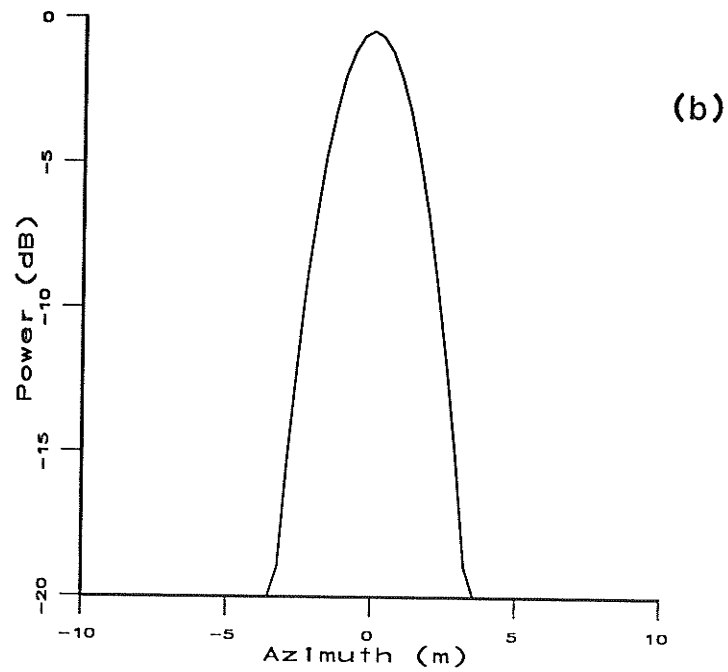
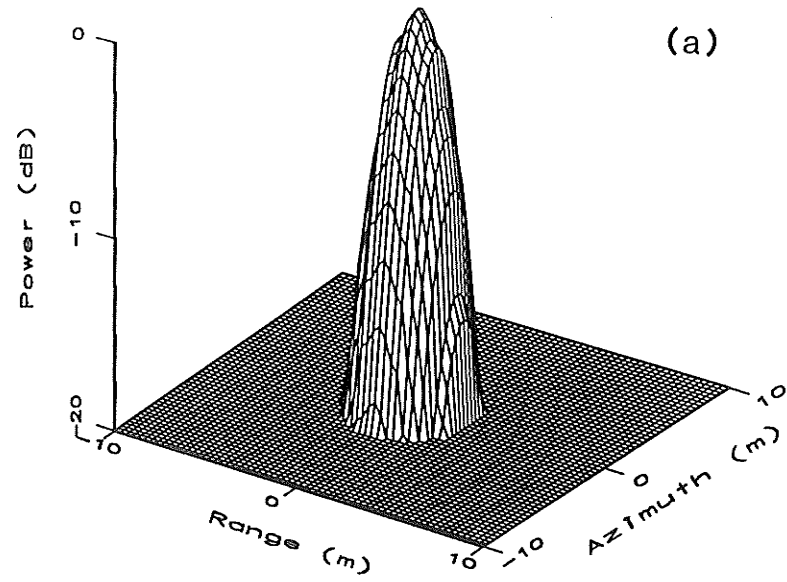
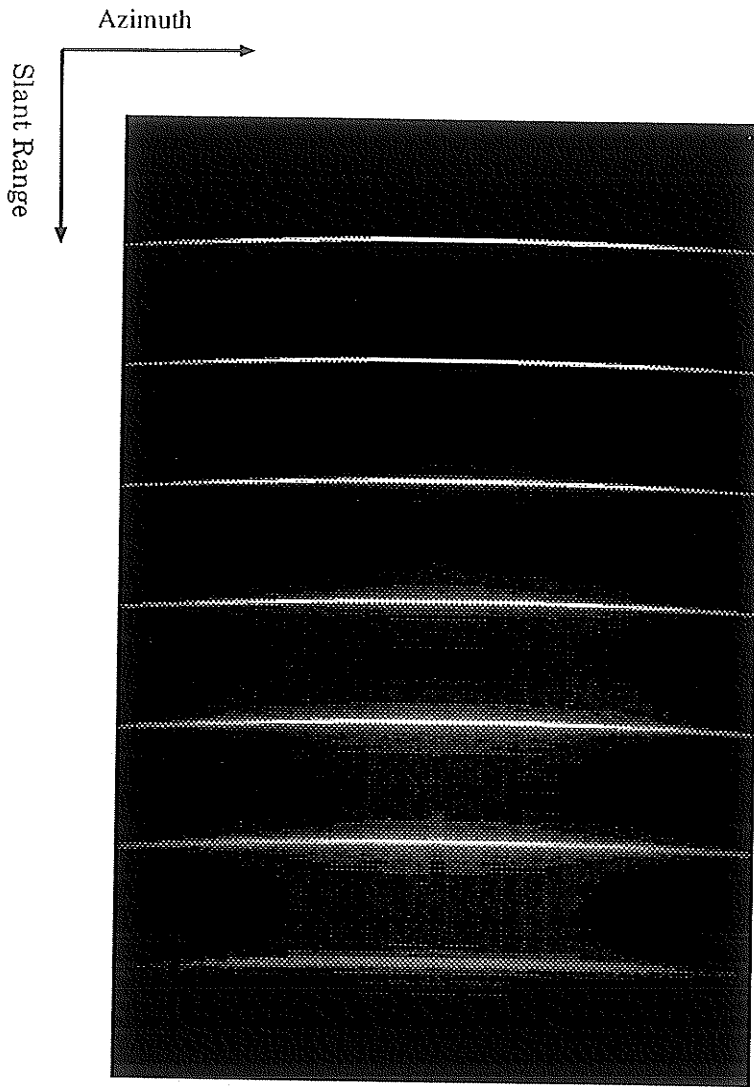
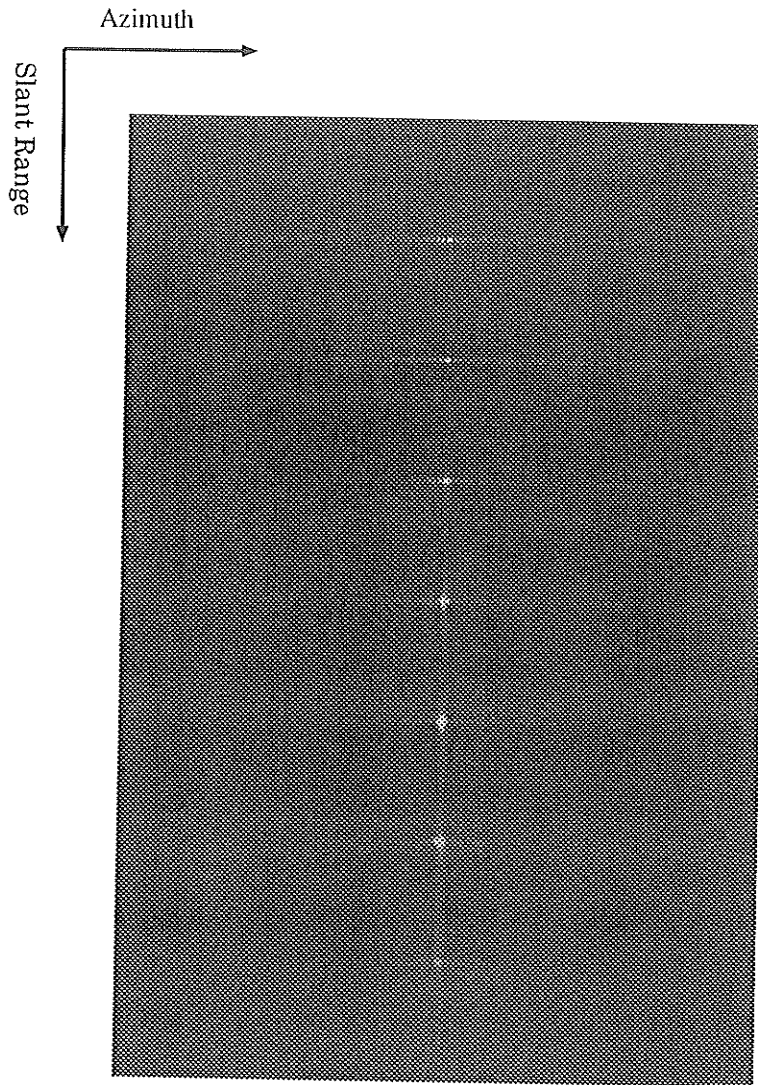


Figure 5.4: (a) Power representation of the reconstructed point scatterer, and (b) cross section along the center azimuth line of the point scatterer. The 3 dB width in azimuth is about 2.8 *m*.



(a)

(continued to the next page)



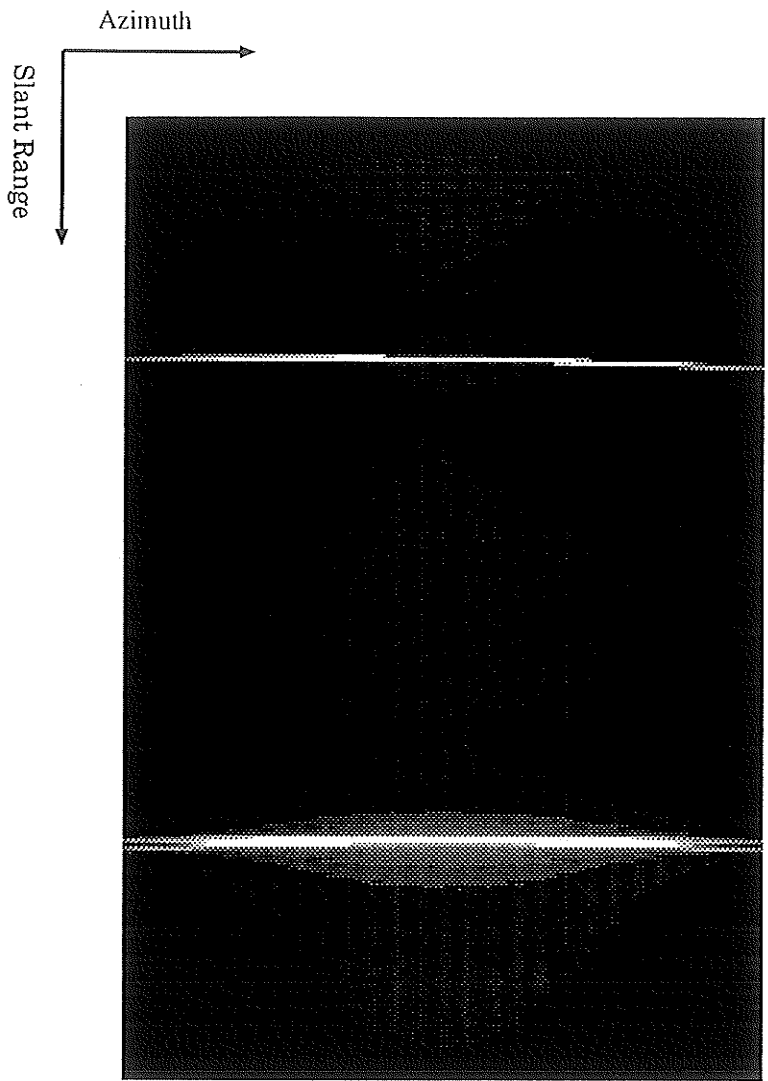
(b)

Figure 5.5: Seasat simulation with seven point scatterers aligned along a range line: (a) a simulated input signal of 4096×4096 pixels, (b) the reconstructed subimage of 4096×256 (range \times azimuth) pixels. Range and azimuth sampling interval are respectively 6.6 m and 4.5 m .

that the inversion method can accommodate the range curvature.

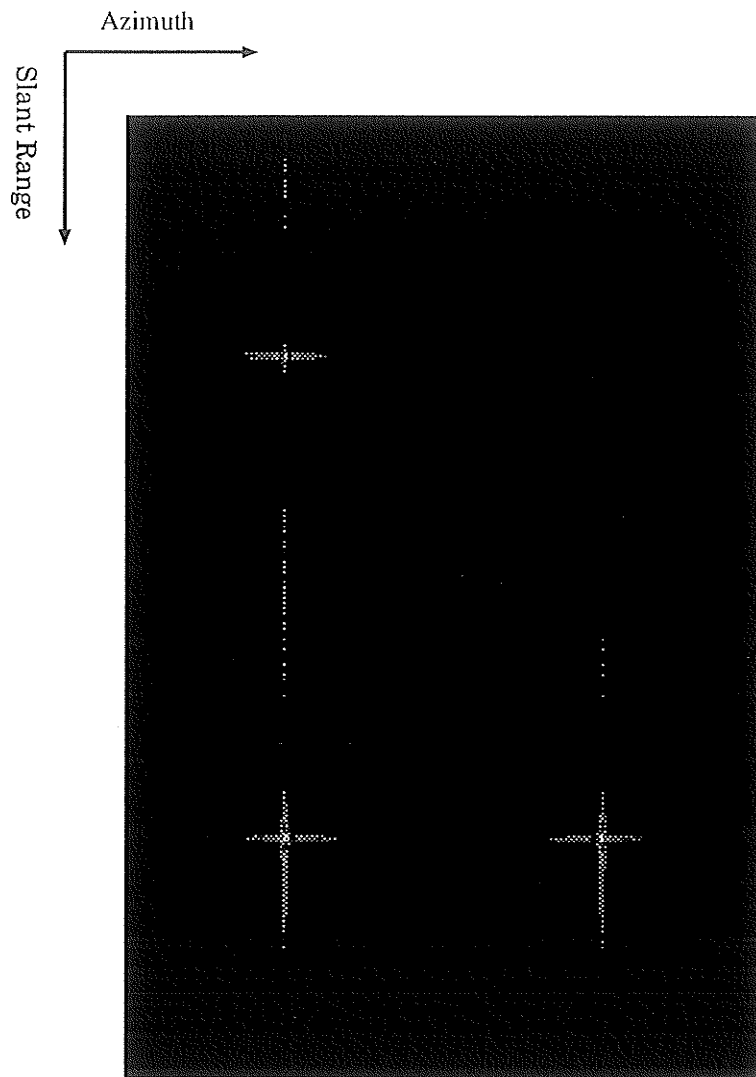
The next Seasat SAR simulation is carried out with the same size input data array (4096×4096), but the scatterers are assumed to have complex backscattering coefficients (Table 5.2). The image of the input signal is shown in Figure 5.6 (a) and the reconstructed image in Figure 5.6 (b). In addition to image reconstruction, the phase can also be estimated from the complex output data. The phase values at each corresponding scatterer's location are listed in Table 5.2. Figure 5.7 represents a combined perspective view image of the reconstructed phase value and the amplitude image in Figure 5.6 (b). In this combined image, estimated phase is used as an elevation map, and thus the height of amplitude image is proportional to the phase of the pixel. The gray level of amplitude image was inverted from that of the original image (Figure 5.6 (b)), that is, larger amplitude pixel is represented by darker gray level. The phase value at pixels having amplitude less than -40 dB around scatterers were excluded in the estimation. The error at the location of scatterers is less than 2° as listed in Table 5.2.

One simulation result may not be enough to draw a solid conclusion because above simulations have been conducted under the assumption of ideal flat-surface. Therefore extensions of further simulation and field test with actual SAR data must be done to prove whether the inversion approach can truly estimate the complex backscattering coefficient of the surface of the Earth. Nevertheless, the simulation result demonstrated above provides the grounds for the future development of the inversion method as a tool for estimating a surface scattering coefficient.



(a)

(continued to the next page)



(b)

Figure 5.6: Seasat simulation with three point scatterers having complex backscattering coefficients: (a) a simulated input signal of 4096×4096 pixels, and (b) the reconstructed image of 4096×4096 pixels.

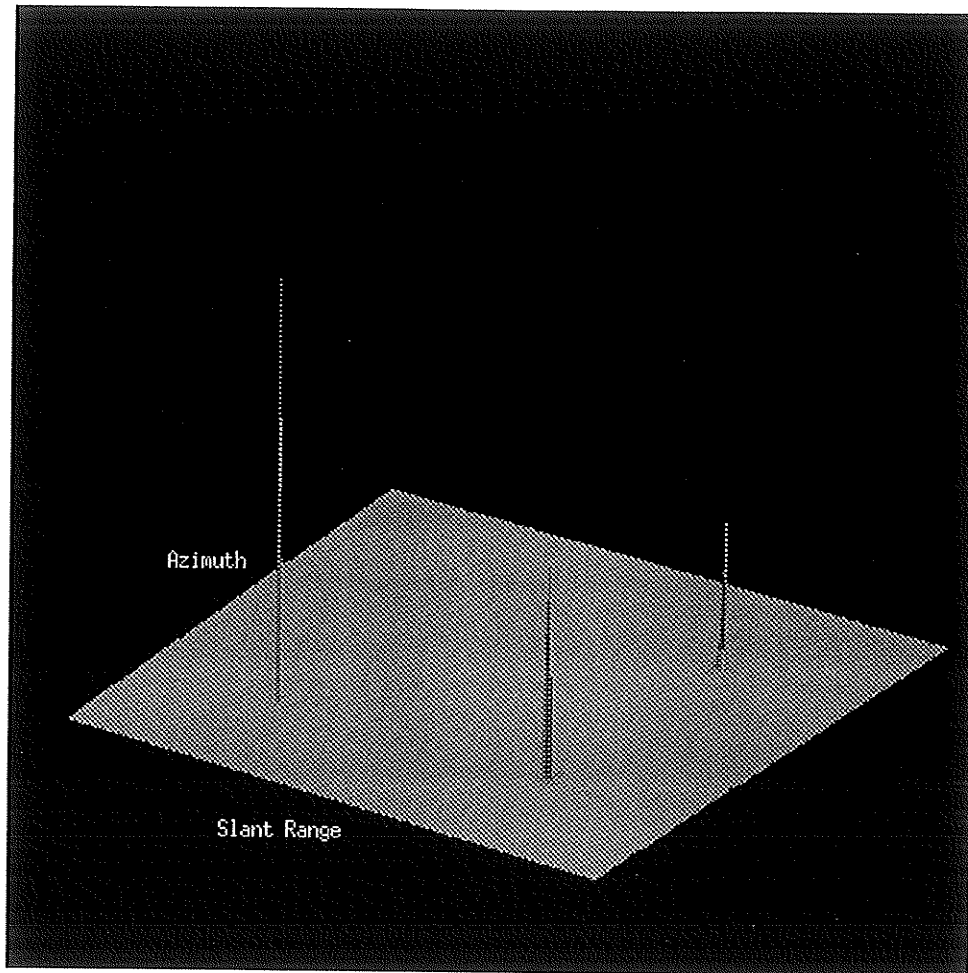


Figure 5.7: Combined perspective view image of amplitudes in Figure 5.6 (b) with the estimated phase. Phase was used as an elevation map, and gray level of amplitude image was inverted.

5.3 Processing of Real SAR Data

A set of SAR data was acquired on August 10, 1990, over a test area south of Ottawa, Canada, by the CCRS using a C-band airborne SAR system. The operating mode was C-band (wavelength 5.67 *cm*) nadir half swath mode in HH-polarization. The operating geometry of the nadir full swath mode is shown in Figure 5.8 (a). In the nadir half swath mode, a range line consists of 2048 range cells. Each cell of signal data is represented by a pair of in-phase and quadrature components, and each component is stored in 8-bits. The signal data were range compressed by an on-board processor. In this particular data acquisition, the on-board motion compensation was not carried out. The slant range and azimuth sampling intervals are about 4 *m* and 0.39 *m*, respectively. The pulse repetition frequency was 343 Hz, the platform velocity (V_s) was 134.76 *m/sec*, and thus the ratio PRF/V_s was 2.57 (m^{-1}). In the nadir mode, the receiver antenna is turned on about 13.2 μsec before the first arrival of the return signal. This will ensure the nadir line is included as a part of image.

The image of 2048×8192 (range \times azimuth) raw signal data is shown in Figure 5.9. To produce an image, complex signal data must be converted to amplitude data and then be discretized into a gray level scale of 0 to 255. Linear histogram stretching (e.g. Jensen [51]) is also performed. Because the range sampling interval (4 *m*) is about ten times larger than the azimuth sampling interval ($\simeq 0.39$ *m*), the amplitude of the signal data is required to be interpolated in the azimuth dimension in order to make an approximately

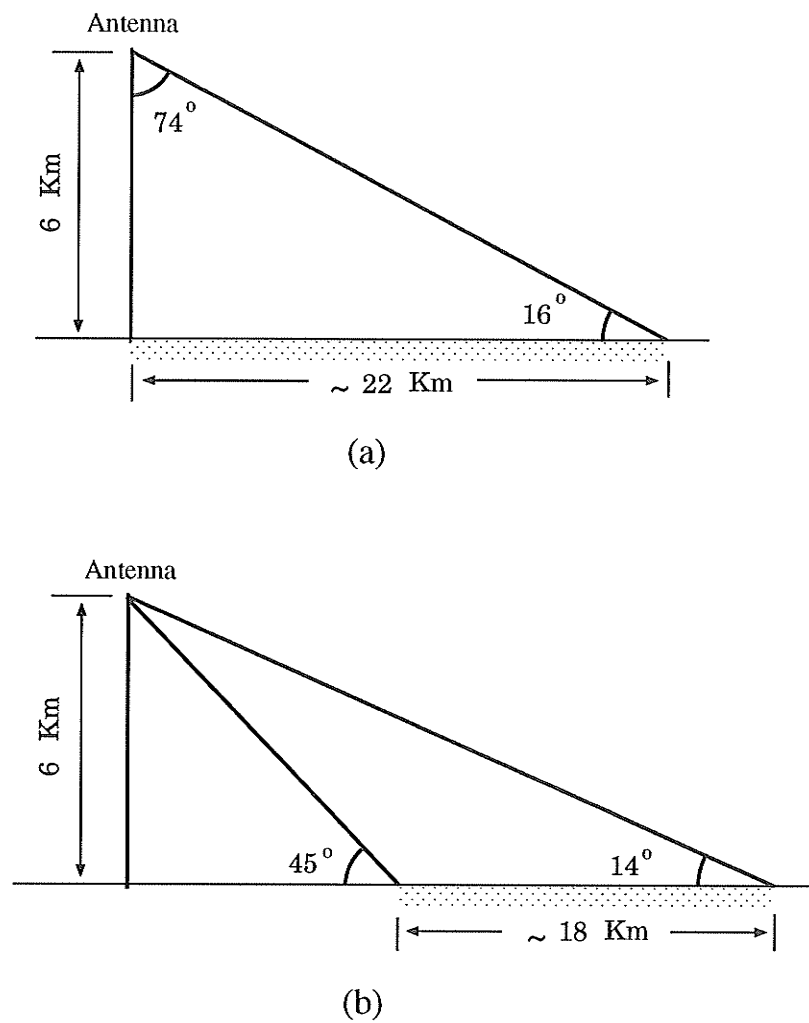


Figure 5.8: CCRS's airborne SAR operating geometries: (a) the nadir mode, and (b) the narrow swath mode.

square pixel with dimension of $\sim 4 \times 4$ *m*. A bright azimuth line at a near range represents the nadir line in Figure 5.9.

The average altitude of aircraft is 6 *km* as shown in Figure 5.8, and this value is the minimum slant range in the nadir mode. The farthest slant range is about 14 *km*, which is more than twice the minimum slant range. Due to this configuration, the wavefield processing approach may experience some difficulty in applying the far field approximation in Eq.(4.23). The spaceborne SAR configuration is more appropriate in terms of the far field approximation of wavefield than an airborne SAR configuration.

With the given platform velocity of 134.76 *m/sec*, the inversion processing was performed on a 2048×8192 input data array to obtain the result shown in Figure 5.10. The image shown in Figure 5.10 represents the magnitude of the complex backscattering coefficient.

Surface characteristics in this image can be roughly divided into two areas with different slant range: the upper half from nadir to middle slant range corresponds to agricultural areas; and the bottom half from middle to far slant range corresponds to Ottawa International Airport and various urban structures. The processed output shows better image reconstruction in the agricultural area where there are no point scatterers. The point scatterer is a discrete scatterer which gives a strong radar return. Although point scatterers can occur naturally, they are best seen in urban area due to corner reflectors such as buildings. Runways of Ottawa International Airport are discernible, but most urban areas in far range are very poorly imaged. The application of inversion processing alone on this data set fails to fully



Figure 5.9: Raw airborne SAR signal which was acquired near Ottawa, Canada, using CCRS's C-band airborne SAR system on August 10, 1990. Operating mode was the nadir half-swath mode in HH-polarization. Flight path direction is from top left to top right in this image.

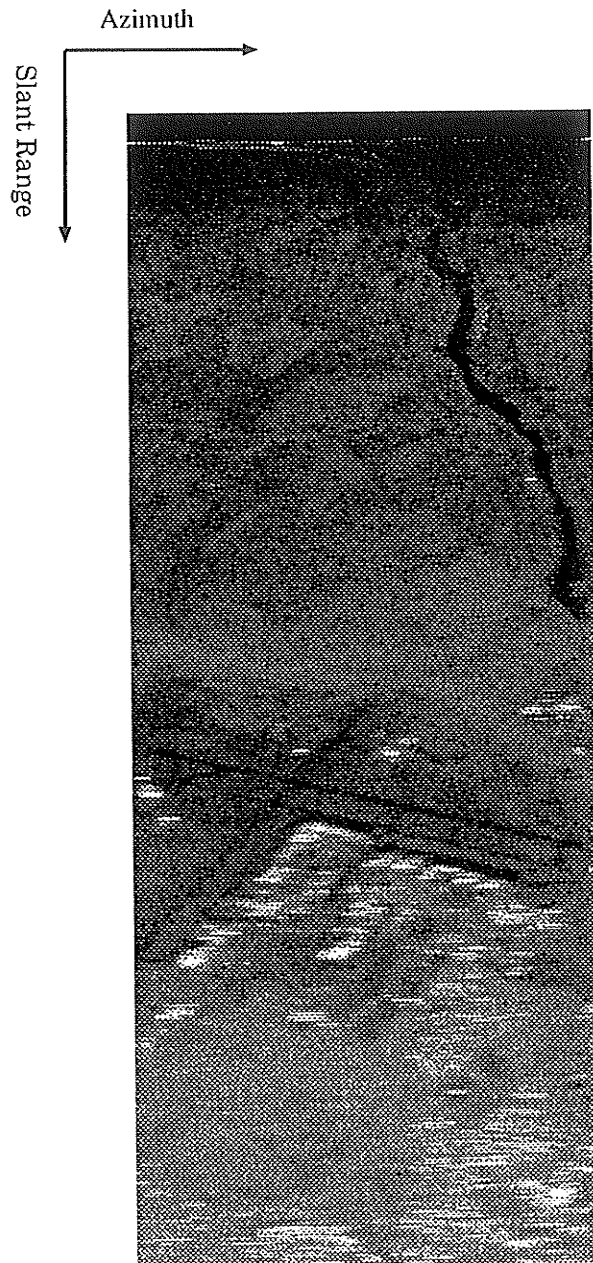


Figure 5.10: Reconstructed image after initial application of the inversion processing alone with platform velocity of 134.76 m/sec . The processed data array was 2048×8192 (range \times azimuth). Pixel size of the image was approximately $4 \times 4 \text{ m}$ after the interpolation in azimuth dimension which is shown from top left to top right.

reconstruct the image, specially at farther range. This results may be partly because of the nature of the nadir mode configuration and the inherent problem of the far field approximation, and partly because of the platform velocity changes discussed in section 4.5. Further focusing is necessary in this case.

Thus an additional focusing process is carried out over the bottom half of the test area. Estimation of the platform velocity is first required to properly perform the focusing process of Eq.(4.36). Moreira [83] suggested a method to estimate platform velocity by estimating two adjacent azimuth spectra. The changes in platform velocity are estimated, using the algorithm described by Moreira [83], at every 64 azimuth pixels and averaged over 16 azimuth lines. After examining the preliminary processed image (Figure 5.10), 512 azimuth pixels were used as the operator window length, and 32 pixels at both ends were overlapped with neighboring window output.

After the further focusing, a final single-look image in Figure 5.11 is obtained. Now point scatterers and details of the urban structure have become clearly visible.

The upper half (near range) of the image is still too dark to be discernible even after a linear histogram stretching. The gray levels of the subimage of the upper half were rescaled to make it visible as shown in Figure 5.12.

Both Figures 5.10 and 5.11 were printed on a HP laser printer which has a 150 ppi (point per inch) resolution. The resolution of the printer is not good enough to provide a high quality printout. For instance, an azimuth line consists of 820 pixels while HP laser printer can only print 360 points

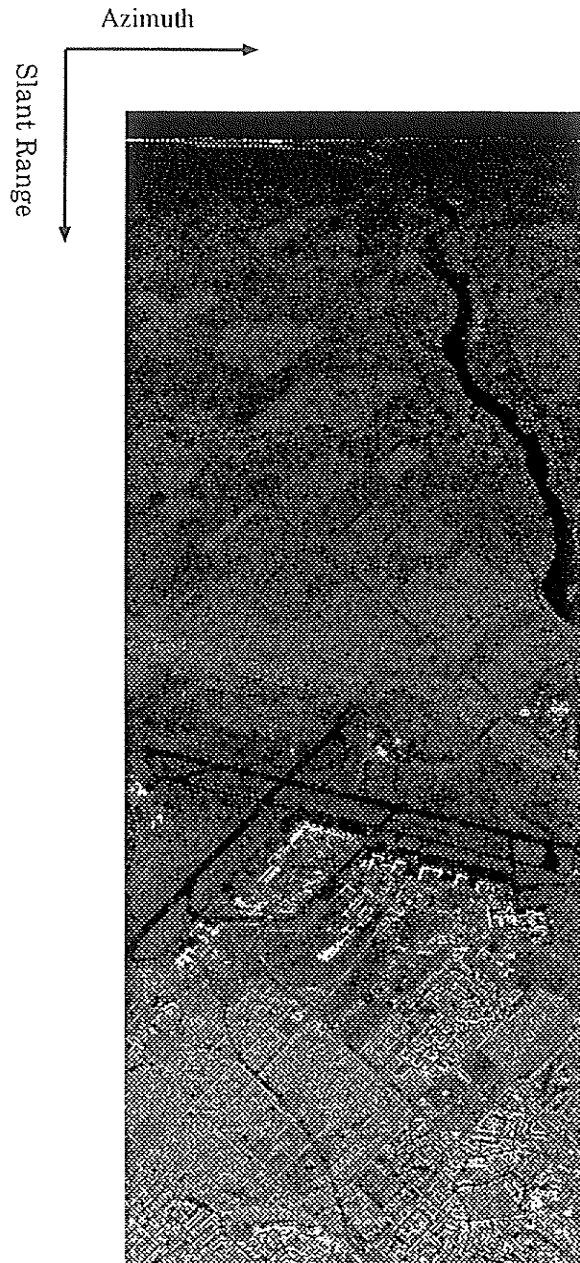


Figure 5.11: Reconstructed image after a further focusing process step. Image representation is same as the one shown in Figure 5.10.



Figure 5.12: The upper half (from the nadir to the middle range) area of the same image shown in Figure 5.11. Gray levels were rescaled.

over the 2.4 inches as shown in Figure 5.11. For this reason, certain small features in the images were blurred.

Enlarged image sfor the upper half and the bottom half (far range) area are shown in Figures 5.12 and 5.13, respectively.

A small area is selected to determine how well point scatterers are reconstructed. Figure 5.14 (a) is a close-up of the image near the junction of the two main runways shown in Figure 5.11. The image is magnified about four times compared with the image shown in Figure 5.11. The rectangle in Figure 5.14 (a) represents the selected subarea, in which two point scatterers are centered. The complex data corresponding to this area were then converted to a power representation and interpolated to obtain the result as shown in Figure 5.14 (b). The 3 dB width in azimuth is determined to be about 4.1 *m*. This 3 dB width (4.1 *m*) is about 1.5 times larger than that of narrow swath airborne SAR simulation (2.8 *m* in Figure 5.4). Therefore the reconstruction from actual SAR data acquired in nadir mode is not so good as the result of the simulation conducted using parameters of the narrow swath mode. The azimuth 3 dB width is, however, still good to be fitted into one resolution pixel.

In summary, the reconstruction by direct application of the inversion process resulted in a slightly underfocused image. Airborne SAR data set acquired in the nadir mode is definitely not most suitable for the test data of the new inversion method, because the ratio of the far range to the near range in this mode is very large. However, the image formation experiment based on the new inversion approach, incorporated with further focusing step, can



Figure 5.13: The bottom half (from the middle to the far range) of the test area as shown in Figure 5.11.

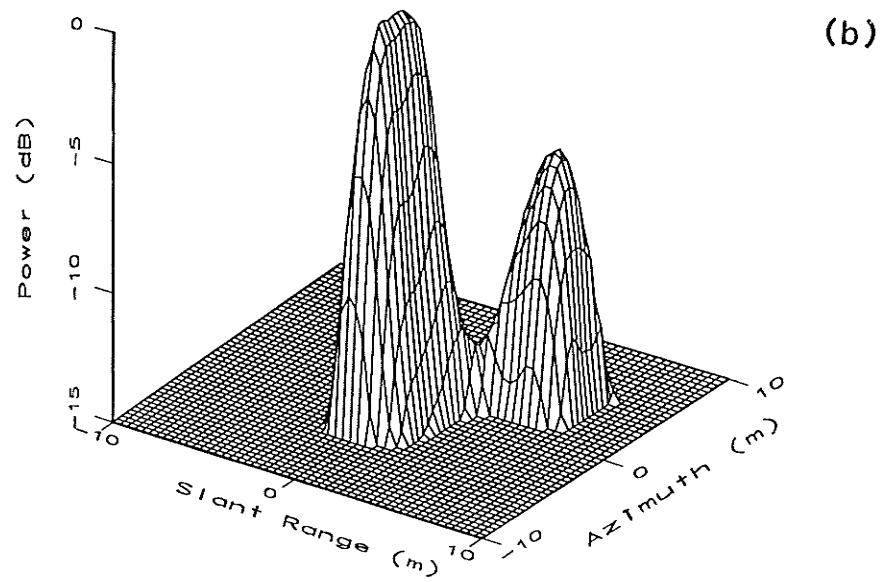
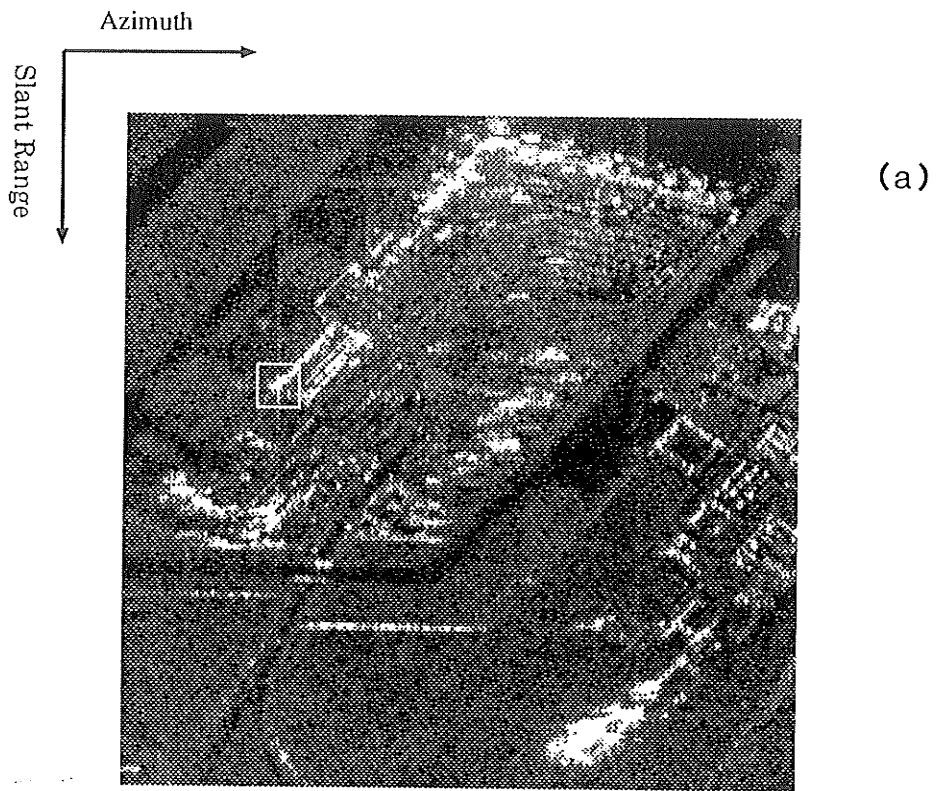


Figure 5.14: (a) The square represents the subarea where the point scatterers are located. (b) Power representation of the small subarea. The 3 dB width in azimuth is about 4.1 m.

successfully overcome the initial underfocusing problem experienced with this particular type of data set. Even though the inversion method is still in the early development stage, the test results are very positive and demonstrate the potential capability of the method.

Although the theoretical formulation of the inversion is now completed, certain details of the implementation of the approach are yet to be quantitatively investigated and tested. More quantitative experiments using satellite-borne SAR data are required to fully assess the performance of the new inversion approach.

Chapter 6

SAR Image Enhancement for Geological Application

6.1 Introduction

Since the early 1950's imaging radar has been used for geologic mapping, especially for surface structural information. SAR imagery is most sensitive to surface morphologic features, principally due to the strong dependence of radar backscattering process on surface roughness, slope, or dielectric constant (Trevett [101]). Among a number of geological applications of airborne and spaceborne SAR, this chapter focuses mainly on geologic lineament analysis and enhancement. The linear features are one of the most distinctive features on aerial and space images, and therefore the use of the term lineament has proliferated in remote sensing geology recently. The term lineament has been applied to imply alignment of different geological features such as shear zones, faults, rift valleys, joints and fracture traces, alignment of fissures, dykes, or plutons, and so on.

Geologic lineament study using remote sensing imagery has long been one

of the most important applications in the geological remote sensing. SAR images generally provide excellent lineament details compared with other sensor data, as demonstrated by many investigations using the Seasat SAR data and Landsat imagery (Harris [40]). However, there exist certain SAR system biases, and thus cautions must be taken when a set of SAR data is interpreted for geological applications. Important radar parameters for imaging of surface geological lineaments are: 1) radar look direction, 2) incidence angle, and 3) spatial resolution (Harris [40]).

Local incidence angle determines the intensity of the radar return: small incidence angle leads to intense backscattering (MacDonald [68]). As the incidence angle increases, the amount of backscattering energy decreases.

The radar look direction is defined by the radar squint angle given in Figure 1.1. In the CCRS's airborne C-SAR and the ERS-1 SAR case, the radar look direction is normal to the azimuth. The radar look direction is the most important factor in imaging lineaments (Harris [40]). The radar look direction biasing (or the radar azimuth biasing) problem has been addressed by Lowman *et al.* [66], and Masuoka *et al.* [75]. The radar look direction determines the preferential enhancement of the terrain: linear features within 20° of being parallel to the look direction are practically invisible (Lowman *et al.* [66]), whereas those within 20° of normal to the look direction are strongly highlighted (Harris [40]). For this reason, Lowman *et al.* [66] suggested that at least two look directions be mandatory in any SAR application project for geologic investigation.

This chapter is focused on two questions:

- 1) how can the trends of lineaments in a SAR image be determined efficiently and effectively ?, and
- 2) if two or more SAR data sets are made available, then how can these multiple SAR data sets be optimally combined for geological interpretation ?

To determine the dominant lineament trends on a SAR image, the Radon transform (Radon [88]) analysis technique is tested first. The plot of the maximum amplitude of Radon transform versus slope is found to be very useful for analyzing surface geologic lineaments. An experiment is carried out using a set of airborne C-SAR and ERS-1 SAR data from the Sudbury Basin. This experiment demonstrates that the radar look direction biasing as well as dominant lineaments trend can be well analyzed through the Radon transform.

Correlation using the Radon transform is also investigated to evaluate whether this technique would be useful for discriminating certain geologic structures in a SAR image. Experimentation with airborne C-SAR data from the Wekusko Lake test area is conducted.

The task of merging two or more SAR data sets into one image is investigated in three different approaches:

- 1) simple addition or subtraction,
- 2) directional derivative followed by subtraction, and
- 3) the principal components analysis (PCA) approach.

Each test is carried out with the CCRS's airborne C-SAR and the ERS-1 SAR data from the Sudbury Basin test area.

Geological interpretation of the selected test areas is beyond the scope of this thesis.

6.2 Determination of Geological Structures Using Radon Transform

6.2.1 Introduction

Geological lineament mapping using remote sensing data has been the most commonly adopted technique in geological remote sensing applications. Lineaments that appear on a SAR image are usually interpreted visually (Harris [40]). Instead of visual detection of lineaments, the Radon transform can be applied to the SAR data with the objective of geologic structure analysis.

The Radon transform has been widely used in pattern recognition for detecting linear features from an image (Illingworth and Kittler [49]). It has been also applied to problems such as ship wake detection by analyzing SAR images (Rey *et al.* [94]). Two approaches to the Radon transform in geological remote sensing of SAR data are investigated in this chapter including: first, geological lineaments analysis, and second, correlation using the Radon transform to determine a certain geologic structure.

Application of the Radon transform for determination of geologic lineaments is straightforward. By detecting pixels of relatively large amplitude in the Radon transform space, certain groups of lineaments in a SAR image can be determined. This study is focused on developing a technique to determine dominant trends of lineaments in a test SAR data rather than detecting individual lineaments. A plot of the maximum amplitude of Radon transform versus slope is found to be an effective criterion in identifying major trends of specific geologic surface features in the SAR data. An experiment was car-

ried out using the CCRS's airborne C-band and ERS-1 SAR data over the Sudbury Basin. Results of the Radon transform analysis demonstrate that it is very efficient and effective for determining dominant trends of surface lineaments from SAR data. However, the radar look direction bias should be carefully analyzed in the process.

The second application is correlation using the Radon transform for locating geologic features of specified shape in a given SAR image. The Radon transform of two-dimensional convolution and correlation are derived in this study, and proved respectively to be one-dimensional convolution and correlation. A test using airborne SAR data from the Wekusko Lake area, Manitoba, is partly successful in locating fold structures through a combined process of screening in the Radon transform space and correlation.

6.2.2 Radon Transform Analysis of Lineaments

The Radon transform has been used widely for linear feature detection in pattern recognition (Illingworth and Kittler [49]). The Radon transform was also utilized to detect ship wakes on a SAR image which was contaminated with speckle noise (Murphy [84], Rey *et al.* [94]). For detection of individual lineaments, a method using the Hough transform can be applied to automatic detection of lineaments (Wang and Howarth, [105]).

In geological applications of SAR imagery, analysis of the dominant trends of lineaments is as important as detecting individual lineaments. An approach for determining dominant direction of geological lineaments in a SAR image through the Radon transform is investigated below.

Coordinates for the image space and the Radon space used in this thesis are as follows. The image space is defined by (x, y) coordinate as shown in Figure 6.1. The origin of x is at the center of vertical axis, while the origin of y is at the left-most pixel. The Radon space is defined by (p, z) coordinate. Slope of a line is defined by p , which is zero if parallel to x -axis, and positively increases clockwise as shown in Figure 6.1. The coordinate z is defined by the interception of a line at $x = 0$. Given this coordinate convention, the Radon transform is given by

$$\begin{aligned}\Psi(p, z) &= \int_{-\infty}^{\infty} \phi(x, z + px) dx \\ &= \iint_{-\infty}^{\infty} \phi(x, y) \delta(y - z - px) dx dy\end{aligned}\quad (6.1)$$

(Radon [88]). The notation

$$\phi(x, y) \xleftrightarrow{R.T.} \Psi(p, z) \quad (6.2)$$

will be used to indicate that the function $\phi(x, y)$ and $\Psi(p, z)$ are related by the Radon transform in Eq.(6.1).

Various properties of the Radon transform were summarized in Deans [25] (pp.65-95), and Durrani and Bisset [28] (p.1181, Table 1). Three Radon transform pairs are summarized in Table 6.1 as examples.

An example depicted in Figures 6.2 and 6.3 illustrate the Radon transform pairs of a point, lines and an hyperbola. The point, two straight lines, and one hyperbola are respectively mapped onto a line, points, and ellipse in the Radon transform space (p - z space) as in Figure 6.3. In this example, one can easily realize that the contribution to Radon transform of an isolated point

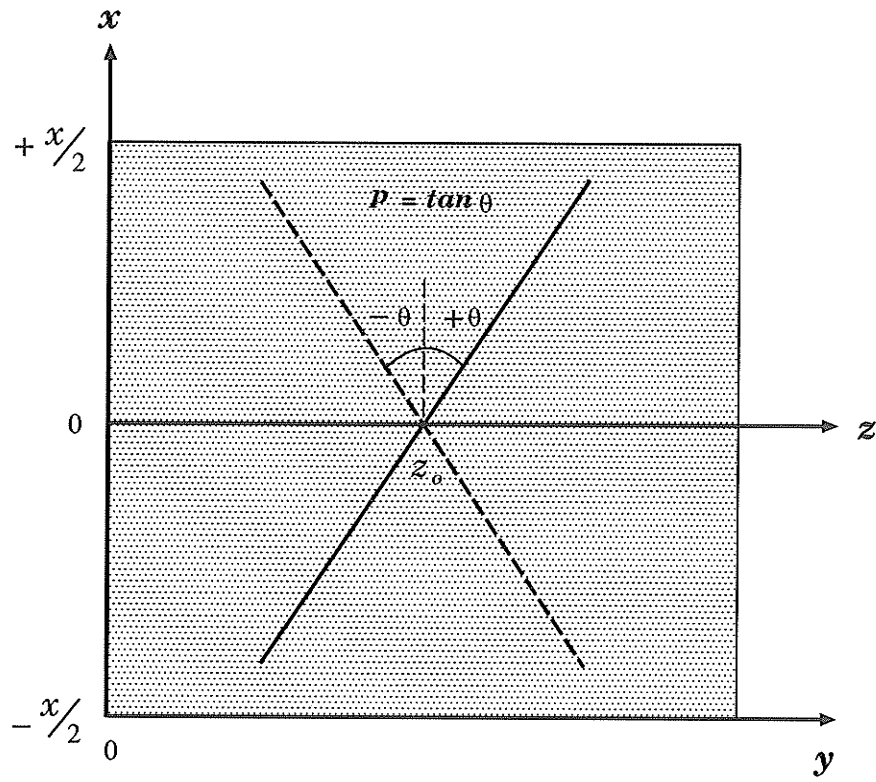


Figure 6.1: Image coordinate for the Radon transform.

Table 6.1: Examples of Radon transform pair.

	Image space	Radon transform
Point	$\delta(x - a, y - a)$	$z = b - ap$ (Line)
Line	$y = p_0x + z_0$	$\delta(p - p_0, z - z_0)$ (Point)
Hyperbola	$y = a\sqrt{x^2 + b^2}$	$z = b\sqrt{a^2 - p^2}$ (Ellipse)

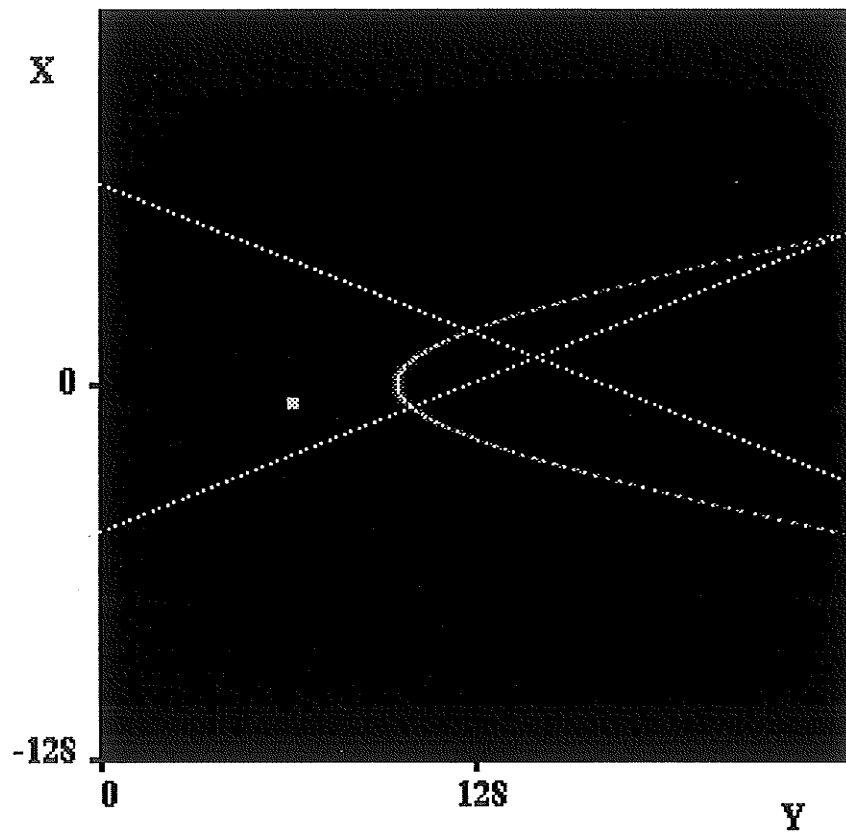


Figure 6.2: Point, lines, and hyperbola in the image space.

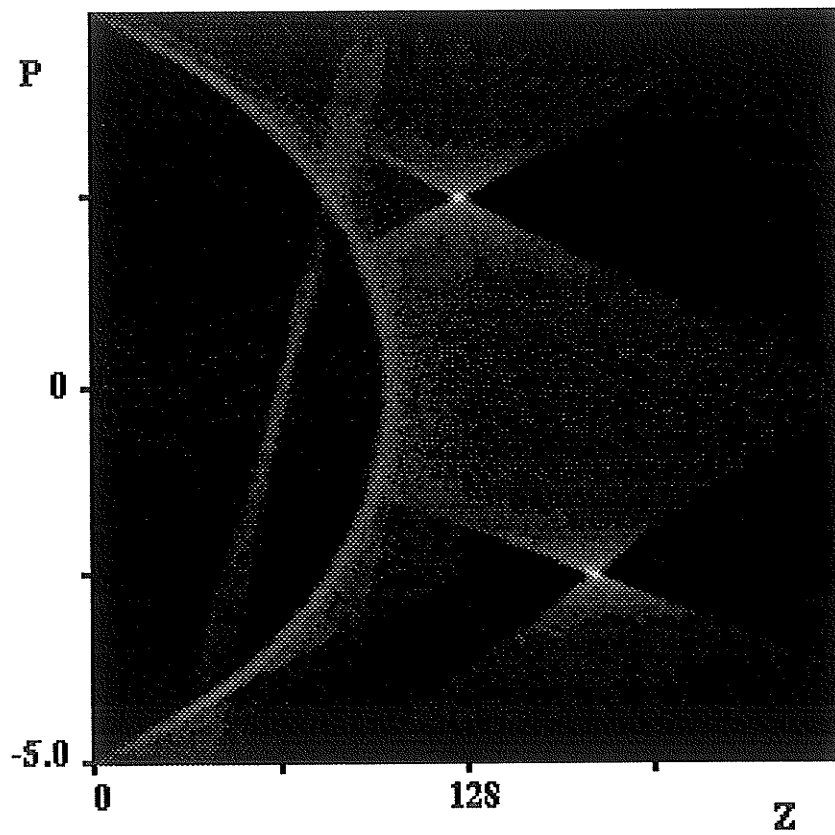


Figure 6.3: Radon transform of point, lines, and hyperbola.

scatterer (e.g. corner reflectors, or speckle noise in a SAR image) is much less significant than those of lines or hyperbola.

Numerical implementation of the Radon transform was made by employing a fast algorithm (Haneveld and Kerman [36]). This algorithm was initially developed for the fast τ - p transform which is a discretized Radon transform developed for seismic application (Haneveld and Kerman [36]). The maximum slope (maximum p -value) used in this study is ± 5.0 (± 78.7 in degrees).

Two sets of SAR data from the Sudbury Basin, Ontario, were selected for the test. The locations of Sudbury Basin and Wekusko Lake test sites are shown in Figure 6.4. The two SAR data sets include the CCRS's airborne C-band SAR data and the ERS-1 C-band SAR data, and images are respectively shown in Figures 6.5 and 6.6. The ERS-1 image data was coregistered to airborne C-band SAR image.

The Sudbury Basin is located in eastern Ontario, Canada, and is a north-east trending ellipsoidal geological structure. The SAR images provide a good representation of the topographic features and certain surface geological lineaments including faults, dykes, and fractures. The topography imaged in the SAR data includes the relatively rugged and mountainous North Range of the Sudbury Basin (northwest parts of images in Figures 6.5 and 6.6), and the low relief interior basin and South Range. An interesting aspect of the C-band SAR imagery over this area is that the terrain is uniformly rough relative to the radar wavelength (5.6 cm). Therefore the tone of the C-band imagery over this area is dominated by the local incidence angle (i.e. by topography alone) (Lowman [67]). Detailed geologic interpretation of the

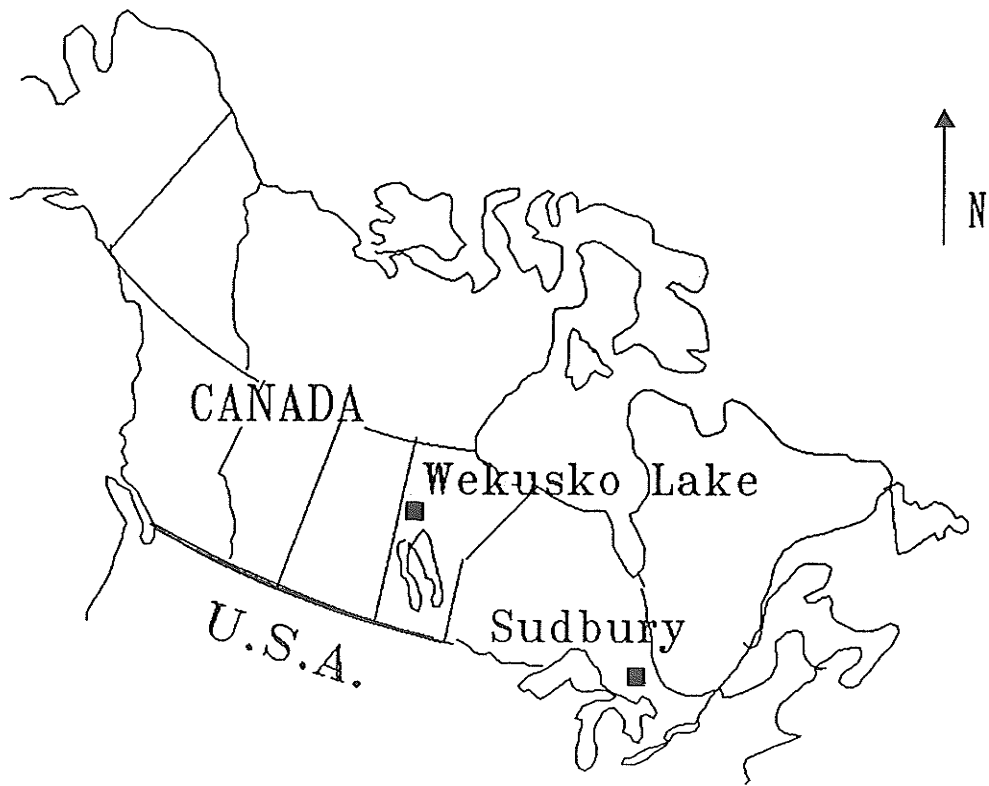


Figure 6.4: Location map of Sudbury Basin and Wekusko Lake test area.

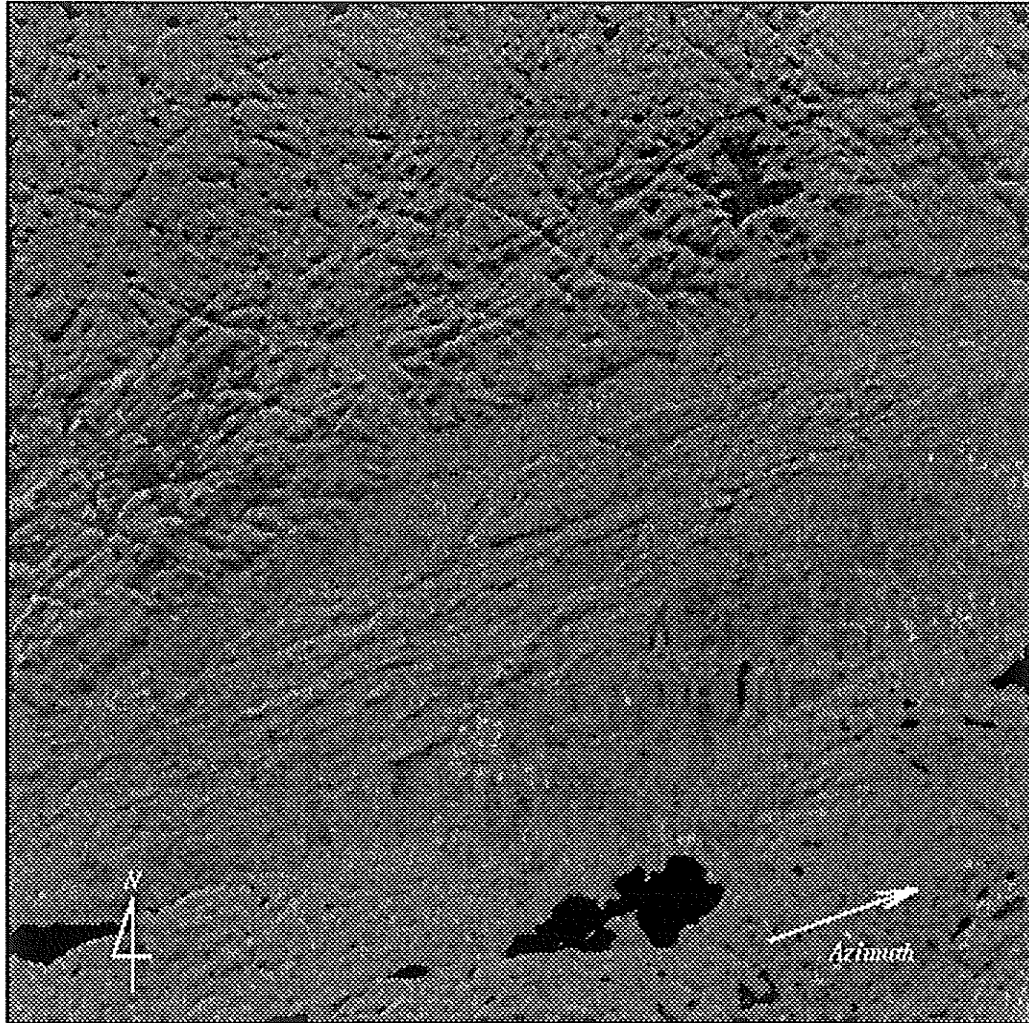


Figure 6.5: CCRS's airborne C-band SAR image over the Sudbury Basin.

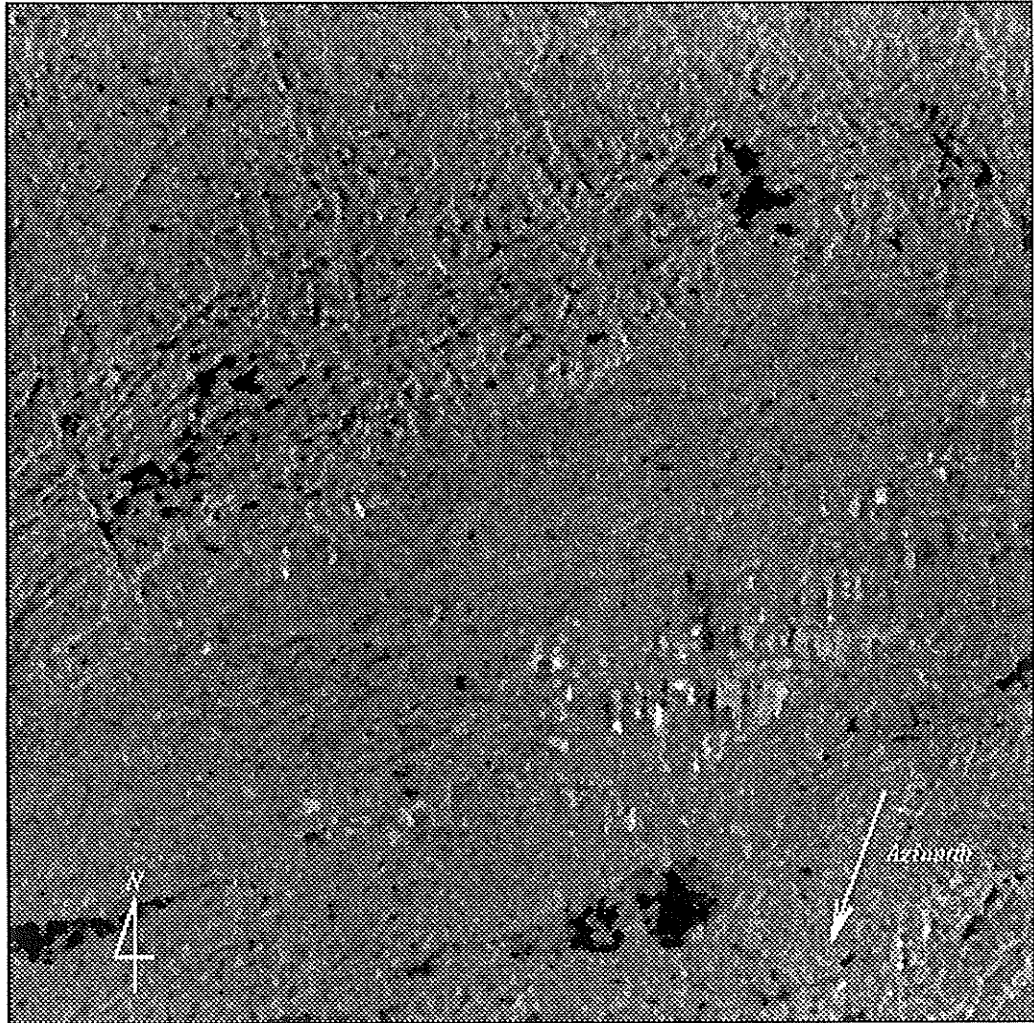


Figure 6.6: ERS-1 SAR image over the Sudbury Basin.

C-band SAR imagery over this area is found to Lowman [67].

This study is concentrated specifically on lineaments in the North Range such as northeast trending fractures, north of northwest trending faults, and west of northwest trending dykes. Some selected geological lineaments in the North Range, transferred from a published geological map (Ontario Geological Survey Map 2491, Pye *et al.* [87]), are superimposed on the airborne SAR data in Figure 6.7.

The airborne SAR image (Figure 6.5) generally depicts surface geological details much better than the ERS-1 SAR image (Figure 6.6). Airborne C-SAR image is specially effective in imaging the interior of the Sudbury Basin where there is relatively low relief region. Although the airborne SAR data provides detailed structures better than the ERS-1 SAR data, the north to northwest trending linear features are poorly imaged in the airborne SAR imagery due to the flight direction (about $70^\circ NE$). Conversely, the ground track of the ERS-1 platform is about $20^\circ SW$, which results in better imaging of north to northwest trending geologic structures, but northwest to eastwest trending dykes are hardly visible. The look direction effects are most conspicuous in the North Range of Sudbury Basin (northwest quadrangle of the images).

The Radon transforms of the airborne SAR and ERS-1 SAR data (Figure 6.5 and 6.6) are plotted using gray level in Figure 6.8 and 6.9, respectively. These Radon transform are obtained after the image digital number (DN) value (from 0 to 255) is rescaled into $(-1.0, 1.0)$. In Figure 6.8 and 6.9, dark stripes having positive slopes are seen. The relationship between a point

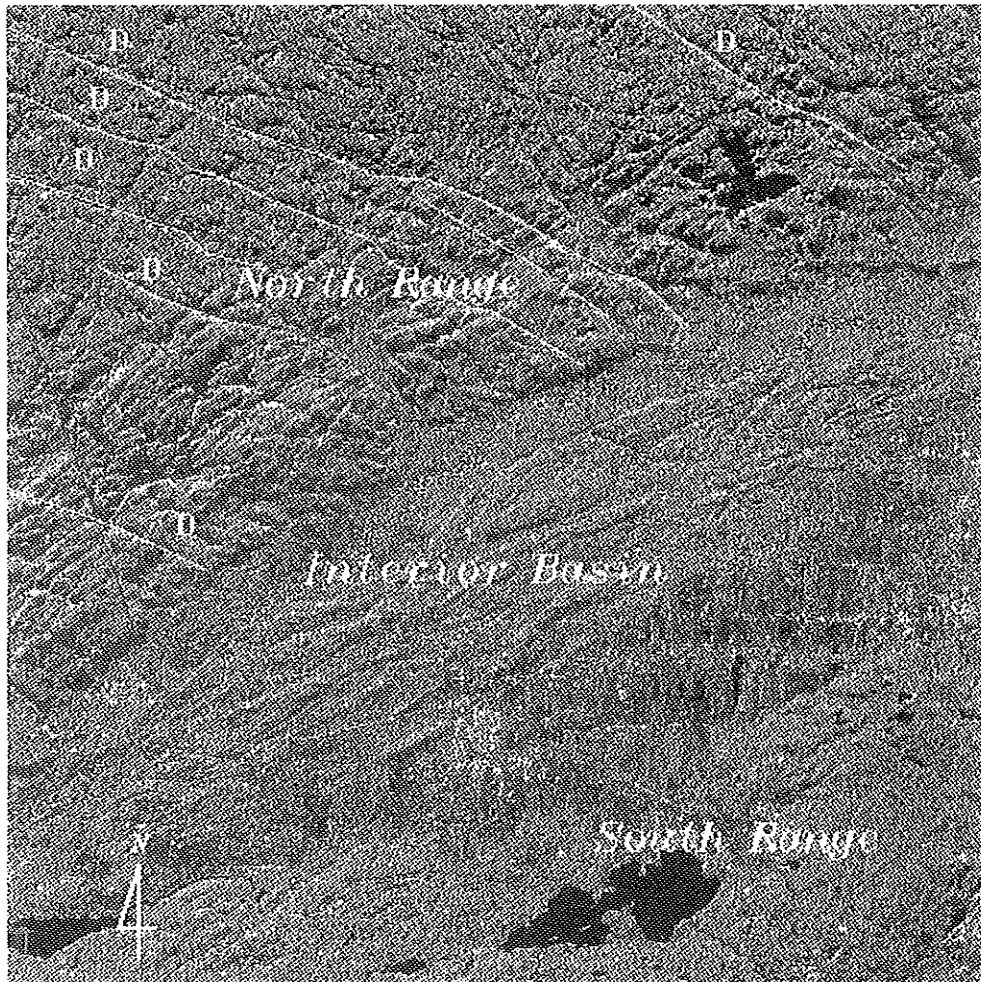


Figure 6.7: Airborne SAR image from the Sudbury Basin superimposed by geological lineaments: F – Fault; D – Dyke.

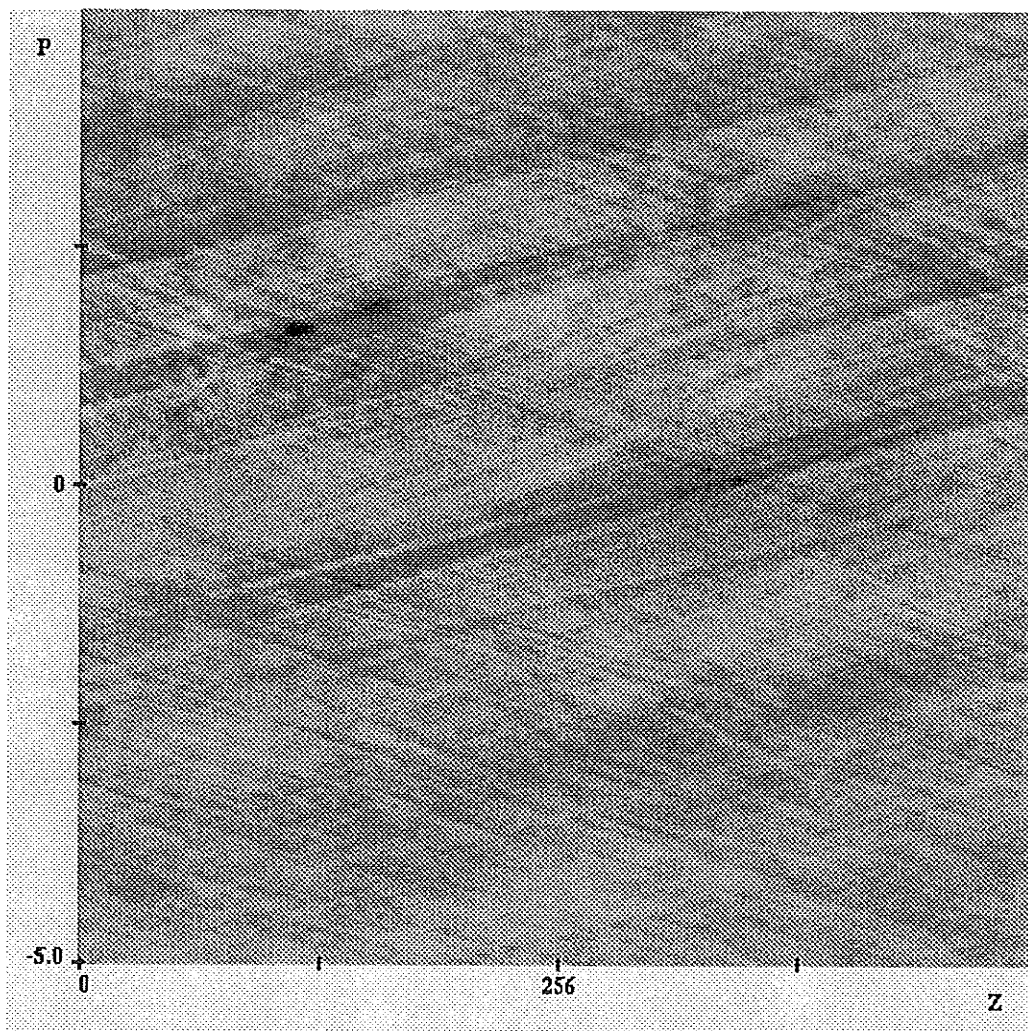


Figure 6.8: Radon transform of airborne SAR data.

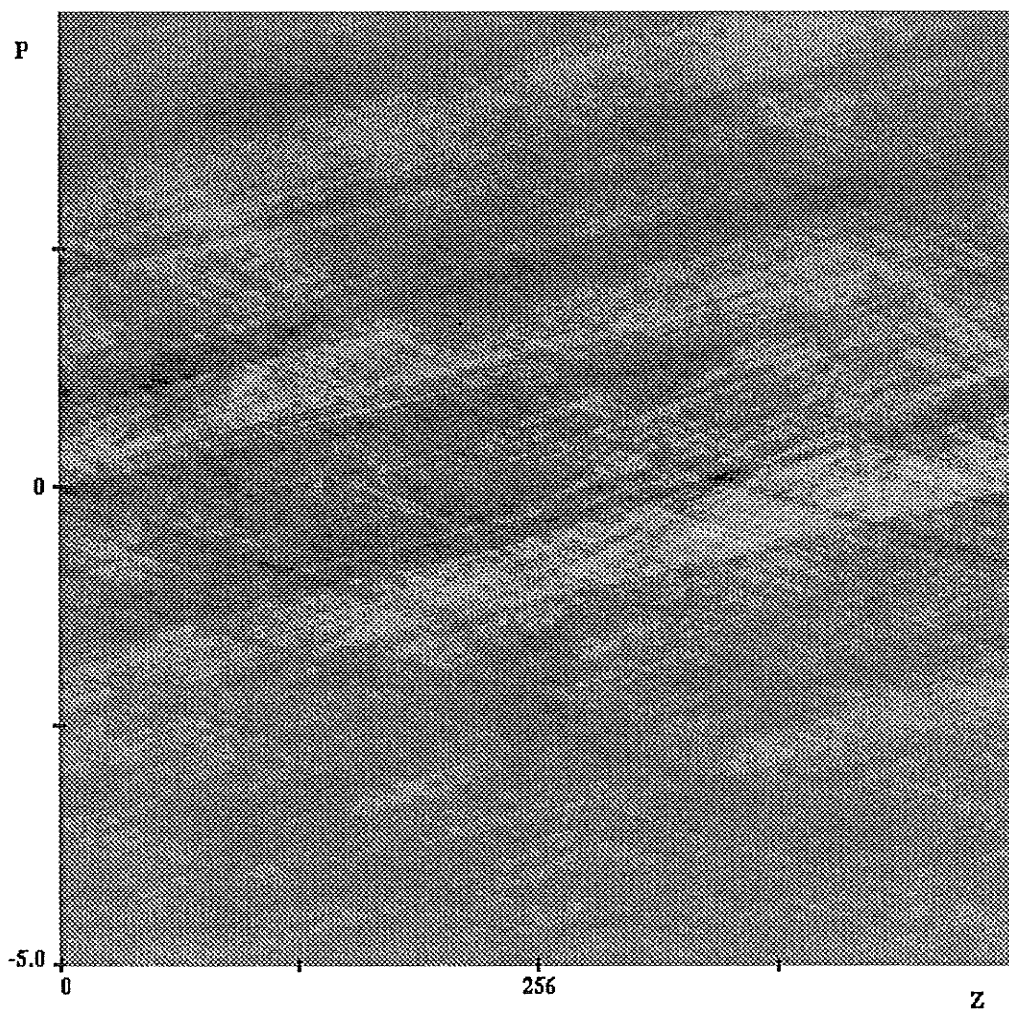
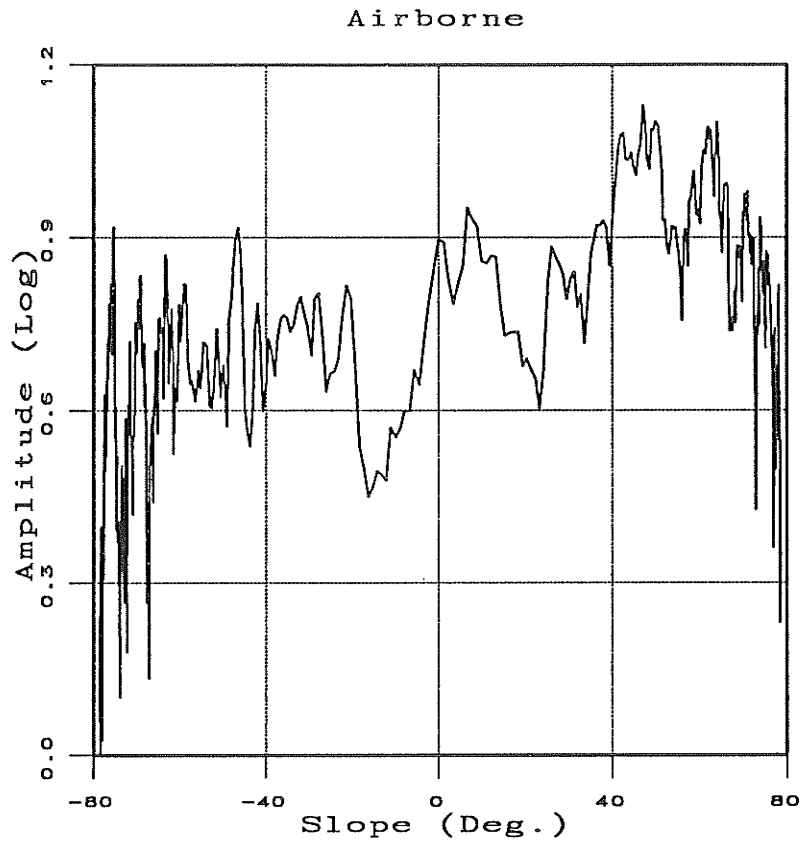


Figure 6.9: Radon transform of ERS-1 SAR data.

in the image space and the line in the Radon transform space indicates that these stripes can be interpreted as contributions from lakes which are dark areas in the SAR images. Bright spots in the Radon transform correspond to lineaments in the SAR image.

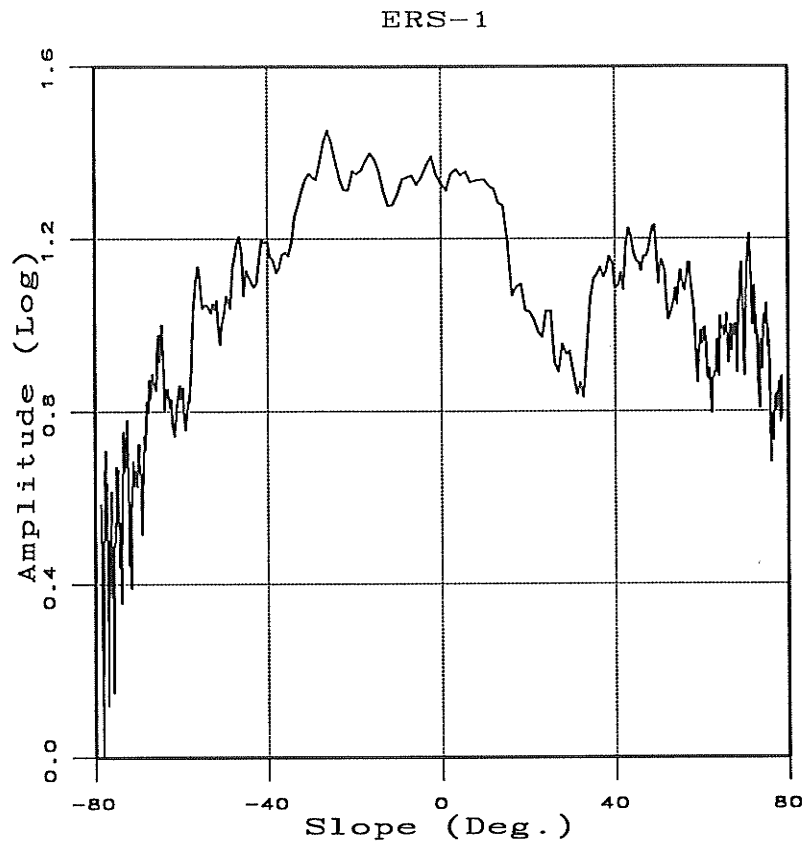
The method of determining dominant trends of geological lineaments is developed, and described below. If the focus of the study is on the major orientation rather than detection of individual lineaments, the relative change in amplitude of Radon transform with respect to p (or slope) is important. The first step is to detect the maximum amplitude at each constant p -value. The next step is to plot the changes of this maximum amplitude versus slope (p in degree) as shown in Figures 6.10 and 6.11.

Figures 6.10 (a) and (b) respectively are plots for the CCRS's airborne and ERS-1 data, plotted together on the same scale in Figure 6.11. The plotted values are roughly divided into three ranges: first the range from about -79° to -40° , the second from -40° to $+35^\circ$, and the third from $+35^\circ$ to about $+79^\circ$. The Radon transform of the ERS-1 data (Figure 6.10 (b)) shows large amplitude (notice the logarithmic scale) between -40° and $+15^\circ$, and a peak value at -26° . In the same range the airborne SAR data (Figure 6.10 (a)) is characterized with an amplitude low at -16° . This means that north to northwest trending lineaments are highlighted on the ERS-1 SAR image, while they are poorly imaged by the airborne SAR. This effect can be explained by the SAR look direction biasing (Harris [40], Lowman *et al.* [66]). As it was pointed out earlier, the azimuth direction of the airborne SAR was about $70^\circ NE$ and that of ERS-1 was about $20^\circ SW$. The airborne SAR look



(a)

(continued to the next page)



(b)

Figure 6.10: Plot of maximum amplitude of Radon transform versus angle: (a) airborne SAR data, (b) ERS-1 SAR data.

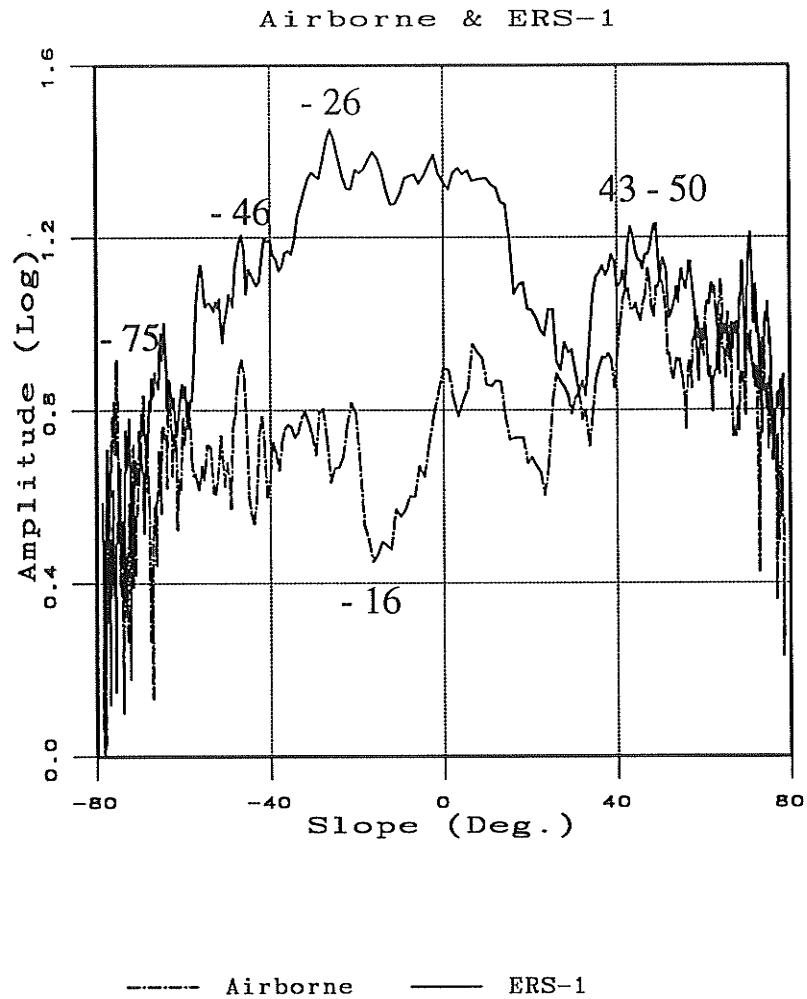


Figure 6.11: Plot of maximum amplitude of Radon transform versus angle: airborne SAR data in dotted line, and ERS-1 SAR data in solid line.

direction bias results in poor imaging of north to northwest trending surface geological lineaments in the study area. Fortunately, the ERS-1's ground track were such that these particular features were highlighted by ERS-1 SAR. The Radon transform experiment clearly demonstrates the SAR look direction effects.

The Radon transform amplitude high in the range from $+43^\circ$ to $+50^\circ$ in both airborne and ERS-1 case (Figure 6.10 (a) and (b)) may represent northeast trending linear features in the North Range. The range between -79° and -40° with a peak at -44° in the Radon transform space corresponds to northwest to eastwest trending lineaments (Figure 6.10 (a) and Figure 6.11). The peak at -46° also appears in the ERS-1 data (Figure 6.10 (b) and Figure 6.11), and it may represent northwest trending lineaments in the North Range.

The other interesting peak at -72° in the airborne data is not significant in the ERS-1 case. The $70^\circ NW$ striking linear features, which are clearly visible at near left-top in the airborne SAR image (Figure 6.5), may represent dykes as shown in Figure 6.7. These lineaments are not visible in ERS-1 SAR image (Figure 6.6).

Evaluating trends of lineaments is an important task in the geological application of SAR (Harris, [40]). As demonstrated in this section, the Radon transform technique for analyzing the geological lineament is very efficient and effective in determining the dominant trends of lineaments from SAR digital image data.

6.2.3 Correlation Using The Radon Transform

Among the various properties of the Radon transform, the convolution and correlation property have been considered to be not as useful as other properties. Many authors, for instance, Deans [25] (pp.95, Eq.(10.1)), and Durrani and Bisset [28] (p.1181, Table 1), have pointed out that the Radon transform of convolution is the convolution of the Radon transforms. Similarly, the Radon transform of correlation is the correlation of the Radon transforms. Compared to the Fourier transform theorems in which the Fourier transform of a convolution pair becomes a product of the Fourier transforms, it was judged that convolution or correlation through the Radon transform was not worth performing.

However, it can be shown that two-dimensional convolution (or correlation) of the Radon transform is simply a one-dimensional convolution (or correlation) in the z -dimension. Thus, convolution or correlation through the Radon transform increases the computational efficiency when it is applied to two-dimensional data. Consequently, correlation through the Radon transform can be applied to determine the location of a certain geological structure of specified shape in two-dimensional survey data such as SAR images.

The Radon transform of two-dimensional convolution and correlation is derived as follows. The shifting property of the Radon transform is given as (Durrani and Bisset [28], pp.1181, Table 1.)

$$\phi(x - a, y - b) \xleftrightarrow{R.T.} \Psi(p, z - b + ap) . \quad (6.3)$$

Two-dimensional convolution is defined as

$$q(x, y) = \iint_{-\infty}^{\infty} f(x', y') g(x - x', y - y') dx' dy' . \quad (6.4)$$

Using Eq.(6.1) and (6.4), the Radon transform of two-dimensional convolution is then written as

$$\begin{aligned} Q(p, z) &= \iint q(x, y) \delta(y - z - px) dx dy \quad (6.5) \\ &= \iint \left[\iint f(x', y') g(x - x', y - y') dx' dy' \right] \delta(y - z - px) dx dy \\ &= \iint \left[\iint g(x - x', y - y') \delta(y - z - px) dx dy \right] f(x', y') dx dy . \end{aligned}$$

The inside of the square bracket is the Radon transform of a shifted function $g(x - x', y - y')$. Using the shifting property in Eq.(6.2), the above equation can be reduced to

$$Q(p, z) = \iint_{-\infty}^{\infty} f(x', y') G(p, z - y' + px') dx' dy' \quad (6.6)$$

where

$$g(x, y) \xleftrightarrow{R.T.} G(p, z) . \quad (6.7)$$

Eq.(6.6) can be rewritten as

$$\begin{aligned} Q(p, z) &= \iint f(x', y') \left[\int G(p, z - z') \delta(z' - y' + x'p) dz' \right] dx' dy' \\ &= \int G(p, z - z') \left[\iint f(x', y') \delta(y' - z' + x'p) dx' dy' \right] dz' \quad (6.8) \end{aligned}$$

Since the inside of the square bracket is the Radon transform of $f(x, y)$, the equation results in

$$Q(p, z) = \int_{-\infty}^{\infty} F(p, z) G(p, z - z') dz' \quad (6.9)$$

where

$$f(x, y) \xleftrightarrow{R.T.} F(p, z) . \quad (6.10)$$

Therefore, two-dimensional convolution in (x, y) domain reduces to only one-dimensional convolution in the Radon transform domain (p, z) , that is

$$f *_{xy} g \xleftrightarrow{R.T.} F *_z G \quad (6.11)$$

where

$$\begin{aligned} f(x, y) &\xleftrightarrow{R.T.} F(p, z) \\ g(x, y) &\xleftrightarrow{R.T.} G(p, z) \end{aligned} \quad (6.12)$$

and $*_{xy}$ denotes two-dimensional convolution in x - and y -dimension, while $*_z$ denotes one-dimensional convolution in z -dimension.

Similarly, the Radon transform of two-dimensional correlation can be proved to be

$$f \otimes_{xy} g \xleftrightarrow{R.T.} F \otimes_z G \quad (6.13)$$

where \otimes_{xy} denotes two-dimensional correlation in x - and y -dimension, while \otimes_z denotes one-dimensional correlation in z -dimension.

In the above derivatin it was shown that the Radon transform of two-dimensional convolution or correlation respectively reduces to one-dimensional convolution or correlation. As regards computational efficiency, convolution

or correlation through the Radon transform is not yet as attractive as the Fourier transform approach. However, there are possible advantages of the Radon transform approach over fast Fourier transform convolution. The Radon transform approaches tested in this chapter are robust even when SAR data is corrupted by noise (also see Murphy [84]). Certain filtering or screening processes in the Radon space can be applied to effectively reduce the noise level as a part of the convolution or correlation process. In addition, the total number of operations can be further reduced if the Radon transform of a certain geometry can be defined by a simple function.

The following model test is carried out using hyperbolas. The test input data shown in Figure 6.12 are composed of 256×256 pixels, and the apexes of two hyperbolas are located at $(64, 71)$ and $(-64, 111)$. The task is to find the coordinates of these apexes by applying correlation through the Radon transform technique with a reference template. A reference template can be made by a specified shape which is to be sought in a given image. For this test, the reference template is selected as a hyperbola having its apex at $(0, 11)$ as shown in Figure 6.13. In the actual operation, the reference template is not necessary to be prepared in the x - y space. Instead, the Radon transform of a hyperbola is estimated to be an ellipse (the relation listed in Table 6.1). A unit value is assigned to the nearest neighborhood pixels along the ellipse in p - z domain. Thus there is only one non-zero pixel at each fixed p -value. Correlation in z -dimension with this reference template in the Radon space can be accomplished now by simply shifting the Radon transform of the original image in the z -dimension. The result of correlation

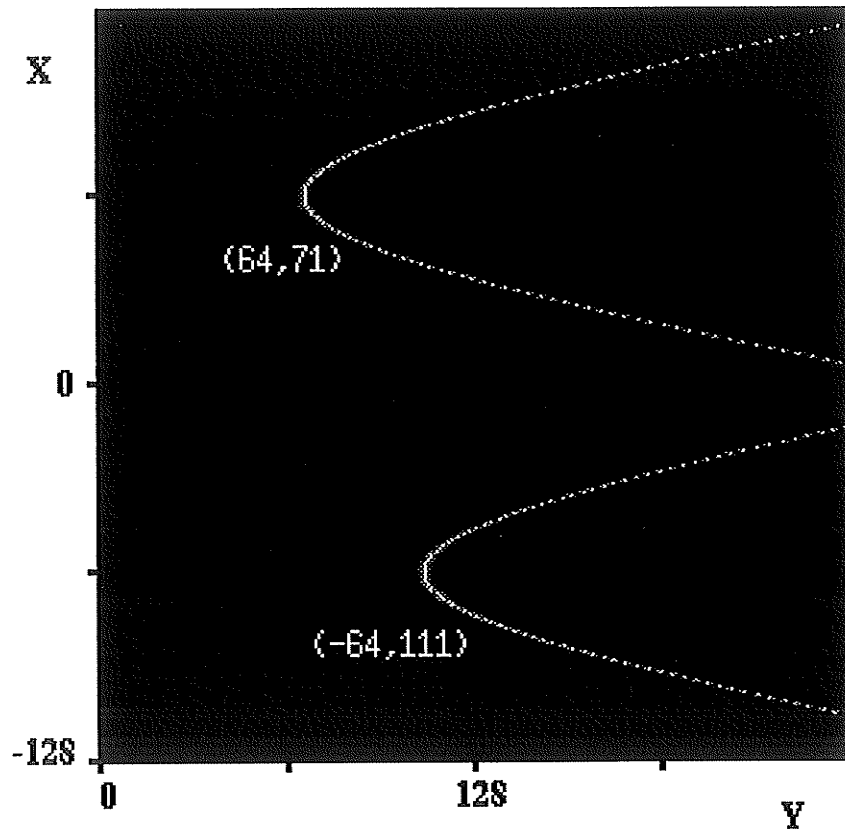


Figure 6.12: Model test for correlation through the Radon transform: input data.

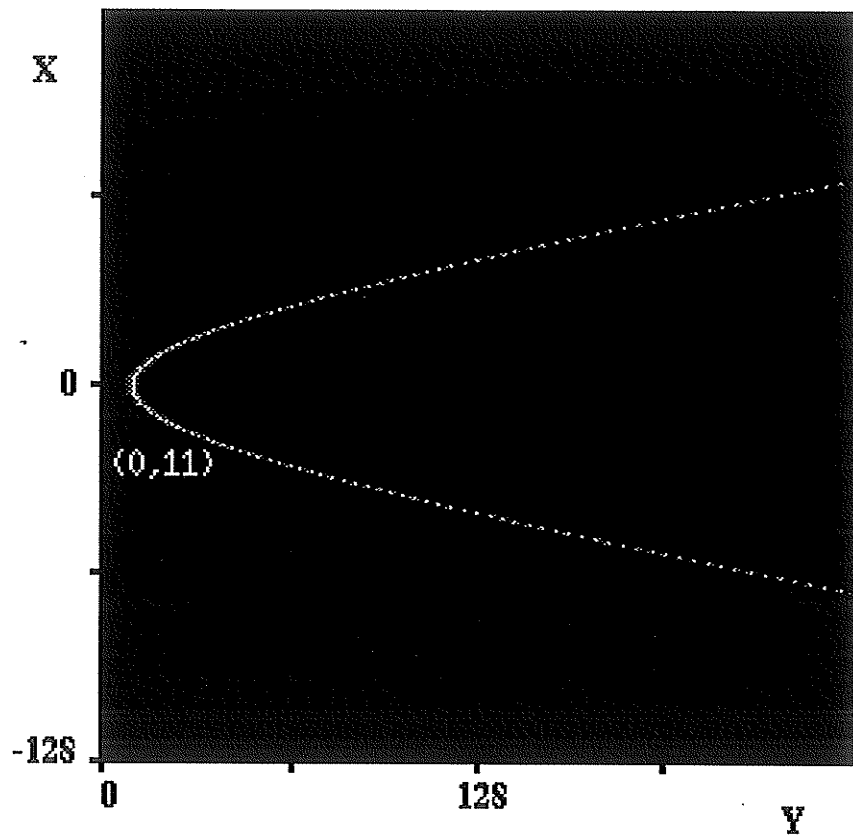


Figure 6.13: Model test for correlation through the Radon transform: reference template.

through the Radon transform is shown in Figure 6.14. The coordinates of two bright spots indicate exactly the distance between the two hyperbolas of the original image (Figure 6.12) and the reference template (Figure 6.13). Each of two bright spots is located at the crossing point of two dim straight lines which are in fact asymptotes to the hyperbola. In summary, coordinates of the apexes can be determined by locating the bright points (or dark point if original value is low DN-value) at the crossing point of two dim asymptotes.

Correlation using the Radon transform approach was applied to the airborne C-band SAR data from the Wekusko Lake area, Manitoba Canada (Figure 6.15). The topography of this area is characterized by the very low relief typical of the Canadian shield, which results in an SAR image with very low radar shadow. Several fold structures are visible, however, due to changes in terrain slope especially in the bottom half of the image (Figure 6.15). Parts of lake shorelines which are parallel or subparallel to azimuth are expressed by high brightness, whereas many fold structures are expressed by darker tone. In Figure 6.15, the squares annotated by "A", "B", and "C" include apexes of visible fold structures. To locate apexes of fold structures, a reference hyperbola is selected which is represented by a equation $y = 4.5\sqrt{x^2 + (33)^3} - 145$ (Figure 6.16). The selection of the reference hyperbola is based on the shape analysis of the fold whose apex is located at "A".

Correlation using the Fourier transform was tested first, with the result shown in Figure 6.17. The correlation through FFT was carried out after zeros were padded to the original data in both x - and y -dimension. No

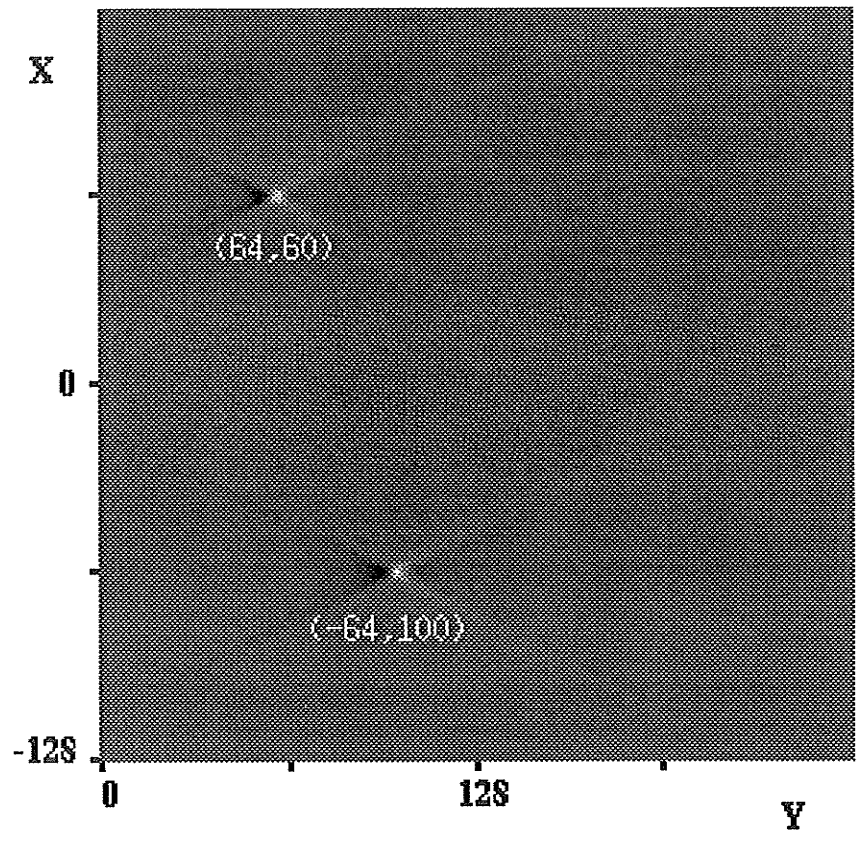


Figure 6.14: Model test for correlation through the Radon transform: output.

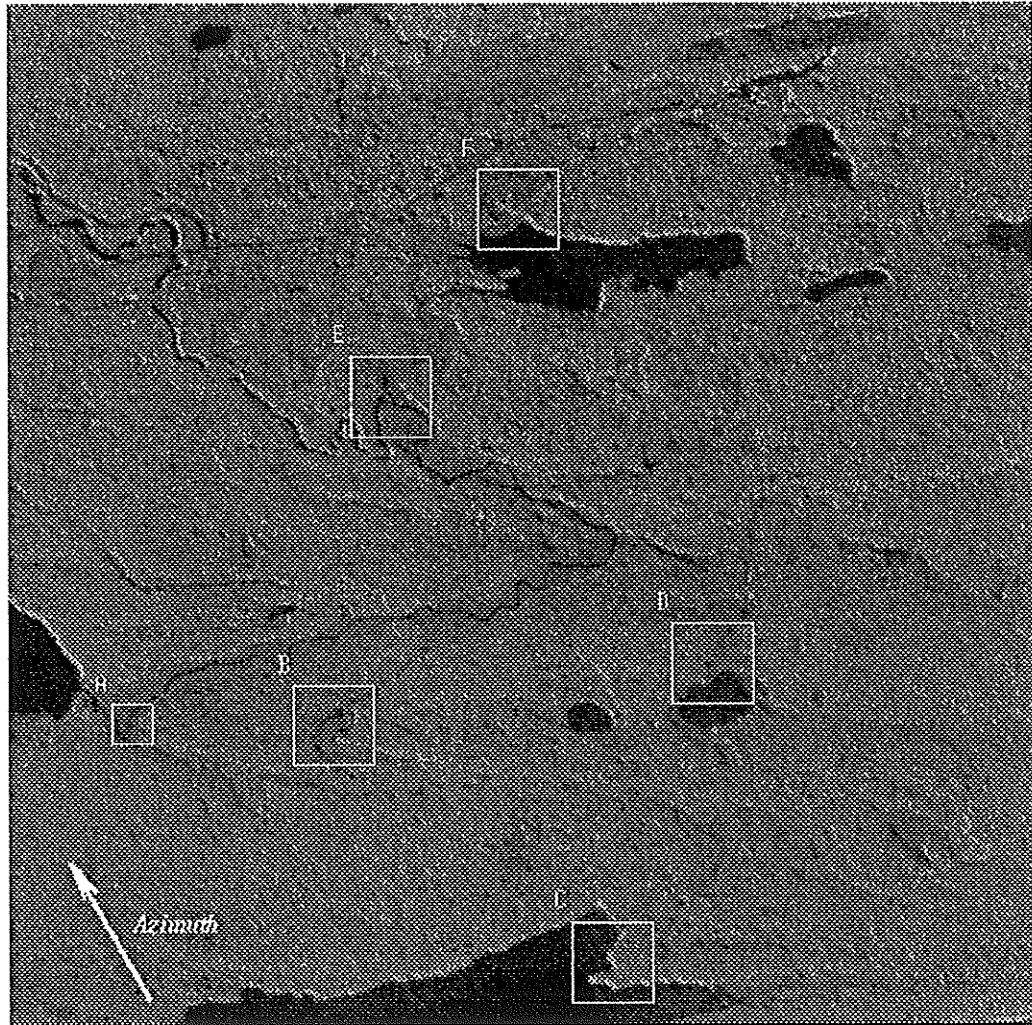


Figure 6.15: Airborne C-band SAR data from the Wekusko Lake area, Manitoba Canada: the squares annotated by “A”, “B”, and “C” correspond to the location of discernible fold apexes; “D”, “E”, and “F” correspond to fold-like structures.

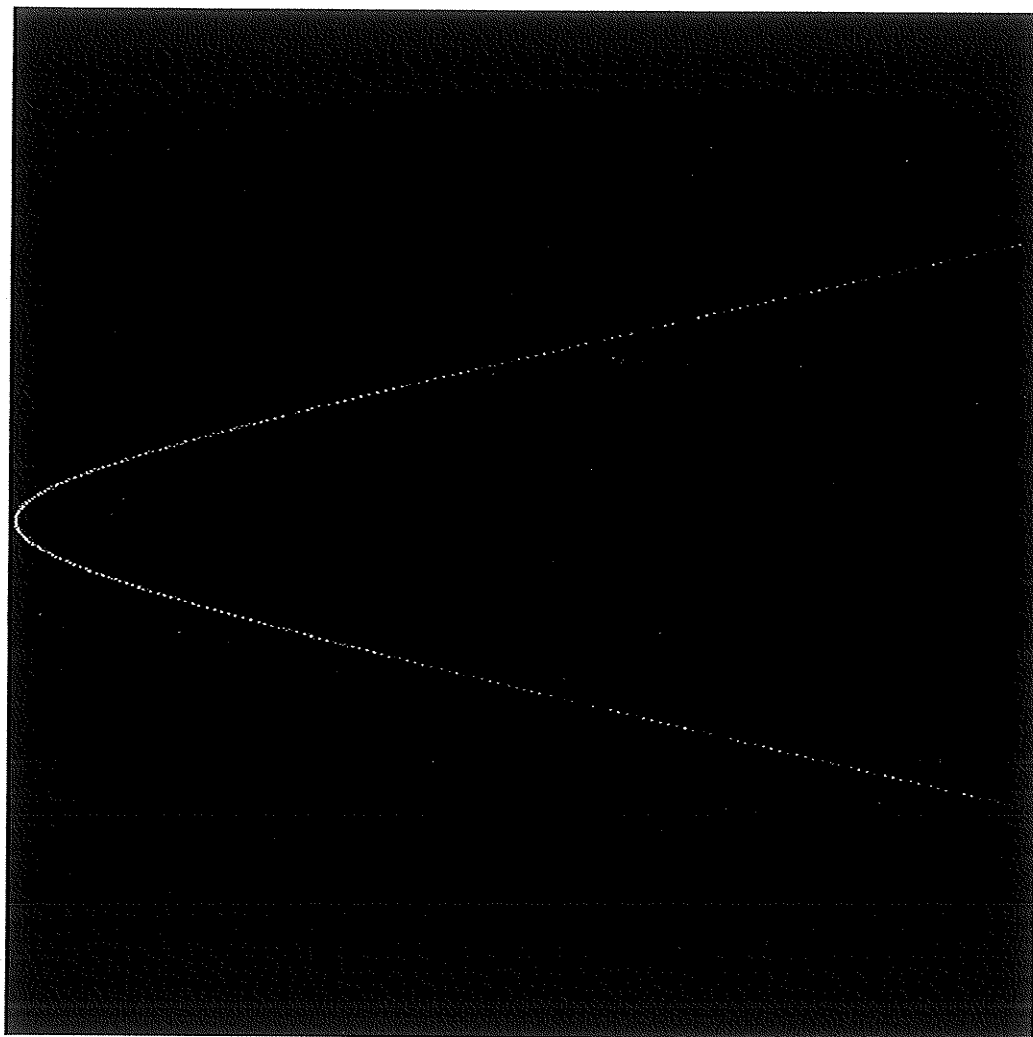


Figure 6.16: The reference hyperbola for correlation.

distinct points can be discerned in Figure 6.17 except for subtle changes in brightness. Low DN-values of fold structures and low tonal contrast of fold structures with adjacent fields in the image may be responsible for this poor result.

Correlation using the Radon transform was tested with the same data as used above. The correlation process, a simple shifting processes in z -dimension as previously explained, was performed after screening in the Radon space. The screening process in the Radon space detects a certain level of amplitude of the Radon transformed values and replaces them with a specified values. Most bright lines in the test SAR image (Figure 6.15) are shorelines parallel or subparallel to azimuth. Thus, one can expect that the high amplitudes of the Radon transform are contributions from these bright shorelines.

Fold structures which are main targets to be located are expressed by low DN-values. For the reason, the high amplitude of the Radon transform signature are not useful for this specific purpose. The screening process adopted is as follows:

- 1) find the maximum amplitude of the Radon transform and multiply it by a weighting factor (0.8 in this test) to make a ceiling value,
- 2) keep the amplitude if it is less than the ceiling value estimated by 1),
or
- 3) replace the amplitude by the ceiling value if the amplitude is higher than this level.

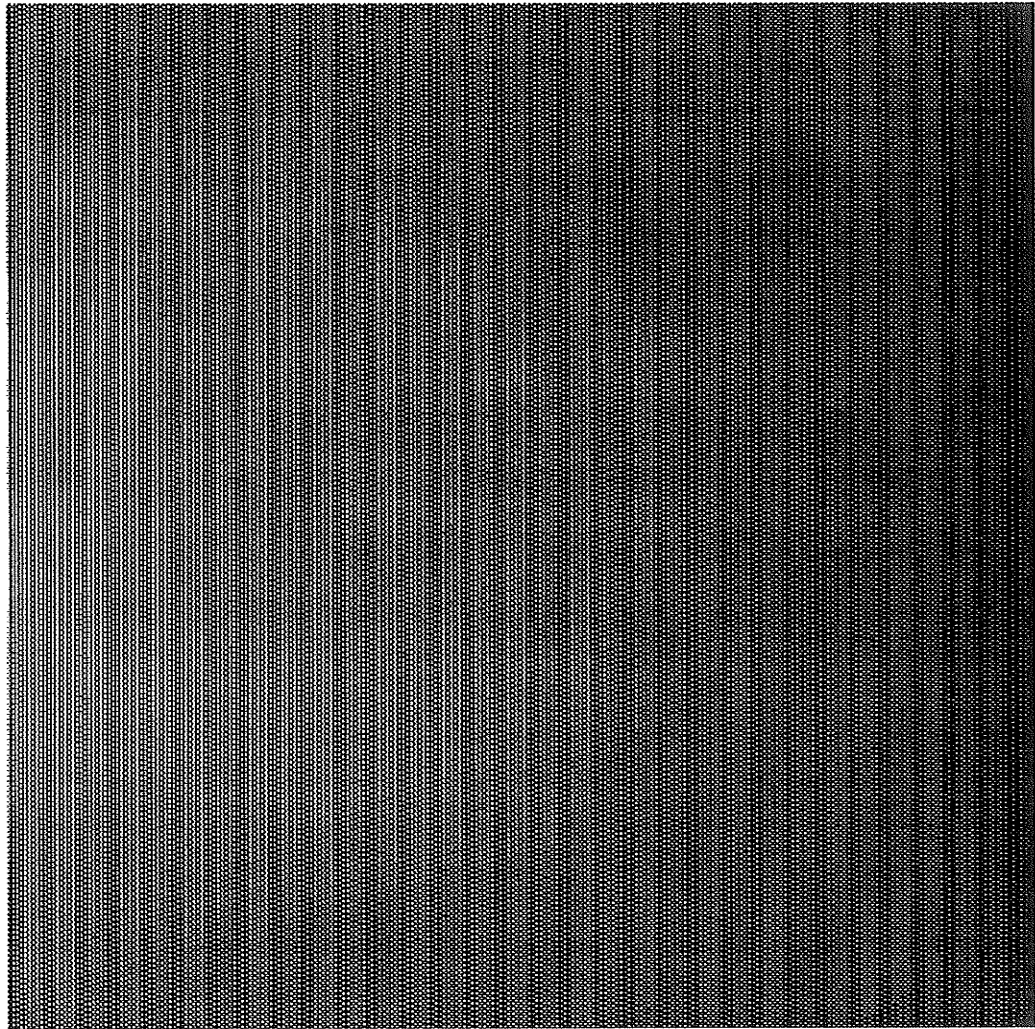


Figure 6.17: Correlation output through the Fourier transform approach.

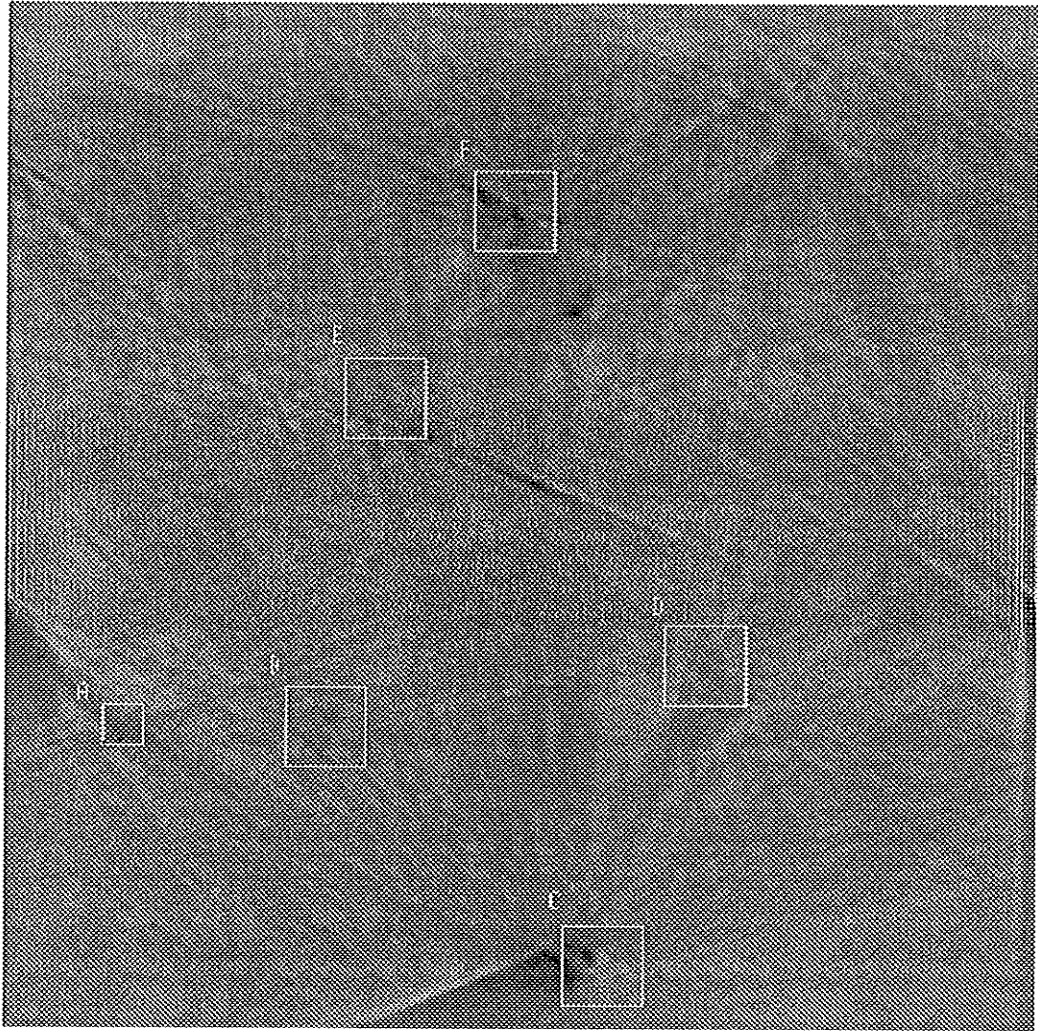


Figure 6.18: Correlation output through the Radon transform approach with superposition of squares from Figure 6.15.

The result of the correlation through the Radon transform is shown in Figure 6.18, and is remarkably different from that shown in Figure 6.17. In Figure 6.18, there are many dark spots with crossing asymptotes from the reference hyperbola. The squares in Figure 6.18 are superimposed from Figure 6.15. Dark spot in the area "A" is easily detectable in Figure 6.18 and it corresponds to apex of a fold ("A" in Figure 6.15). Dark spots in the area "B" and "C" are not as clear as the area "A" in Figure 6.18 and interpretation are questionable. There are some difficulties in determining geological interpretation of area "D", "E", and "F", which are more clearly detectable than "B" and "C", but they may not represent true fold structures.

In summary, the correlation approach through the Radon transform is not yet fully applicable for locating certain geological structures on SAR image data. However, the result of this approach is very promising as an alternative to the Fourier transform approach especially when correlation is combined with a screening process in the Radon transform space.

6.3 Merging of Multiple SAR Image Data Sets

6.3.1 Introduction

Since the first public orbital SAR mission on Seasat, a number of digital image processings of SAR data have been carried out to enhance geologic structure (e.g. Masuoka *et al.* [75], Lowman *et al.* [66], Curlis *et al.* [20], Hirose and Harris [42], Daily [24]). Masuoka *et al.* [75] in particular has tested various digital SAR image enhancement techniques using SIR-B and Seasat data over Canadian Shield. Lowman *et al.* [66] also investigated SIR-B and Seasat SAR imagery over the Canadian Shield test sites, and addressed the SAR look direction biasing (or azimuth illumination biasing) problem. The radar look direction bias is severe especially at linear ridges and valleys that are uniformly rough relative to radar wavelength, because incidence angle will be similar and there will be no inherent backscatter contrast (Lowman *et al.* [66]). It was suggested that at least two data sets of different look direction be mandatory for geologic interpretation of SAR data (Lowman *et al.* [66]).

The following work is focused on the topic of merging two or more SAR data sets to reduce the radar look direction biasing, and enhancement of geologic features in the merged image. Three approaches are investigated and tested using C-band airborne SAR data and ERS-1 SAR data from the Sudbury Basin test area. They include:

- 1) simple addition or subtraction,

- 2) directional derivative followed by simple subtraction, and
- 3) principal components analysis (PCA) approach.

6.3.2 Digital Image Addition and Subtraction

One of the simplest approaches to combine two SAR data sets is pixel by pixel addition or subtraction of digital image data. The added images were reported to retain both topographic and geologic features when Seasat and SIR-B SAR data were combined for a low relief Canadian Shield area (Lowman *et al.* [66]).

A general equation of the addition process can be written as

$$DN_{new} = a \cdot DN_A + b \cdot DN_B \quad (6.14)$$

where a and b are weighting factors and are positive constants.

In this study, tests for digital image addition are carried out using C-band airborne and ERS-1 SAR data over the Sudbury Basin test area shown in Figures 6.5 and 6.6, respectively. Two resulting additive images are shown in Figure 6.19 and 6.20. The first one in Figure 6.19 was generated by a direct addition (i.e. $a = 1.0$ and $b = 1.0$ in Eq.(6.14)), and the second one in Figure 6.20 used $a = 0.75$ and $b = 0.75$. In this test of additive image, the relative weighting case (i.e. different a and b) has not been included because optimal weighting factors of a and b can be achieved by the principal component analysis.

The digital image DN-values are always positive, consequently the addition results in brighter tone than the original images in general. Specifically,

in Figure 6.19 which is a direct addition with unit weighting factors, details of many small geologic features have disappeared because of the many scattered bright spots. In Figure 6.20 where the weighting factors were $a = 0.75$ and $b = 0.75$, large surface geologic features of the North Range (northwest parts in the image) are retained, and both *NWW*-trending lineaments of airborne SAR data and *NNW*-trending lineaments of ERS-1 SAR data are relatively well visible. Geologic features inside the Sudbury Basin structure are blurred when compared with the original airborne data in Figure 6.5. Northeast trending linear features along the North Range are also hardly visible.

Instead of additive process, two SAR data sets can be combined through a subtraction. The following subtractive operation used is:

$$DN_{new} = DN_A + a \cdot (DN_A - DN_B) \quad (6.15)$$

where a is a constant factor. Two subtractive images were generated by using a factor $a = 0.5$ (Figure 6.21) and $a = 0.4$ (Figure 6.22) using two original airborne and ERS-1 SAR data sets. In a similar manner to the additive images shown in Figure 6.20, geologic features in the North Range have retained characteristics of both airborne (*NWW*-trending lineaments) and ERS-1 (*NNW*-trending lineaments) SAR data. Features inside the low relief Sudbury Basin area are less clear than in the original airborne SAR image (Figure 6.5), but are better imaged than the additive images shown in Figure 6.19 and 6.20. Northeast trending linear features along the North Range are not so distinct as the original SAR data in Figures 6.5 and 6.6.



Figure 6.19: Additive images with factors $a = 1.0$ and $b = 1.0$.



Figure 6.20: Additive images with factors $a = 0.75$ and $b = 0.75$.



Figure 6.21: Subtractive images with factors $a = 0.5$.

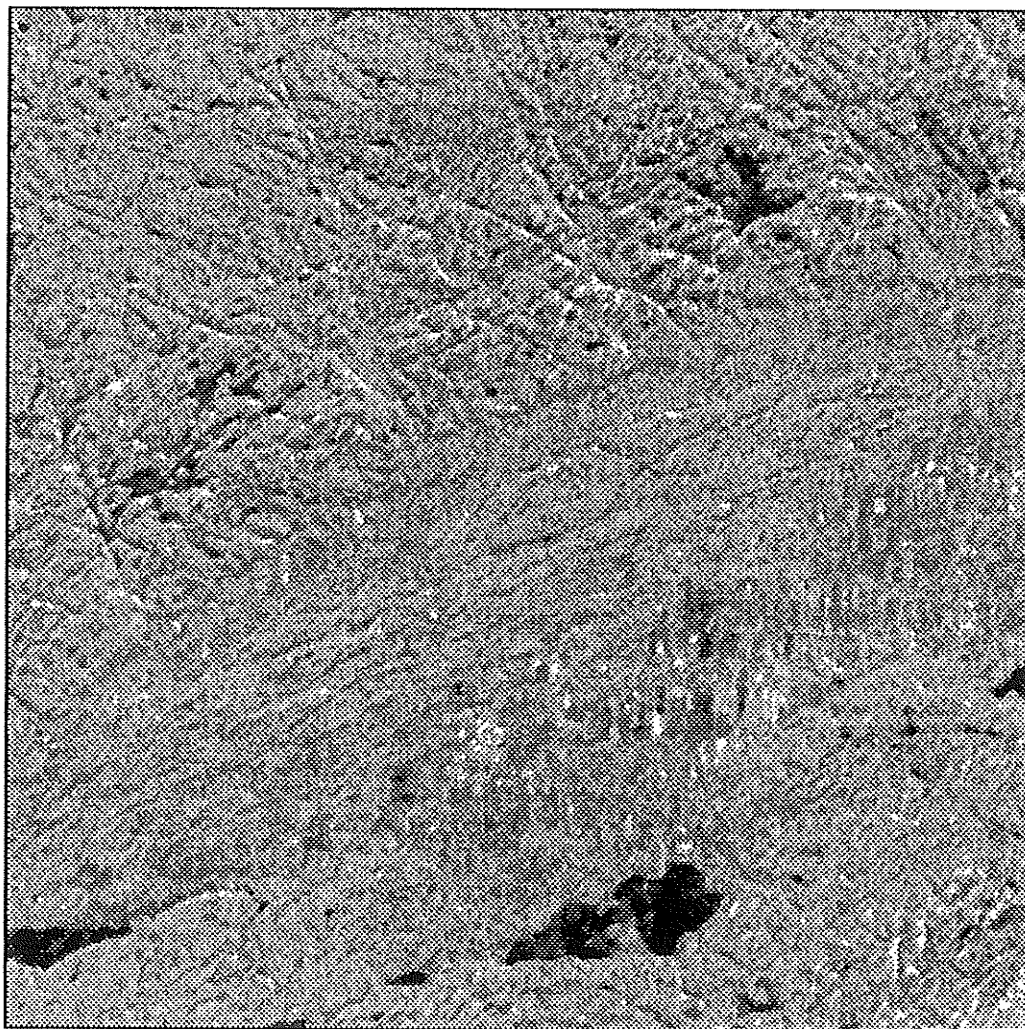


Figure 6.22: Subtractive images with factors $a = 0.4$.

In summary, the subtractive image merging appears to work better than the simple additive image processing in this particular example. However, neither the simple addition nor the subtraction process is very effective for preserving the original surface geologic features.

6.3.3 Directional Derivative Approach

In the previous section, merging of two SAR data sets using simple addition or subtraction resulted in loss of certain geologic features. In both case, enhancement of specific features prior to merging is required. The directional derivative method is very effective in enhancing linear features of remote sensed data in a selected direction (Masuoka *et al.* [75], Harding [39], Moore and Waltz [82]). Moore and Waltz [82] suggested a general approach to lineament enhancement on Landsat TM data. Masuoka *et al.* [75] investigated a variety of lineament enhancing filters suitable specifically for SAR data, and concluded that a Prewitt edge mask was most useful but suggested a slight modification for SAR data from that used by Moore and Waltz [82]. A remaining question is then how the direction to be enhanced can be determined. One simple approach is the visual inspection of the SAR image data to select the direction. The radar look direction may be an alternative because surface geologic structures parallel to the radar look direction are generally poorly imaged in SAR data unless roughness contrasts compensate.

A method described in this section is an approach utilizing the Radon transform analysis discussed in Section 6.2.2. The following processing steps for the directional derivative and merging are implemented:

- (1) select a direction to be enhanced using the Radon transform analysis.
- (2) directional derivative processing using a 3×3 convolution window (Figure 6.23) developed by Haralick [37].
- (3) add directional components of step (2) to the original digital SAR data.
- (4) generate a subtractive image with the other SAR data.

SAR data sets used are again the CCRS's airborne C-band and the ERS-1 SAR data from the Sudbury Basin test site (Figure 6.5 and 6.6). Plots of the maximum amplitude of the Radon transform versus slope are shown in Figures 6.10 (a) and (b), and 6.11.

One class of important surface geologic feature in this test site is the northeast trending linear features in the North Range (Figure 6.7). These were highlighted in neither the additive image (Figure 6.20) nor the subtractive images (Figure 6.21 and 6.22). Strikes of these linear features were estimated to be the range from $+43^\circ$ to $+50^\circ$ using the Radon transform analysis. In this range, the amplitude of Radon transform of both original CCRS's airborne and ERS-1 SAR data show relatively high amplitude (Figure 6.11). Directional components were estimated first using ERS-1 data with $\theta = +47^\circ$ for the convolution mask shown in Figure 6.23. A subtractive image with weighting $a = 0.4$ (Eq.(6.15)) in Figure 6.24 is then produced using the original SAR data and the lineament enhanced ERS-1 data through the directional derivatives. Comparing Figure 6.24 with simple additive or subtractive images of Figure 6.20, 6.21, and 6.22, the *NE*-trending geological linear features are well enhanced. In addition, *NNW*-trending lineaments in

$$\cos \theta * \begin{array}{|c|c|c|} \hline -1 & 0 & 1 \\ \hline -1 & 0 & 1 \\ \hline -1 & 0 & 1 \\ \hline \end{array} + \sin \theta * \begin{array}{|c|c|c|} \hline 1 & 1 & 1 \\ \hline 0 & 0 & 0 \\ \hline -1 & -1 & -1 \\ \hline \end{array}$$

Figure 6.23: Directional derivative convolution mask (Haralick 1984).

the North Range, which are characteristic features in the ERS-1 SAR data, are also well expressed and enhanced relative to the original airborne SAR data shown in Figure 6.5. Small structures in the south-eastern parts of the image where there is an area of relatively low relief are deteriorated to some extent by many speckle noise-like bright spots.

Another image in Figure 6.25 is obtained through the same steps used to generate the images in Figure 6.24 but with $\theta = -26^\circ$. This is the strike estimated using Radon transform analysis of the ERS-1 SAR data (Figures 6.10 (b) and 6.11) for distinct linear features. The image shown in Figure 6.25 enhanced *NW*- to *NNW*-trending lineaments relative to the results shown in Figure 6.24. Geologic structures inside the Sudbury Basin, however, are less than in the original airborne C-band SAR data.

Further investigations are required to reduce speckles and the other artifacts introduced by the directional derivative process. However, a combined processing of directional derivative and digital subtraction is effective approaches for merging to reduce radar look direction bias relative to simple addition or subtraction. The Radon transform analysis has proven to be very effective for selecting linear edge directions for enhancement.

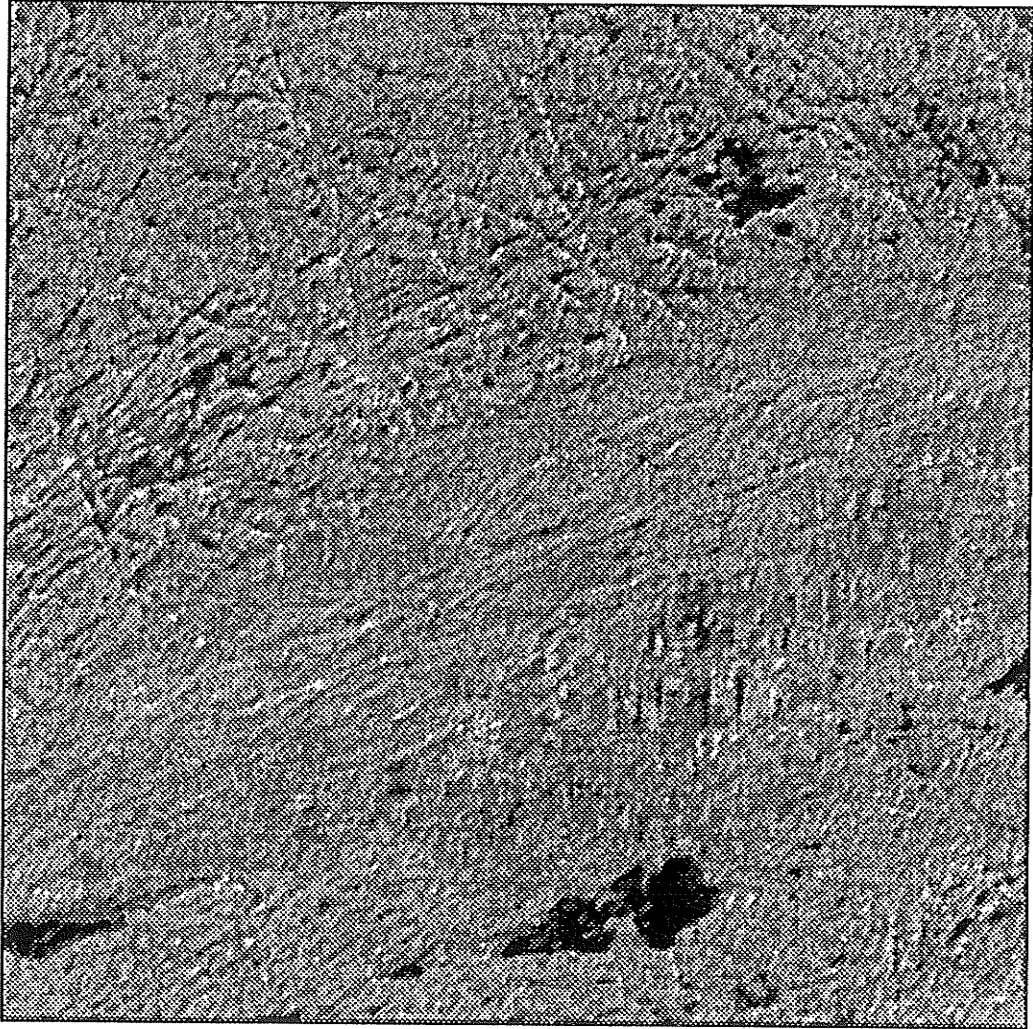


Figure 6.24: Image obtained through directional derivative process ($\theta = +43^\circ$).

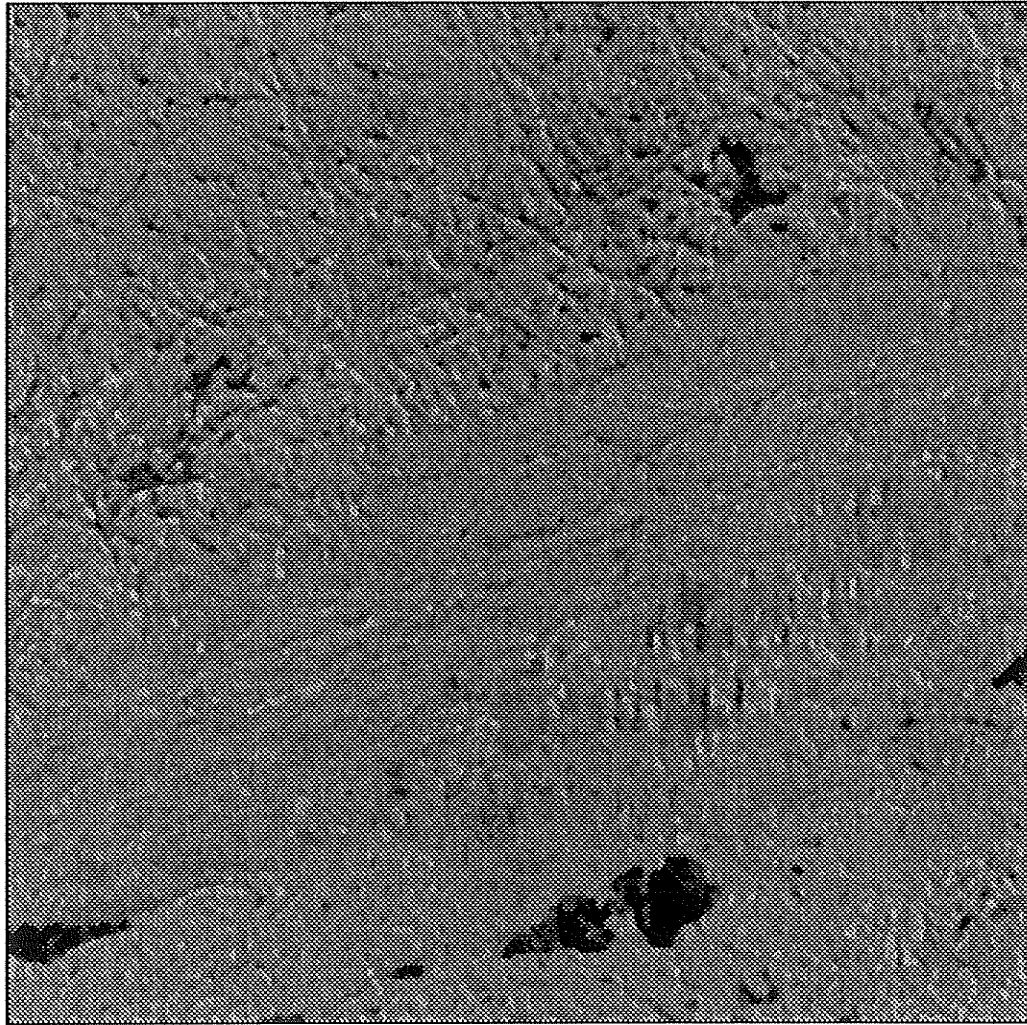


Figure 6.25: Image obtained through directional derivative process ($\theta = -26^\circ$).

6.3.4 Principal Components Analysis

The principal components analysis (PCA), also referred as Karhunen-Loève transform, is a very useful technique for the analysis of correlated multiple data sets. The PCA is widely used in digital remote sensing to compress the dimensionality of multispectral data sets by projecting data to an eigen space with the objective of optimally reducing redundancy (e.g. Jensen [51]). Moon *et al.* [79] tested the PCA approach with SPOT data, and showed that it was very effective in the classification of surface geological features. Masuoka *et al.* [75] carried out a similar PCA study with three SAR data sets.

For multiple data sets, the DN-values are often highly correlated with each other. The mutual relations of DN-values between two data sets can be measured by covariance matrix. Covariance matrix is defined by the joint variance of DN-values about common mean of two data sets (Jensen [51]). Correlation coefficient is the ratio of the covariance of two data sets to the product of their standard deviations. Using a covariance matrix of the multispectral data set, a new coordinate system can be defined so that the first axis (or first principal component) is aligned to the direction associated with the maximum variance. The second principal component is then orthogonal to the first principal component and associated with the remaining maximum variance. The following principal components are defined in a similar manner to the second principal component. Thus, projecting highly correlated original data sets to the principal components results in new uncorrelated multiple data sets. The first principal component is associated with the

direction of the maximum amount of variance, and thus the first principal component image is dominated by most highly correlated features in all of original data sets.

The problem examined here is how to merge SAR data sets to reduce the radar look direction bias, and consequently enhance the geologic lineament features through the PCA processing. The PCA test was first carried out with two data sets: the original airborne SAR data in Figure 6.5 and the original ERS-1 SAR data in Figure 6.6. The resulting image of the first principal components (the largest eigen value) is shown in Figure 6.26. Correlation statistics of the PCA processing of the two SAR data sets are given in Table 6.2, and the eigen values and eigen vectors are listed in Table 6.3. The correlation coefficient of the two data sets is very low, 0.16, as given in Table 6.2. The first component contains 58.5 percent of the variance. Although certain lineaments are enhanced, details of the interior basin are not well visible. The resulting image in Figure 6.26 is not much better than the simple additive image shown in Figure 6.20. This result can be explained by low correlation between two SAR data sets. In this case, auxiliary data sets are required to improve the first principal component image.

The second PCA experiment are carried out using three data sets: the CCRS's airborne SAR data (Figure 6.5), the ERS-1 SAR data (Figure 6.6), and lineament-enhanced data set obtained through the directional derivative process (Figure 6.24). Correlation statistics and the eigen vectors of three data sets are given in Tables 6.4 and 6.5.

The first principal component image is shown in Figure 6.27, and shows

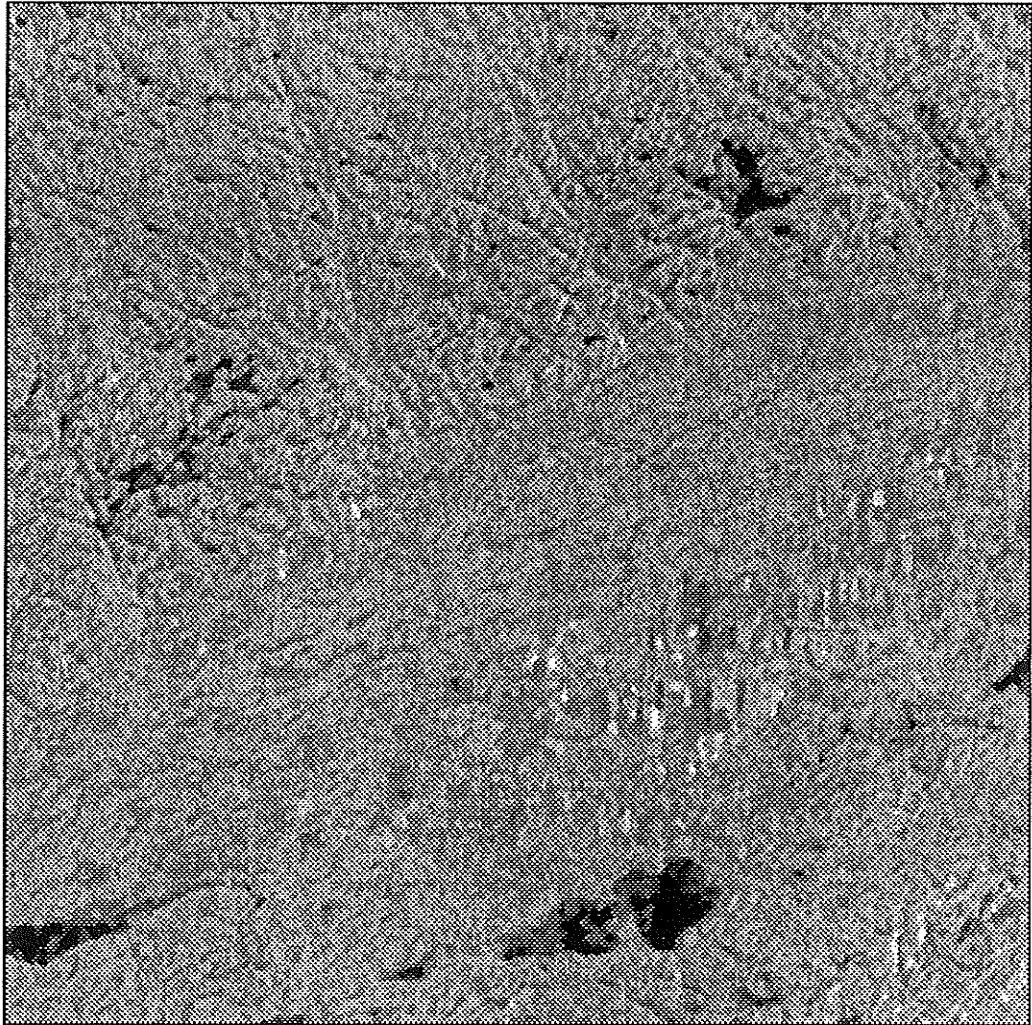


Figure 6.26: The PCA first component image of two data sets.

Table 6.2: Correlation coefficient of the CCRS's airborne and the ERS-1 SAR data: Band 1 is the airborne SAR data, and Band 2 is the ERS-1 SAR data.

Band	1	2
1	1.00	
2	0.16	1.00

Table 6.3: Eigen values and eigen vectors of two components.

Eigen value	Eigen value (%)	X1	X2
1176.29	58.45	0.56	0.83
836.15	41.55	-0.83	0.56

details of the surface geologic features extremely well. All three types of lineaments in the North Range, which include *NNW*-trending lineaments, *NWW*-trending lineaments, and *NE*-trending lineaments, are enhanced as are the small structures inside the basin.

The Radon transform analysis are again carried out to evaluate the enhanced lineaments, and the resulting plot of maximum amplitude versus slope in degree is shown in Figure 6.28 (solid line). The Radon transform analysis of the original airborne SAR data (Figure 6.10 (a)) is also plotted (dotted line) using the same scale to compare with that of the PCA image. The plot in Figure 6.28 shows the enhanced lineaments in the PCA image (solid line) at -16° and -26° compared with the plot of the original airborne SAR data (dotted line). It also shows that other characteristic amplitude peaks

Table 6.4: Correlation coefficient of three data sets: Band 1 is the CCRS's airborne SAR data, Band 2 is the ERS-1 SAR data, and Band 3 is linement enhanced data.

Band	1	2	3
1	1.00		
2	0.16	1.00	
3	0.74	0.40	1.00

Table 6.5: Eigen values and eigen vectors of three components.

Eigen value	Eigen value (%)	X1	X2	X3
2378.47	66.91	0.52	0.36	0.77
913.45	25.70	-0.41	0.90	-0.15
262.92	7.40	-0.75	-0.24	0.62

at -75° , -46° , and the amplitude high in the range from $+43^\circ$ to $+50^\circ$ are all retained in the PCA image.

In summary, the PCA approach appears to be one of most effective method for merging multiple SAR data sets, and it retains the characteristics of each original SAR data set remarkably. However, the PCA image obtained from only the two original SAR data sets did not improve much from the simple additive approach due to low correlation between the two original SAR data sets. In that case, at least one more additional data set is required to effectively enhance lineaments in the resulting PCA image. In this study, an additional data set obtained through a directional derivative processing was used, and the resulting PCA first component image enhanced



Figure 6.27: The PCA first component image of three data sets.

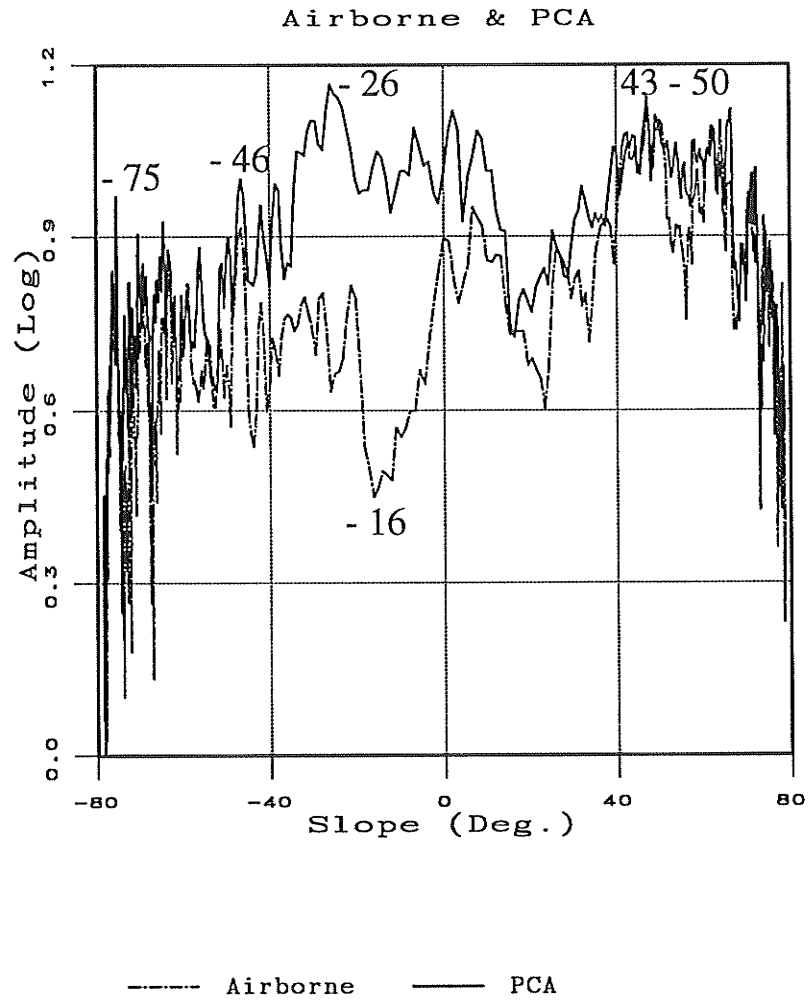


Figure 6.28: Maximum amplitude of the Radon transform versus slope: solid line represents the PCA image, and dotted line represents the original airborne SAR data.

the geological surface lineament features while it retains many small detailed structures.

Chapter 7

Conclusions

A SAR inversion formula for surface scattered SAR data in the f - k domain has been established in this thesis based on the Born (first) approximation concept. The development has been focused on the initial formulation and numerical implementation. The incident field as well as the backscattered field are included in this approach. The wavefield spreading factor is kept through the formulation. To be specific, the spreading factor of the incident field as well as the backscattered field are included by introducing frequency derivatives. The resulting inversion developed in this thesis theoretically provides an efficient alternative and straightforward basis for the f - k domain SAR signal processing.

To support the theoretical development of the inversion of SAR data, simulations for both airborne and spaceborne SAR systems were carried out. The simulation results demonstrate that the azimuth compression capability of the new inversion algorithm, along with the accommodation of range curvature, is very effective for both airborne and spaceborne cases. Another distinguishing advantage over the conventional approach is that the complex

backscattering coefficient can be determined, if desired. Simulation results are presented to demonstrate that phase information of the scatterers can be precisely determined by the new inversion method.

The results of an experiment using actual airborne SAR data set acquired by the CCRS, in the nadir mode, turned out to be slightly underfocused. The poor performance is partly due to ad hoc estimation of system parameters during the processing and partly due to the inherent problem of airborne nadir mode operating geometry. Despite the initial underfocusing problem, further focusing processes, incorporated with the inversion processing, produce a well-focused final SAR image.

Although the theoretical derivation of the f - k domain inversion is now completed, certain details of the numerical implementation of the approach are yet to be assessed quantitatively. More detailed theoretical review and quantitative experiments using satellite-borne SAR data are needed to verify that the new approach extracts the complex backscattering coefficient properly.

Various techniques of SAR image enhancement for geological application have also been investigated and tested.

In determination of the dominant lineament trends, the plot of the maximum amplitude of Radon transform versus slope is found to be very useful. The radar look direction bias can also be analyzed using this plot. Two dimensional correlation using the Radon transform is also reviewed, and it is found that the Radon transform of two-dimensional correlation (or convolution) becomes one-dimensional correlation (or convolution). Experiments

to locate geologic structure of specified shape using this technique have not proven successful. However, this method has demonstrated that this new approach, with a suitable screening process in the Radon transformed space, can be as effective as the fast Fourier transform approach.

Three approaches for merging of two or more SAR data sets have been investigated and tested in this thesis. Simple addition or subtraction reduced radar look direction bias to some extent but blurred certain small geologic features. The combined processing of directional derivative and simple subtraction is effective relative to the simple addition or subtraction. The Radon transform analysis can be utilized to select the direction of linear feature to be enhanced by directional derivative. The PCA approach is the most effective among the three approaches tested. The first principal component image enhances the geological linear features while retaining small structural details. Three data sets are at least required to effectively enhance lineaments using the PCA approach. If only two sets of SAR image data are available for bias reduction, and if correlation between these two original data sets is very low, at least one auxiliary data set is required.

Appendices

A. Derivation of Forward Formula

Eq.(4.29) can be derived from Eq.(4.28) as follows. The Fourier transform of $\Theta(x_0; \omega)$ in Eq.(4.28) with respect to x_0 is

$$\Theta(k_x; \omega) \sim \frac{2\omega}{8\pi^2 c^2} \iint_B i\pi \sigma_n^o(\mathbf{r}) e^{-ik_x x} \cdot H_0^{(2)} \left(\sqrt{y^2 + z_0^2} \cdot \sqrt{4\frac{\omega^2}{c^2} - k_x^2} \right) dx dy \quad (\text{A..1})$$

where $H_0^{(2)}(\cdot)$ is the Hankel function of second kind (Magnus and Oberhettinger [71]). Now let us change the (y, z_0) coordinate into the slant-range coordinate $\eta = \sqrt{y^2 + z_0^2}$, then we have

$$\Theta(k_x; \omega) \sim \frac{2\omega}{8\pi^2 c^2} \iint_B \sigma_n^o(x, \eta) \frac{i\pi \eta}{\sqrt{\eta^2 - z_0^2}} H_0^{(2)}(\eta k_\eta) e^{-ik_x x} dx d\eta \quad (\text{A..2})$$

where k_η is as defined by Eq.(4.31) in Section 4.4. The argument of Hankel function (ηk_η) is much larger than unity because the minimum slant-range η is at least several kilometers and k_η is always positive value as discussed in section 3. Thus, the Hankel function can be replaced by its asymptotic formula given

$$H_0^{(2)}(\eta k_\eta) \sim \sqrt{\frac{2}{\pi \eta k_\eta}} e^{-i\eta k_\eta + i\pi/4} \quad (\text{A..3})$$

(Olver [86]).

Substituting Eq.(A..3) into Eq.(A..2), we have

$$\Theta(k_x; \omega) \sim \frac{i\omega e^{i\pi/4}}{4\pi c^2} \sqrt{\frac{2}{\pi k_\eta}} \iint_B \frac{\sqrt{\eta} \sigma_n^o(x, \eta)}{\sqrt{\eta^2 - z_0^2}} e^{-i(k_x x + k_\eta \eta)} dx d\eta \quad (\text{A..4})$$

which is Eq.(4.29) in Section 4.4.

B. Derivation of Inversion Formula

The inversion formula Eq.(4.32) is derived as follows. The Eq.(4.29) in Section 4.4 can be rewritten as

$$\Theta(k_x; \omega) \sim \frac{i\omega e^{i\pi/4}}{4\pi c^2} \sqrt{\frac{2}{\pi k_\eta}} \sigma_{nc}^o(k_x, k_\eta) \quad (\text{B..1})$$

or equivalently

$$\sigma_{nc}^o(k_x, k_\eta) \sim -2\sqrt{2\pi^3} c^2 e^{i\pi/4} \frac{\sqrt{k_\eta}}{\omega} \Theta(k_x; \omega) . \quad (\text{B..2})$$

Thus the complex backscattering coefficient $\sigma_{nc}^o(x, \eta)$ can be easily obtained by taking the two-dimensional inverse Fourier transform of $\sigma_{nc}^o(k_x, k_\eta)$ with respect to k_x and k_η .

Before taking the two-dimensional inverse Fourier transform, some special conditions in processing SAR data can be considered. It is necessary to compensate for the time gap of $(2\eta_0/c)$ between the signal transmission and the first arrival by multiplying $\Theta(k_x; \omega)$ by $e^{-i2\eta_0\omega/c}$.

From Eq.(4.31) in Section 4.4, the frequency ω is

$$\omega = \omega_0 + \omega' = \frac{c}{2} \sqrt{k_x^2 + k_\eta^2} \quad (\text{B..3})$$

where ω_0 is the center frequency of the transmitted signal and ω' is a frequency width. The range of ω' is

$$-2\pi \frac{\text{A/D Rate}}{2} \leq \omega' \leq 2\pi \frac{\text{A/D Rate}}{2} .$$

After multiplying Eq.(B..2) by $e^{-i2\eta_0\omega/c}$ and replacing ω by Eq.(B..3), the two-dimensional inverse Fourier transform becomes

$$\begin{aligned} \sigma_{nc}^o(x, \eta) \sim & -4\sqrt{2\pi^3} c e^{i\pi/4} \frac{1}{(2\pi)^2} \iint \frac{\sqrt{k_\eta}}{\sqrt{k_\eta^2 + k_x^2}} e^{-i\eta_0\sqrt{k_\eta^2 + k_x^2}} \\ & \Theta\left(k_x, \frac{c}{2}\sqrt{k_\eta^2 + k_x^2}\right) e^{i(k_x x + k_\eta \eta)} dk_x dk_\eta . \end{aligned} \quad (\text{B..4})$$

Notice that the restored image $\sigma_{nc}^o(x, \eta)$ does not provide any information for less than the minimum slant-range η_0 , and therefore that the image is required to be expressed by a shift variable $\eta' = \eta - \eta_0$. The final inversion formula then becomes

$$\begin{aligned} \sigma_{nc}^o(x, \eta') \sim & -4\sqrt{2\pi^3} c e^{i\pi/4} \frac{1}{(2\pi)^2} \iint \frac{\sqrt{k_\eta}}{\sqrt{k_\eta^2 + k_x^2}} e^{i\eta_0(k_\eta - \sqrt{k_\eta^2 + k_x^2})} \\ & \Theta\left(k_x, \frac{c}{2}\sqrt{k_\eta^2 + k_x^2}\right) e^{i(k_x x + k_\eta \eta')} dk_x dk_\eta \end{aligned} \quad (\text{B..5})$$

which is Eq.(4.32) in Section 4.4.

C. Derivation using the Method of Stationary Phase

The Fourier transform of Eq.(3.51) in Section 3.2.3 with respect to the azimuth x can be obtained through the method of stationary phase as follows.

The Fourier transform of Eq.(3.51) is given as

$$s(k_x, t; \eta) = \int \delta \left(t - \frac{2}{c}\eta - \frac{x^2}{c\eta} \right) \exp \left\{ -i \frac{4\pi}{\lambda} \left(\eta + \frac{x^2}{2\eta} \right) \right\} e^{-ik_x x} dx . \quad (\text{C..1})$$

The method of stationary phase is summarized as

$$f(\xi) = \int g(x) \exp \{ i\xi\varphi(x) \} dx, \quad \xi > 0 \quad (\text{C..2})$$

$$\sim e^{i\pi/4} \left[\frac{2\pi}{\xi |\varphi''(x_0)|} \right]^{1/2} g(x_0) \exp \{ i\xi\varphi(x_0) \} \quad (\text{C..3})$$

where x_0 satisfies $\varphi'(x_0) = 0$ (Carrier *et al.* [15]).

Comparing Eq.(C..1) with Eq.(C..2), we can set

$$g(x) = \delta \left(t - \frac{2}{c}\eta - \frac{x^2}{c\eta} \right) \quad (\text{C..4})$$

$$\varphi(x) = - \left(\frac{4\pi}{\lambda}\eta + \frac{4\pi}{\lambda} \frac{x^2}{2\eta} + k_x x \right) \quad (\text{C..5})$$

$$\varphi'(x) = k_x + \frac{4\pi}{\lambda\eta} x \quad (\text{C..6})$$

$$\varphi''(x) = \frac{4\pi}{\lambda\eta} \quad (\text{C..7})$$

The x_0 satisfying $\varphi'(x_0) = 0$ is estimated from Eq.(C..6) such as

$$x_0 = -\frac{\lambda\eta}{4\pi} k_x . \quad (\text{C..8})$$

Replacing Eq.(C..3) by Eqs.(C..4) - (C..7) with $x_0 = -\lambda\eta k_x/4\pi$, we have

$$s(k_x, t; \eta) \sim \sqrt{\frac{\lambda\eta}{2}} e^{-i(4\pi\eta/\lambda - \pi/4)} \delta\left(t - \frac{2}{c}\eta - \frac{c\eta}{4} \frac{k_x^2}{\omega_0^2}\right) \exp\left\{i \frac{c\eta}{4} \frac{k_x^2}{\omega_0}\right\} \text{C..9)}$$

which is shown in Eq.(3.51).

References

- [1] Ahmed, S., Warren, H.R., Symonds, M.D., and Cox, R.P., 1990, The Radarsat system, *IEEE Trans. Geosci. Electron.*, v.28, no.4, pp.598-602.
- [2] Allan, T.D. (ed.), 1983, *Satellite Microwave Remote Sensing*, Ellis Horwood Ltd.
- [3] Attema, E.P.W., 1991, The active microve instrument on-board the ERS-1 satellite, *Proc. IEEE*, v.79, no.6, pp.791-799.
- [4] Barber, B.C., 1985, Review Article: Theory of digital imaging from orbital Synthetic-Aperture Radar, *Int. J. Remote Sensing*, v.6, no.7, pp.1009-1057.
- [5] Bamler, R., 1991, Doppler frequency estimation and Cramér-Rao bound, *IEEE Trans. Geosci. Remote Sensing*, v.GE-29, no.3, pp.385-390.
- [6] Bennett, J.R. and Cumming, I.G., 1979, Digital SAR image formation airborne and satellite results, *Proc. 13th Int'l Symp. Remote Sensing of Environment*, pp.337-360.
- [7] Bennett, J.R., Cumming, I.G., and, Robert, A.E., 1980, The digital processing of SEASAT Synthetic Aperture Radar data, *Proc. IEEE Int. Radar Conf.*, pp.168-175.
- [8] Bennett, J.R., Cumming, I.G., McConnell, P.R., Gutteridge, L., 1981, Features of a generalized digital Synthetic Aperture Radar processor, *Proc. 15th Int'l Symp. Remote Sensing of Environment*, pp.271-290.

- [9] Bernfeld, M., Cook, C.E., Paolillo, J., and Palmieri, C.A., 1964-1965, Matched filtering, pulse compression and wave design, Part I-IV, *Microwave J.*, v.7, no.10, pp.57-64, no.11., pp.81-90, no.12, pp.70-76 (1964), v.8, no.1, 73-81 (1965).
- [10] Bleistein, N., 1984, *Mathematical Methods for Wave Phenomena*, Academic Press.
- [11] Bleistein, N., Cohen, J.K., and Hagin, F.G., 1985, "Computational and Asymptotic Aspects of Velocity Inversion", *Geophysics*, v.50, pp.1253-1265.
- [12] Born, V.M., 1926 Quantenmechanik der stoßvorgänge, *Z. Physik*, v.38, pp.803-827.
- [13] Brown, W.M. and Porcello, L.J., 1969, An introduction to Synthetic Aperture Radar, *IEEE Spectrum*, September, pp.52-62. (also in the reference [56])
- [14] Brown, W.M., Houser, G.G., and Jenkins, R.E., 1973, Synthetic aperture processing with limited storage and presumming, *IEEE Trans. Aerosp. Electron. Syst.*, v.9, no.2, pp.166-176. (also in the reference [56])
- [15] Carrier, G.F., Krook, M., Pearson, C.E., 1966, *Functions of a Complex Variable*, McGraw-Hill Book Co., pp.272-275.
- [16] Cheng, G. and Coen, S., 1984, The relationship between Born inversion and migration for common-mid point stacked data: *Geophysics*, v.49, 2117-2131.
- [17] Cohen, J.K. and Bleistein, N., 1979, Velocity inversion procedure for acoustic waves, *Geophysics*, v.44, pp.1077-1085.
- [18] Cohen, J.K. and Bleistein, N., 1983, The influence of out-of-plane surface properties on unmigrated sections, *Geophysics*, v.48, 125-132.
- [19] Cook, C.E. and Bernfeld, M., 1967, *Radar Signals: An Introduction to Theory and Application*, Academic Press.

- [20] Curlis, J.D., Frost, V.S., Dellwig, L.F., 1986, Geological mapping potential of computer-enhanced images from the Shuttle Imaging Radar: Lisbon valley anticline, Utah, *Photogramm. Eng. Remote Sensing*, v.52, no.4, pp.525-532.
- [21] Curlander, J.C., 1986, Performance of the SIR-B digital image processing subsystem, *IEEE Trans. Geosci. Remote Sensing*, v.24, no.4, pp.649-652.
- [22] Curtona, L.J., Vivian, W.E., Leith, E.N., and Hall, G.O., 1961, A high resolution radar combat-surveillance system, *IRE Trans. Military Electron.*, v.5, no.2, pp.127-131. (also in the reference [56])
- [23] Curtona, L.J. and Hall, G.O., 1962, A comparison of techniques for achieving fine azimuth resolution, *IRE Trans. Military Electron.*, v.6, no.2, pp.119-121. (also in the reference [56])
- [24] Daily, M., 1983, Hue-saturation-intensity split-spectrum processing of Seasat radar imagery, *Photogramm. Eng. Remote Sensing*, v.49, no.3, pp.349-355.
- [25] Deans, S.R., 1983, *The Radon transform and some of its application*, John Wiley & Sons.
- [26] Di Cenzo, A., 1988, A new look at nonseparable synthetic aperture radar processing, *IEEE Trans. Aerosp. Electron. Syst.*, v.24, no.3, pp.218-223.
- [27] Duchossois, G., 1986, Overview and status of the ERS-1 programme, *Proc. IGARSS'86*, Zurich, pp.155-159.
- [28] Durrani, T.S., and Bisset, D., 1984, The Radon transform and its properties, *Geophysics*, v.49, no.8, pp.1180-1187.
- [29] Eklundh, J.O., 1972, A fast computer method for matrix transposing, *IEEE Trans. Computers*, v.21, no.7, pp.801-803.
- [30] Fitch, J.P., 1988, *Synthetic Aperture Radar*, Springer-Verlag.
- [31] Ford, J.P., 1980, Seasat orbital radar imagery for geologic mapping: Tennessee-Kentucky-Verginia, *AAPG Bull*, v.64, pp.2064-2094.

- [32] Franceschetti, G., Schirinzi, G., 1989, A SAR processor based on two-dimensional FFT codes, *IEEE Trans. Aerosp. Electron. Syst.*, v. 26, no.2, pp.356-365.
- [33] Fraser, D., 1979, An optimized mass storage FFT, *ACM Trans. Math. Software*, v.5, pp.500-517.
- [34] Gazdag, J., 1978, Wave equation migration with the phase-shift method, *Geophysics*, v.43, no.7, pp.1342-1351.
- [35] Goodman, J.W., 1968, *Introduction to Fourier Optics*, McGraw-Hill Book Co..
- [36] Haneveld, C.J., and Herman, G.C., 1990, A fast algorithm for the computation of Radon Transforms, *Geophy. Prospecting*, v.38, pp.853-860.
- [37] Haralick, R.M., 1984, Digital step edges from zero crossing of second directional filters, *IEEE Trans. Pattern Analy. Machine Intelligence*, v.6, pp.58-68.
- [38] Hager, R.O. 1970, *Synthetic Aperture Radar Systems, Theory and Design*, Academic Press.
- [39] Harding, A.E. and Forrest, M.D., 1989, Analysis of multiple geological datasets from the English Lake district, *IEEE Trans. Geosci. Remote Sensing*, v.27, no.6, pp.732-738.
- [40] Harris, J., 1984, Lineament mapping of central Nova Scotia using Landsat-MSS and Seasat-SAR imagery, *Proc. 9th Canadian Symp. Remote Sensing*, St. John's, pp.359-373.
- [41] Held, D.N., Brown, W.E., Freeman, A., Klein, J.D., Zebker, H., Sato, T., Miller, T., Nguyen, Q., and Lou, Y., 1988, The NASA/JPL multi-frequency, multipolarisation airborne SAR system, *Proc. IGARSS' 88*, Scotland, pp.345-349.
- [42] Hirose, T., and Harris, J., 1985, On the improvement of SAR image interpretability using spectral multi-looking and spatial filtering, *Int. Symp. Remote Sensing Environ., Second Thematic Conf, Remote Sensing Explor. Geol.*, pp.601-617.

- [43] Horn, R., 1988, E-SAR – The experimental airborne L/C-band SAR system of DFVLR, *Proc. IGARSS' 88*, Scotland, pp.1025-1027.
- [44] Hovannessian, S.A., 1980, *Introduction to Synthetic Array and Imaging Radar*, Artech House, Inc..
- [45] Hou, H.S. and Andrews, H.C., 1978, Cubic splines for image interpolation and digital filtering, *IEEE Trans. Acoust, Speech, Signal Processing*, v.22, no.6, pp.508-517.
- [46] Huneycutt, B.L., 1989, Spaceborne imaging radar–C instrument, *IEEE Trans. Geosci. Remote Sensing*, v.GE-27, no.2, pp.164-169.
- [47] Huneycutt, B.L., 1990, Innovative operating modes and techniques for the spaceborne imaging radar–C instrument, *IEEE Trans. Geosci. Remote Sensing*, v.GE-28, no.4, pp.603-608.
- [48] *IEEE Trans. Geosci. Remote Sensing*, 1986, *Special Issue on the Shuttle Imaging Radar (SIR-B)*, v.GE-24, no.4., July.
- [49] Illingworth, J. and Kittler, J., 1988, A survey of the Hough transform, *Comput. Vision Graphics Image Process.*, v.44, pp.87-116.
- [50] Jackson, J.D., 1975, *Classical Electrodynamics*, 2nd ed., John Wiley & Sons Inc..
- [51] Jensen, J.R., 1986, *Introductory Digital Image Processing: A Remote Sensing Perspective*, Prentice-Hall.
- [52] Jin, M.Y. and Wu, C., 1984, A SAR correlation algorithm which accommodates large-range migration, *IEEE Trans. Geosci. Remote Sensing*, v.GE-22, no.6, pp.592-597.
- [53] Jordan, R.L., 1980, The Seasat-A synthetic aperture radar system, *IEEE J. Ocean Eng.*, v.5, pp.154-164.
- [54] Jordan, R.L., Huneycutt, B.L., and Werner, M., 1991, The SIR-C/X-SAR synthetic aperture radar system, *Proc. IEEE*, v.79, no.6, pp.827-838.

- [55] Kirk, J.C. Jr., 1975, A discussion of digital processing in synthetic aperture radar, *IEEE Trans. Aerosp. Electron. Syst.*, v.11, no.3, pp.326-337. (also in the reference [56])
- [56] Kovaly, J.J. (ed.), 1976, *Synthetic Aperture Radar*, Artech House, Inc..
- [57] Krishnapuram, R. and Casasent, D., 1988, Hough transform projections and slices for object discrimination and distortion estimation, *Applied Optics*, v.27, no.16, pp.3451-3460.
- [58] Li, F.K., Held, D.N., Curlander, J.C., and Wu, C., 1985, Doppler parameter estimation for spaceborne synthetic aperture radars, *IEEE Trans. Geosci. Remote Sensing*, v.GE-23, no.1.
- [59] Li, F.K., and Raney, R.K. (ed.), 1991, *Special section on spaceborne radars for Earth and planetary observations*, *Proc. IEEE*, v.79, no.6, June, pp.773-880.
- [60] van de Lindt, W.J., 1977, Digital technique for generating synthetic aperture radar Images, *IBM J. Res Develop.*, Sept., pp.415-432.
- [61] Linvingstone, C.E., Gray, A.L., Hawkins, R.K., and Olsen, R.B., 1987, CCRS C-Band airborne radar: System description and test result, *Proc. 11th Canadian Symposium on Remote Sensing, Waterloo, Ontario*, June 22-25, 36 p.
- [62] Linvingstone, C.E., Gray, A.L., Hawkins, R.K., and Olsen, R.B., 1988, CCRS C/X-Band airborne synthetic aperture radar: An R and D tool for the ERS-1 time frame, *IEEE Aerosp. Electron. Syst. Magazine*, October, pp.11-16.
- [63] Lodge, D.W.S., 1983, Experience of bathymetry on SEASAT synthetic radar images: in *Satellite Microwave Remote Sensing* (T.D. Allan ed.), Ellis Horwood Ltd., pp.247-260.
- [64] Loewenthal, D., Lu, L., Roberson, R., and Sherwood, J., 1976, The wave equation applied to migration, *Geophysical Prospecting*, v.24, pp.380-399.

- [65] Loffeld, O., 1990, Doppler centeroid estimation with Kalman filters, *Proc. IGARSS'90*, Washington, pp.1309-1312.
- [66] Lowman, P.D., Jr., Harris, J., Masuoka, P.M., Singhroy, V.H., and S-laney, V.R., 1987, Shuttle imaging radar (SIR-B) investigations of the Canadian Shield: initial report, *IEEE Trans. Geosci. Remote Sensing*, v.25, no.1, pp.55-65.
- [67] Lowman, P.D., 1991, Original shape of the Sudbury structure, Canada: a study with airborne imaging radar, *Canadian J. Remote Sensing*, v.17, no.2, pp.152-161.
- [68] MacDonald, H.C., 1969, Geologic evaluation of radar imagery from Darien Province, Panama, *Modern Geol.*, v.1, pp.1-63.
- [69] Madsen, S.N., 1989, Estimating the Doppler centroid of SAR data, *IEEE Trans. Aerosp. Electron. Syst.*, v.25, no.2, pp.134-140.
- [70] Madsen, S.N., Christensen, E.L., and Dall, J., 1991, The Danish SAR system: design and initial tests, *IEEE Trans. Geosci. Electron.*, v.29, no.3, pp.417-426.
- [71] Magnus, W. and Oberhettinger, F., 1949, *Formulas and Theorems for the Functions of Mathematical Physics*, Chelsea Pub. Co., pp.118.
- [72] Marconi, G, 1922, Radio telegraphy, *Proc. IRE*, v.10, pp.237.
- [73] Marconi, D., 1982, *My Father Marconi*, Balmuir Books Pub. Co.
- [74] Martinson, L., 1975, A programmable digital processor for airborne radar, *Proc. IEEE Int. Radar Conf.*, pp.186-191.
- [75] Masuoka, P.M., Harris, J., Lowman, P.D., Jr., and Blodget, H.W., 1987, Digital processing of orbital radar data to enhance geologic structure: examples from the Canadian Shield, *Photogramm. Eng. Remote Sensing*, v.54, no.5, pp.621-632.
- [76] McCauley, J.F., Schaber, G.G., Breed, C.S., Grolier, M.J., Haynes, C.V., Issawi, B., Elachi, C., Blom, R., 1982, Subsurface valleys and geology of the eastern Sahara revealed by Shuttle radar, *Science*, v.318, pp.1004-1020.

- [77] Ministry of International Trade and Industry (MITI) and National Space Development Agency of Japan (NASDA), 1990, *Outline of The JERS-1 System*, October.
- [78] Moon, W.M., Stewart, I., Won, J.S., 1991, *Ground Reference System for Japanese Earth Resources Satellite-1 (JERS-1) with Computer Program*, Geophysics Technical Report No. 14, University of Manitoba.
- [79] Moon, W.M., Won, J.S., Li, B., Slaney, V. R., and Lamontagne, M., 1991, Application of Airborne C-SAR and SPOT image Data to the Geological Setting of The Nahanni Earthquake Area, *Canadian J. Remote Sensing*, v.17, no.3, pp.272-278.
- [80] Moore, R.K., 1983, Radar fundamentals and scatterometers: *Manual of Remote Sensing*, 2nd ed. (R.N. Colwell ed.), American Society of Photogrammetry, pp.369-427.
- [81] Moore, R.K., 1983, Imaging radar systems: *Manual of Remote Sensing*, 2nd ed. (R.N. Colwell ed.), American Society of Photogrammetry, pp.429-474.
- [82] Moore, G.K, and Waltz, F.A., 1983, Objective Procedures for lineament enhancement and extraction, *Photogramm. Eng. Remote Sensing*, v.49, no.5, pp.641-647.
- [83] Moreira, J.R., 1990, A new method of aircraft motion error extraction from radar raw data for real time motion compensation, *IEEE Trans. Geosci. Remote Sensing*, v.28, no.4, pp.620-626.
- [84] Murphy, L.M., 1986, Linear feature detection and enhancement in noisy images via the Radon transform, *Pattern Recog.*, v.4, pp.279-284.
- [85] Nemoto, Y., Nishino, H., Ono, M., Mizutamari, H., Nishikawa, K., and Tanaka, K., 1991, Japanese Earth resources satellite-1 synthetic aperture radar, *Proc. IEEE*, v.79., no.6, pp.800-809.
- [86] Olver, F.W.J., 1974, *Introduction to Asymptotics and Special Function*, Academic Press, pp.237-241.

- [87] Pye, E.G., Naldrett, A.J., and Giblin, P.E. (Eds), 1984, *The Geology and Ore Deposits of the Sudbury Structure, Ontario Geological Survey Special Volume 1*, Ministry of Natural Resources, Ontario.
- [88] Radon, J., 1917, Über die bestimmung von funktionen durch ihre integralwerte langs gewisser mannigfaltigkeiten, *Berichte Sächsische Akademie der Wissenschaften*, v.69, pp.262-277.
- [89] Raney, R.K., 1984, Conceptual design of satellite SAR, *Proc. IGARSS'84*, Strasbourg, pp.801-807.
- [90] Raney, R.K., 1986, Doppler properties of radars in circular orbits, *Int. J. Remote Sensing*, v.7, no.9, pp.1153-1162.
- [91] Raney, R.K., 1987, A comment on Doppler FM Rate, *Int. J. Remote Sensing*, v.8, no.7, pp.1091-1092.
- [92] Raney, R.K., and Vachon, P.W., 1989, A phase preserving SAR processor, *Proc. IGARSS'89*, Vancouver, v.4, pp.2588-2591.
- [93] Raney, R.K., Luscombe, A.P., Langham, E.J., and Ahmed, S., 1991, RADARSAT, *Proc. IEEE*, v.79, no.6, pp.839-849.
- [94] Rey, M.T., Tunaley, J.K., Folinsbee, J.T., Jahans, P.A., Dixon, J.A., and Vant, M.R., 1990, Application of Radon transform techniques to wake detection in Seasat-A SAR image, *IEEE Trans. Geosci. Remote Sensing*, v.28, no.4, pp.553-560.
- [95] Rinenour, L.N., 1947, *Radar System Engineering: MIT Radaation Laboratory Series*, Vol.I, McGraw-Hill.
- [96] Rocca, F., Cafforio, C., and Prati, C., 1989, Synthetic aperture radar: A New application for wave equation techniques, *Geophysical Prosepecting*, v.37, pp.809-830.
- [97] Rosenbaum, J.H. and Bourdeaux, G.F., 1981, Rapid convergence of some seismic processing algorithms, *Geophysics*, v.46, pp.1667-1671.
- [98] Sherwin, C.W., Ruina, J.P., and Rawcliffe, D., 1962, Some early developments in Synthetic Aperture Radar systems, *IRE Trans. Military Electron.*, v.6, no.2, pp.111-115. (also in the reference [56])

- [99] Stolt, R.H., 1978, Migration by Fourier transform, *Geophysics*, v.43, pp.23-48.
- [100] Tomiyasu, K., 1978, Tutorial review of synthetic aperture radar (SAR) with applications to imaging of the ocean surface, *Proc. IEEE*, v.66, no.5, pp.563-583.
- [101] Trevett, J.W., 1986, *Imaging Radar for Resource Surveys*, Chapman and Hall.
- [102] Ulaby, F.T., Moore, R.K., and Fung, A.K., 1981, *Microwave Remote Sensing, Active and Passive: Vol.1*, Addison-Wesley.
- [103] Ulaby, F.T., Moore, R.K., and Fung, A.K., 1982, *Microwave Remote Sensing, Active and Passive: Vol.2*, Addison-Wesley.
- [104] Velten, E.H. and Dieterle, G.H., 1986, Development status of the ERS-1 payload instruments, *Proc. IGARSS'86, Zurich*, pp.161-166.
- [105] Wang, J., Howarth, P.J., 1989, Edge following as graph searching and Hough transform algorithm for lineament detection, *Proc. IGARSS'89, Vancouver*, v.I, pp.93-96.
- [106] Weglein, A.B., 1985, The inverse scattering concept and its seismic application: *Developments in Geophysical Exploration (Methods-6)*, Fitch T.J. (ed.), Elsevier Publishing Ltd., pp.111-138.
- [107] Wenzel, F., 1988, The relation between Born inversion and standard migration schemes, *J. Geophys.*, v.62, pp.148-157.
- [108] Won, J.S. and Moon, W.M., 1992, Inversion of synthetic aperture radar data for surface scattering: *Geophys. J. Int.*, v.108, pp.423-432.
- [109] Wu, C., 1976, A digital system to produce imagery from SAR data, *Proc. AIAA Syst. Design Driver by Sensors*, Paper 76-968.
- [110] Wu, C., 1980, A digital fast correlation approach to produce SEASAT SAR imagery, *Proc. IEEE Int. Radar Conf.*, pp.153-160.

- [111] Wu, C., Barkan, B., Karplus, W.J., and Carswell, D., 1982, SEASAT synthetic aperture radar data reduction using parallel programmable array processors, *IEEE Trans. Geosci. Remote Sensing*, v.20, no.3, pp.352-357.
- [112] Wu, C., Liu, K.Y., and Jin, M., 1982, Modeling and a correlation algorithm for spaceborne SAR signals, *IEEE Trans. Aerosp. Electron. Syst.*, v.18, pp.563-574.